Modification and incorporation of chitosan nanoparticles into different polymer matrices

by

Heino Pesch

Thesis presented in fulfilment of the requirements for the degree of Master of Science in the Faculty of Science (Polymer Science) at Stellenbosch University

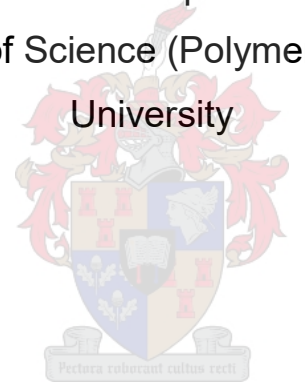

Department of Chemistry and Polymer Science,

Stellenbosch University

Supervisor: Dr. Marietjie Lutz

Co-supervisor: Prof. Albert van Reenen

March 2020

DECLARATION

By submitting this thesis electronically, I declare that the entirety of the work contained therein is my own, original work, that I am the sole author thereof (save to the extent explicitly otherwise stated), that reproduction and publication thereof by Stellenbosch University will not infringe any third party rights and that I have not previously in its entirety or in part submitted it for obtaining any qualification.

Heino Pesch March 2020

ABSTRACT

Chitosan is an abundantly found polysaccharide with known antimicrobial, biodegradable and nontoxic properties. Chitosan has been used in drug delivery systems and as partial components in food packaging materials. The main aim of this study was to incorporate functionalised chitosan nanoparticles into polymer matrices, which are used for packaging purposes, for investigation of their structure-property relationship. Therefore, poly(vinyl alcohol-co-ethylene) (EVOH) and low-density polyethylene (LDPE) were used as the matrices of interest. Chitosan was functionalised to *N,O*-carboxymethyl chitosan, for hydrophilic functionality, and a quaternary ammonium chitosan derivative, for hydrophobic functionality, before being crosslinked with sodium tripolyphosphate to produce three chitosan nanoparticle variants with different hydrophilic nature. The modified and unmodified chitosan nanoparticles were added to LDPE and three grades of EVOH copolymer, with varying ethylene content, to form composite films which were produced by solution casting and melt-pressing to create nanocomposite films. Furthermore, all three nanoparticles were added to the different EVOH copolymers by electrospinning to produce nanocomposite fibre mats. The nanoparticles were characterised by scanning electron microscopy and their thermal stability was evaluated by thermogravimetric analysis. The nanocomposite films and fibres were subjected to confocal fluorescence microscopy to investigate the nanoparticle distribution throughout the matrices. It was found that the electrospinning process improved the nanoparticle distributions when compared to solvent casting. Differential scanning calorimetry of the nanocomposites showed that a nanoparticle content of up to 8 wt% had an insignificant influence on the melting and crystallisation temperatures of the films and fibres but tended to decrease the melting and crystallisation enthalpies. Water uptake studies and static contact angle measurements showed, in general, that the addition of any of the three types of chitosan nanoparticles increased the wettability of the LDPE and EVOH films and fibres. It was also noted that the wettability of the EVOH fibres was more sensitive to the nanoparticle content. Antimicrobial studies were performed by using *Staphylococcus aureus* (*S. aureus*). The nanocomposite films all showed inhibition of *S. aureus*, irrespective of nanoparticle content. This inhibition was attributed to the hydrophobicity of the polymer films and the inability of *S. aureus* to attach onto the samples. The increased wettability of the nanocomposite fibres allowed the *S. aureus* to attach successfully and as a result no growth inhibition was observed. It was therefore concluded that a nanoparticle content of up to 8 wt% did not provide sufficient interaction with *S. aureus*.

OPSOMMING

Die gebruik van chitosan is reeds bekend weens sy antimikrobiese, bioafbreekbare en nie-giftige eienskappe. Chitosan is al gebruik as deel van verpakkingsmateriale en word gebruik as nanopartikels om te dien as ‘n vervoermiddel vir sekere medikasies. Die hoof doel van hierdie studie is om chitosan te funksionaliseer, nanopartikels daarvan te maak en dit in matrikse te voeg wat gebruik kan word in die verpakkingsindustrie. Die matrikse wat ondersoek was was poli(viniel alkohol-ko-etileen) (EVOH) en lae digtheid poliëtileen (LDPE). Chitosan was gefunksionaliseer na karboksiemetiel chitosan, vir addisionele hidrofiliese funksionaliteit, en na ‘n kwaternêre ammonium chitosan, vir addisionele hidrofibisiteit. Nanopartikels was vervaardig vanaf die oorspronkilike chitosan en gefunksionaliseerde weergawes. Die drie tipes chitosan nanopartikels was in LDPE en EVOH matrikse gevoeg deur gebruik te maak van drogings- en elektrospinprosesse. Drie tipes EVOH, met verskillende etileeninhoude, was gebruik. Hierdie prosesse het nanosaamgestelde materiale van twee verskillende formate geskep wat geanaliseer kon word. Die vervaardiging van chitosan nanopartikels was bevestig deur skanderingelektronmikroskopie en termiese-gravimetriese analise was gebruik om die termiese stabiliteit van die nanopartikels te vergelyk met die oorspronklike chitosan. Die nanosaamgestelde- films en vesels was geanaliseer deur konfokale fluoressensiemikroskopie en het gewys dat die elektrospinproses ‘n meer homogene verspreiding van chitosan nanopartikels veroorsaak het, in vergelyking met die drogingsproses. Differensieëlskanderingskalorometrie van die nanosaamgestelde materiale het gewys dat daar geen noemenswaardige verandering plaasgevind het in die vesels en films se smeltings- en kristallisasie temperatuur nie. Daar was wel ‘n algemene afname in die smeltings- en kristallisasie entalpie tot en met 8% gewigsinhoud van die verskillende nanopartikels. Die wateropname en statiese kontakhoek lesings het gewys dat die teenwoordigheid van enige van die drie soorte chitosan nanopartikels die hidrofibisiteit van die EVOH en LDPE films en vesels verlaag. Dit was ook duidelik dat die vesels se hidrofibisiteit die meeste beinvloed was deur die chitosan nanopartikels. *Staphylococcus aureus* (*S. aureus*) was gebruik vir die antimikrobiese studies en het gewys dat geen mikrobiese groei plaasgevind het op die nanosaamgestelde films nie. Hierdie bevinding was onafhanklik van die nanopartikel inhoud. Hierdie inhibisie is toegeskryf aan die hidrofibisiteit van die polimeer films en die onvermoë van *S. aureus* om te heg aan die film monsters. Die verlaagde hidrofibisiteit van die nanosaamgestelde vesels het toegelaat dat *S. aureus* suksesvol kon aanheg en as ‘n gevolg was geen inhibisie van groei waargeneem nie. Dit was dus bepaal dat die nanopartikels teen 8% van die nanosaamgestelde gewig nie voldoende interaksie met *S. aureus* verskaf het nie.

ACKNOWLEDGEMENTS

Dr. Marietjie Lutz, for acting as my supervisor and providing guidance and financial support.

Prof. Albert van Reenen, my co-supervisor, for advice, guidance and financial support.

Polyolefins research group, for all the assistance and for accommodating me in their group.

My parents, for supporting and motivating me throughout my research.

Prof. Marina Rautenbach, for assisting with the antimicrobial studies of the prepared nanocomposite materials.

Madelane Frazenburg and Elrika Harmzen at Stellenbosch University Central Analytical Facility (CAF) for SEM analysis.

Lize Engelbrecht at Stellenbosch University Central Analytical Facility (CAF) for confocal microscopy analysis.

Paul Reader at Kansai Plascon Stellenbosch for providing training to measure water contact angles.

I would like to acknowledge the **National Research Foundation (NRF)** for partially funding this research and therefore helping me to obtain my MSc.

TABLE OF CONTENTS

LIST OF FIGURES

LIST OF TABLES

LIST OF EQUATIONS

LIST OF ABBREVIATIONS

ATR-FTIR	attenuated total reflectance – fourier transform infrared
CFM	confocal fluorescence microscopy
CFU	colony forming units
CNP	chitosan nanoparticles
D_2O	deuterium oxide
DDA	degree of deacetylation
DMSO	dimethyl sulfoxide
DNA	deoxyribonucleic acid
DQ	degree of quaternisation
DSC	differential scanning calorimetry
EVOH	poly(vinyl alcohol-co-ethylene)
FITC	fluorescein isothiocyanate
GC	gas chromatography
HDPE	high-density polyethylene
LB	luria bertani
LDPE	low-density polyethylene
LLDPE	linear low-density polyethylene
mRNA	messenger ribonucleic acid
N	molality
N,O-CMC/np	*N,O*-carboxymethyl chitosan/nanoparticles
NBT	nitrotetrazolium blue chloride
NMR	nuclear magnetic resonance
PE	polyethylene
qC12/np	quaternary ammonium chitosan/nanoparticles
S. aureus	*Staphylococcus aureus*
SCA	static contact angle

SEM	scanning electron microscopy
SEM-EDS	scanning electron microscopy – energy dispersive spectroscopy
STDEV	standard deviation
TCD	tip to collector distance
TGA	thermogravimetric analysis
TPP	sodium tripolyphosphate
v/v	volume/volume
w/v	weight/volume
W_o	weight (initial)
W_t	weight (final)
wt%	weight percentage

CHAPTER 1

INTRODUCTION AND OBJECTIVES

1.1 Introduction

Chitin is the second most abundant linear polysaccharide, besides cellulose. The main use of chitin is the production of chitosan by a process of deacetylation[1]. Chitosan has been extensively researched in the past to illustrate its biodegradability, solubility, nontoxicity and antimicrobial properties[1–3]. The most significant interest in chitosan is for its nontoxicity and antimicrobial properties which makes it feasible for applications in drug delivery systems, biomedical applications and food packaging materials to extend the shelf-life of food and promote food safety[1,3–5]. In this regard, chitosan has been used as filler material for composite films and fibres with vinyl alcohol-co-ethylene (EVOH) and low-density polyethylene (LDPE), which are commonly used as packaging materials[6–8]. Furthermore, it has been shown that nanoparticles of desirable size can be produced from chitosan, specifically for drug delivery systems[4].

This study wants to use the existing knowledge of chitosan composites and nanoparticle production and combine it to investigate the effects of using chitosan nanoparticles as filler material in nanocomposite films and fibres of EVOH and LDPE. Furthermore, the field of knowledge is expanded by investigating the physical, thermal and surface properties of nanocomposite materials which are produced with hydrophilic and hydrophobic functionalised chitosan nanoparticles.

This study was approached by functionalising chitosan to obtain hydrophilic *N,O*-carboxymethyl chitosan (*N,O*-CMC) and hydrophobic quaternary ammonium chitosan (qC12)[9–11]. Thereafter, unmodified chitosan and the functionalised chitosan derivatives were crosslinked with sodium tripolyphosphate (TPP) to produce nanoparticles. The three nanoparticle variants were incorporated into EVOH and LDPE matrices during solvent casting and electrospinning processes to create nanocomposite films and fibres. The nanocomposite properties were evaluated by varying the polymer matrices, the matrix format (film and fibre), the nanoparticle content and the nanoparticle functional groups.

1.2 Aims and Objectives

The aim of this study was to incorporate chitosan nanoparticles into polymer matrices to act as filler material and to investigate the properties of the prepared nanocomposite materials. Specifically, a structure-property study was to be undertaken to investigate the influence of filler

and matrix hydrophobicity by varying the chitosan nanoparticle hydrophobicity through functionalisation and investigating polymer matrices of varying hydrophobicity.

The aim of this study was approached in terms of the following objectives:

1. Synthesis and characterisation of *N,O*-carboxymethyl chitosan (*N,O*-CMC) and quaternary ammonium chitosan, N,N-(2-dimethyl)propyl-3-N',N'-dimethyl-N'-dodecylammonium chitosan chloride (qC12).

2. Production of nanoparticles of unmodified chitosan, *N,O*-CMC and qC12 by using TPP as a crosslinking agent.

3. Production of nanocomposite films by using all three chitosan nanoparticle derivatives individually with EVOH and LDPE as polymer matrices and investigation of the thermal, physical, surface and antimicrobial properties.

4. Production of nanocomposite fibres by electrospinning EVOH together with all three chitosan nanoparticle derivatives and investigation of the thermal, physical, surface and antimicrobial properties.

5. Comparison of the properties of the produced nanocomposite films and fibres.

1.3 Thesis layout

An overview of the thesis structure is presented below.

Chapter 1: Introduction and objectives

This chapter provides an introduction to the research project. The research aims and objectives are discussed in detail.

Chapter 2: Relevant background

An overview of current literature knowledge which relates to this study is discussed in this chapter.

Chapter 3: Experimental

This chapter explains the experimental procedures and analytical techniques used during this study.

Chapter 4: Characterisation of functionalised chitosan nanoparticles

This chapter discusses the results of the chitosan functionalisation and the nanoparticle production which followed.

Chapter 5: Nanocomposite films

A discussion of the results for the incorporation of the functionalised chitosan nanoparticles into EVOH and LDPE matrices.

Chapter 6: Electrospinning of EVOH nanocomposites

Discusses the results for the electrospinning of nanocomposite materials which included EVOH and functionalised chitosan nanoparticles

Chapter 7: Conclusions and recommendations

Deals with the conclusions and future recommendations which arose from this study

1.4 References

1. Muxika, A., Etxabide, A., Uranga, J., Guerrero, P. & de la Caba, K. Chitosan as a bioactive polymer: Processing, properties and applications. *Int. J. Biol. Macromol.* **105**, 1358–1368 (2017).
2. Rinaudo, M. Chitin and chitosan: Properties and applications. *Prog. Polym. Sci.* **31**, 603–632 (2006).
3. Sahariah, P. & Másson, M. Antimicrobial Chitosan and Chitosan Derivatives: A Review of the Structure-Activity Relationship. *Biomacromolecules* **18**, 3846–3868 (2017).
4. Elgadir, M. A., Uddin, M. S., Ferdosh, S., Adam, A., Chowdhury, A. J. K. & Sarker, M. Z. I. Impact of chitosan composites and chitosan nanoparticle composites on various drug delivery systems: A review. *J. Food Drug Anal.* **23**, 619–629 (2015).
5. Bugnicourt, L. & Ladavière, C. Interests of chitosan nanoparticles ionically cross-linked with tripolyphosphate for biomedical applications. *Prog. Polym. Sci.* **60**, 1–17 (2016).
6. Hein, S., Wang, K., Stevens, W. F. & Kjems, J. Chitosan composites for biomedical applications: status, challenges and perspectives. *Mater. Sci. Technol.* **24**, 1053–1061 (2008).
7. Fernandez-Saiz, P., Ocio, M. J. & Lagaron, J. M. Antibacterial chitosan-based blends with ethylene-vinyl alcohol copolymer. *Carbohydr. Polym.* **80**, 874–884 (2010).
8. Vasile, C., Darie, R. N., Cheaburu-Yilmaz, C. N., Pricope, G. M., Bračič, M., Pamfil, D., Hitruc, G. E. & Duraccio, D. Low density polyethylene - Chitosan composites. *Compos. Part B Eng.* **55**, 314–323 (2013).
9. Hayes, E. R. N,O-Carboxymethyl chitosan and preparative method thereof. (1986).
10. Smit, M. Polymer-coated magnetic nanoparticles and modified polymer nanofibers for the efficient capture of Mycobacterium tuberculosis (Mtb) (MSc). (Stellenbosch University, 2018).

11. Guo, Z., Xing, R., Liu, S., Zhong, Z., Ji, X., Wang, L. & Li, P. Antifungal properties of Schiff bases of chitosan, N-substituted chitosan and quaternized chitosan. *Carbohydr. Res.* **342**, 1329–1332 (2007).

CHAPTER 2

RELEVANT BACKGROUND

2.1 Polymer matrices

Polymers such as poly(vinyl alcohol-co-ethylene) (EVOH) and low-density polyethylene (LDPE) are widely used in the packaging industry due to their attractive functionality and low cost, respectively[1]. As a result, these polymers have been subjected to previous studies which attempted to improve the polymer properties for the packaging industry[1–3]. In order to create composite materials from these polymers it is important to understand how they are synthesised and which variables are relevant in determining the properties of the polymers.

2.1.1 Poly(vinyl alcohol-co-ethylene) (EVOH)

EVOH copolymers are random semi-crystalline materials that consist of hydrophilic vinyl alcohol and hydrophobic ethylene monomeric units[1,4–6]. These copolymers are produced commercially by free radical polymerization followed by saponification[7]. Instead of vinyl alcohol, polymerization is performed using vinyl acetate and ethylene due to the instability of vinyl alcohol[7]. As a result, the saponification process converts the acetate functional group to a hydroxyl group to form EVOH. Figure 2.1.1-1 shows the structure of EVOH as it consists of its two monomeric constituents.

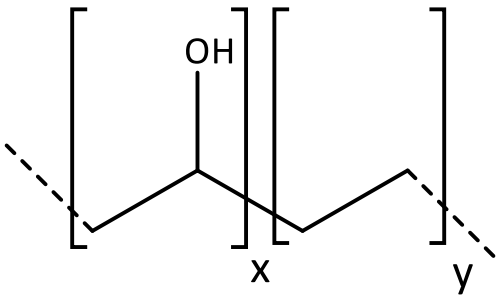

Figure 2.1.1-1: Chemical structure of EVOH consisting of its two constituent monomers.

EVOH copolymers are known to display excellent gas barrier properties to organic compounds and oxygen in dry conditions. The copolymer composition of EVOH determines its physical properties, where the polyvinyl alcohol monomer provides excellent gas barrier properties but is water soluble and the ethylene monomer provides water resistance but is lacking in gas barrier properties[7]. EVOH resins are commercially available mostly with vinyl contents of 52-76 mole % so that the copolymer displays a combination of the constituent monomer properties[7].

Despite the varying comonomer content, EVOH tends to show poor moisture resistance and plasticizes when exposed to moisture. Therefore, EVOH is usually placed between hydrophobic polymeric layers when used as packaging material. Some sources have reported a water uptake of up to 9 wt% which would significantly decrease the gas barrier properties of the

copolymer[8]. This water uptake can be attributed to the hydrogen bonds between the alcohol groups which are intercepted by the water molecules. This leads to a weakening of bonds and makes the EVOH polymer sensitive to moisture[1].

2.1.2 Low-Density Polyethylene (LDPE)

LDPE is a semicrystalline homopolymer which consists of a backbone made up by ethylene monomers. This polymer is generally described by the formula $(C_2H_4)_n$, where the value of n indicates the number of monomer chains connected to one another. LDPE has important applications in the packaging industry including the production of plastic bags and bottles.

The properties of polyethylene (PE) can be altered by varying the molecular weight, degree of crosslinking, molecular weight distribution and density[9]. Varying the properties of PE leads to the classification of specific PE variants. The most common variants include linear low-density polyethylene (LLDPE), low-density polyethylene (LDPE) and high-density polyethylene (HDPE). The main distinctions between these variants are branching and density differences. Figure 2.1.2-1 illustrates the differences in structure of the three PE variants.

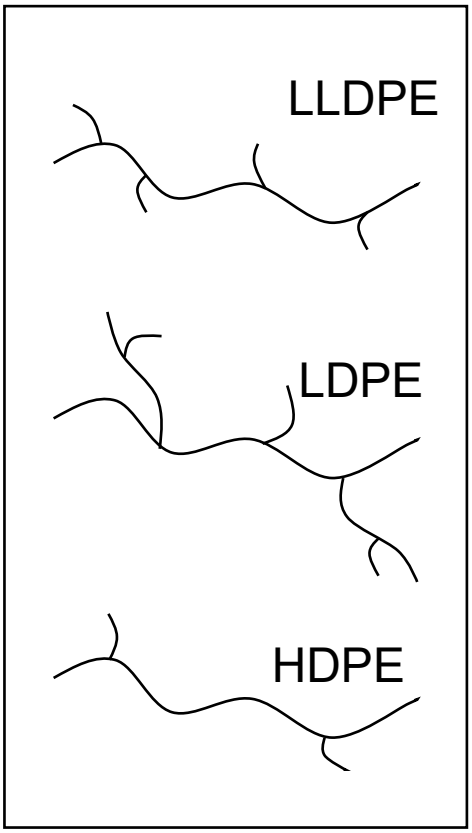

Figure 2.1.2-1: Illustration of the differences in branching between polyethylene variants.

2.2 Chitin

Chitin is a natural linear polysaccharide with a structure which can be described as poly(β-(1→4)-*N*-acetyl-D-glucosamine)[10]. Chitin is obtained from the exoskeletons of crustaceans, such as crabs and shrimp, and insects. This natural polymer is the most abundant biopolymer, after cellulose[10]. Chitin has also been found in the cell walls of fungi and yeast[10]. The structural difference between cellulose and chitin is that the hydroxyl group at the C2 position of cellulose is replaced by an amide group for chitin. Figure 2.2-1 below compares the chemical structures of cellulose and chitin.

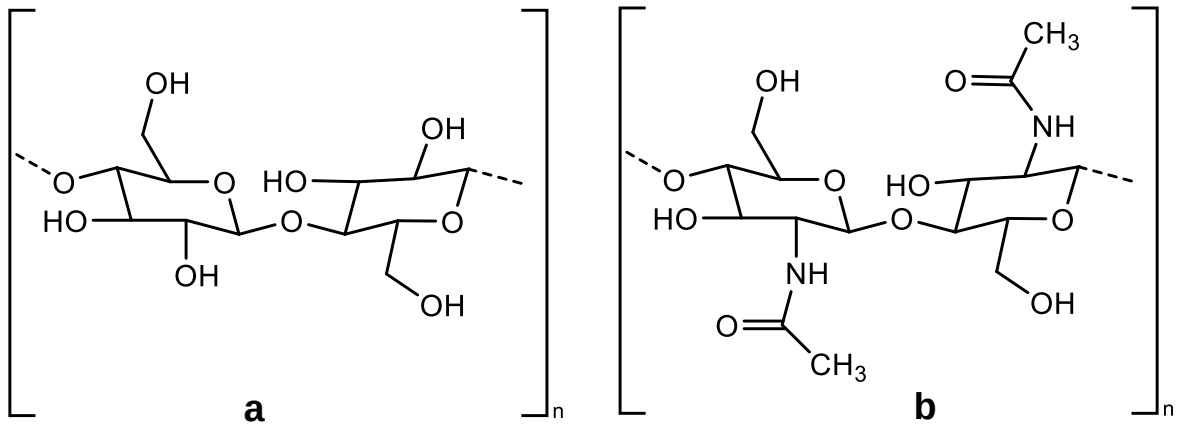

Figure 2.2-1: Structural comparison of (a) cellulose and (b) chitin.

Chitin is extracted from marine resources at an industrial scale by deproteinisation, through the addition of an alkaline solution to the raw material, and is followed by demineralization and discoloration using acidic and alkaline solutions, respectively[10,11]. Chitin is an attractive polymer to utilize for pharmaceutical and medical applications. This biopolymer is a biodegradable material, inert in the gastrointestinal tracts of mammals and exhibits biocidal properties[12]. These properties would favour the use of chitin for drug delivery and wound-dressing materials, if it were not for one significant drawback.

The disadvantage of chitin is that it is difficult to process due to its lack of solubility in solvents[13–15]. Its insolubility has been attributed to the acetamido functionality which causes strong inter- and intra-polymer hydrogen bonds. Instead of using harsh solvents to process chitin, it is generally preferred to convert chitin to chitosan through deacetylation of the acetamido group to yield an amino group[14].

2.3 Chitosan

Chitosan is a derivative of chitin which is obtained through a deacetylation process to produce a polymer with better solubility, while retaining the favourable properties of chitin[14]. Chitin and chitosan are distinguished from one another based on the degree of deacetylation of the

polymer. Chitin is said to have a degree of acetylation of 90% and once the degree of deacetylation reaches 50% it is known as chitosan[14]. This means that chitosan can be described as a random copolymer which consists of N-acetyl-D-glucosamine (acetylated) and D-glucosamine (deacetylated) repeating units with β-(1→4) linkages[11,14,16]. Figure 2.3.1-1 demonstrates the deacetylation process of chitin. The proton-sensitive amino group in chitosan contributes towards the solubility in acidic solutions and is the reason for the easier processing of chitosan[11,14]. The deacetylation process is performed by treating chitin with hydroxide solutions at elevated temperatures[11,15]. The degree of deacetylation and molecular weight of chitosan are two important variables of the biopolymer and can influence properties such as viscosity, solubility and heavy metal ion chelation[17]. As a result, the deacetylation process must be controlled to provide the desired functionality of the polymer[11,14].

2.3.1 Chitosan functionalisation

The deacetylation of chitin to chitosan is an example of chemical modification to obtain desired functionality from polymeric material. Figure 2.3.1-1 shows the functional groups present in chitosan after partial deacetylation. Research has been done to investigate further functionalisation of these functional groups to create chitosan derivatives with modified structural properties, whether it be increased solubility, hydrophobicity or antimicrobial activity[10,13,15,18–23]. The deacetylation process increases the amount of amino groups present in the repeating units of chitosan, which can be used for further functionalisation such as Schiff base chitosan and quaternised chitosan synthesis (qC12)[19]. The hydrophobicity of chitosan can be increased by the addition of long alkyl chains to the repeat units[13,18]. Chitosan solubility can be improved by selective functionalisation. An example of this is the synthesis of a water-soluble chitosan derivative, *N,O*-carboxymethyl chitosan (*N,O*-CMC), by the addition of a carboxylmethyl group to the free amino groups and primary alcohols of chitosan[24,25]. Therefore, the functionality of chitosan provides an opportunity to synthesise polymer derivatives with increased hydrophilicity (*N,O*-CMC) and increased hydrophobicity (qC12), relative to unmodified chitosan. This enables the evaluation of chitosan hydrophobicity in a structure-property study.

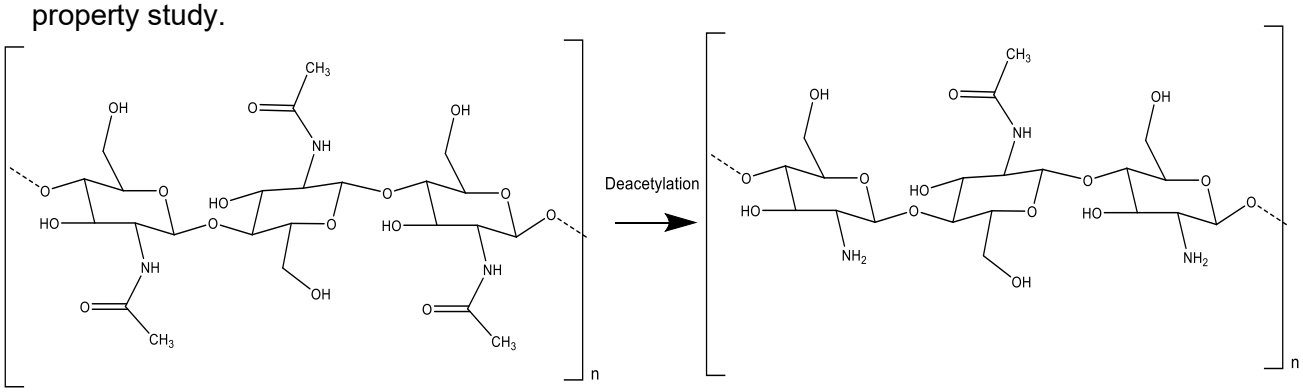

Figure 2.3.1-1: Partial deacetylation of chitin to produce chitosan.

2.3.2 Chitosan nanoparticles

Chitosan nanoparticle production has been studied extensively in previous works[11,13,15,26–28]. Nanoparticle production has been achieved using microemulsion, emulsification solvent diffusion, polyelectrolyte complex and ionotropic gelation, with the last mentioned being the most widely used method[28,29]. From here on only ionotropic gelation will be discussed in more detail. A common crosslinking agent, for the ionotropic gelation method, is sodium tripolyphosphate (TPP) because it is nontoxic and possesses a quick gelling ability[28]. Figure 2.3.2-1 shows a typical crosslinking reaction between chitosan, with its amino group protonated in an acidic solution, and a solution of TPP.

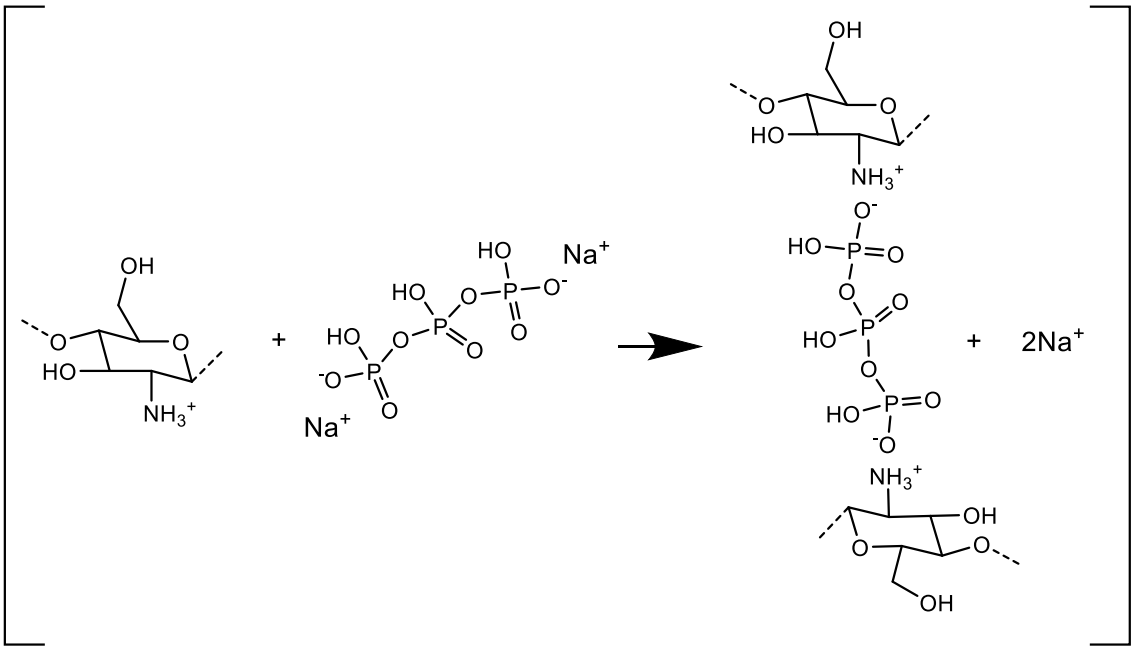

Figure 2.3.2-1: Ionotropic gelation between sodium tripolyphosphate (TPP) in solution and protonated chitosan.

The positively charged amino group on the chitosan experiences ionic interaction with the negatively charged TPP and leads to a physical crosslinking which reduces the risk of damaging biological agents or drug-loading attempts in further experiments[27]. This method of nanoparticle production can be used on chitosan which has been functionalised further, prior to crosslinking[18,30]. It was shown that various aspects, such as chitosan solution concentration, TPP solution concentration, chitosan solution pH, chitosan solution temperature, mass ratio of chitosan to TPP, acetic acid solution concentration and ambient temperature, influenced the nanoparticle size[27,31]. These parameters all have critical values at which nanoparticle size will start to increase. Therefore, optimisation of the experimental setup is required during nanoparticle production.

2.4 Composite materials

Composites are materials that consist of more than one base constituent. A composite is defined in terms of its matrix and filler, or reinforcing phase. The filler material is added to the matrix to supplement the matrix material properties or modify them. The concentration of filler content has a significant influence on the mechanical and chemical properties of the composite. Filler loadings up to 30% have been reported but in most cases such high loadings are not feasible and significant changes in composite properties can already be seen with 5% loadings[32,33]. The use of composites, to obtain desirable properties from different materials, is well established. Natural fibre based polymer composites already appeared in 1908, with reinforced plastics surfacing around 1940[34]. Composite materials can also be classified specifically as nanocomposites. Figure 2.4-1 illustrates a composite material that consists of a matrix and reinforcing material.

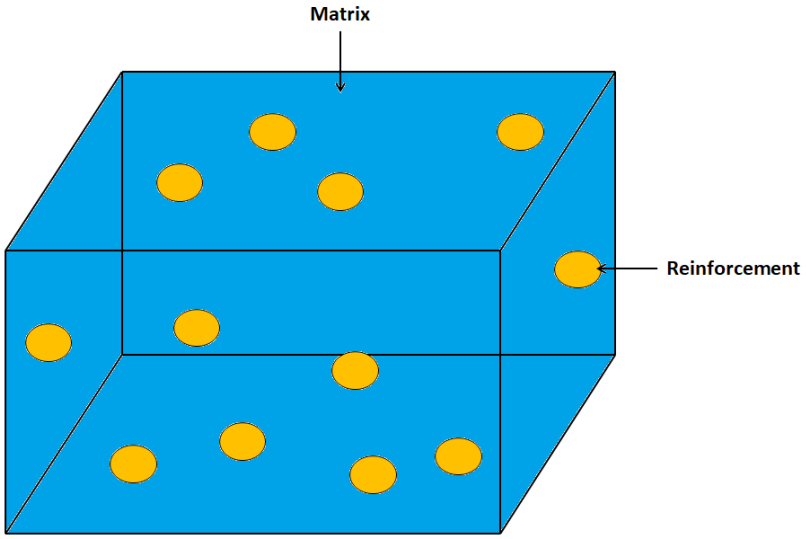

Figure 2.4-1: Illustration of a composite material consisting of a matrix and reinforcing material.

For a material to be classified as a nanocomposite at least one constituent of the composite, usually the filler material, must have a dimension in the nanometre range. The nanometre range is technically defined between 1-1000 nm but it is often considered to be limited to 100 nm. As mentioned earlier, chitosan is an attractive biodegradable polymer, with antimicrobial properties, and has enjoyed applications in the biomedical field[35,36]. Previous research reports on the investigation of the incorporation of chitosan into LDPE and EVOH matrices to prepare antimicrobial composites, with increased antimicrobial activity noticed at 2 wt% chitosan[2,3,37]. This study will look at using chitosan nanoparticles as filler material in LDPE and EVOH matrices to modify nanocomposite properties by varying chitosan hydrophobicity through functionalisation. This is aimed at gaining insight into the interactions between amphiphilic

polymer fillers and matrices and modifying the interactions by varying the hydrophobicity of the amphiphilic polymers.

2.5 Electrospinning

Electrospinning is a fibre-creating process of drawing polymeric solutions or melts into fibres by applying an electric field to the polymer[38–40]. Electrospinning has enjoyed attention in multiple avenues of research due to the favourable properties of drawn fibres, which include potential nanoscale dimensions and therefore high surface-to-volume ratios. Research has focused on optimising electrospinning techniques, expanding electrospinning feasibility to additional polymers and reinforcing electrospun fibres with filler material[38–44].

As mentioned above, electrospinning can be performed either by melt spinning, or solution spinning. Melt electrospinning is an attractive option to create fibres from polymeric materials which have low solubility or require high boiling point and toxic solvents to dissolve. The problem arises that the experimental procedure for melt electrospinning is more complex than solution spinning. Effective temperature control must be applied across the experimental equipment to ensure that the polymer remains in the melted state during electrospinning. As a result, solution electrospinning is the more common method being used. A typical solution electrospinning setup is shown in Figure 2.5-1 and consists of a syringe, needle, syringe pump, voltage supply and collector plate for the fibre mat.

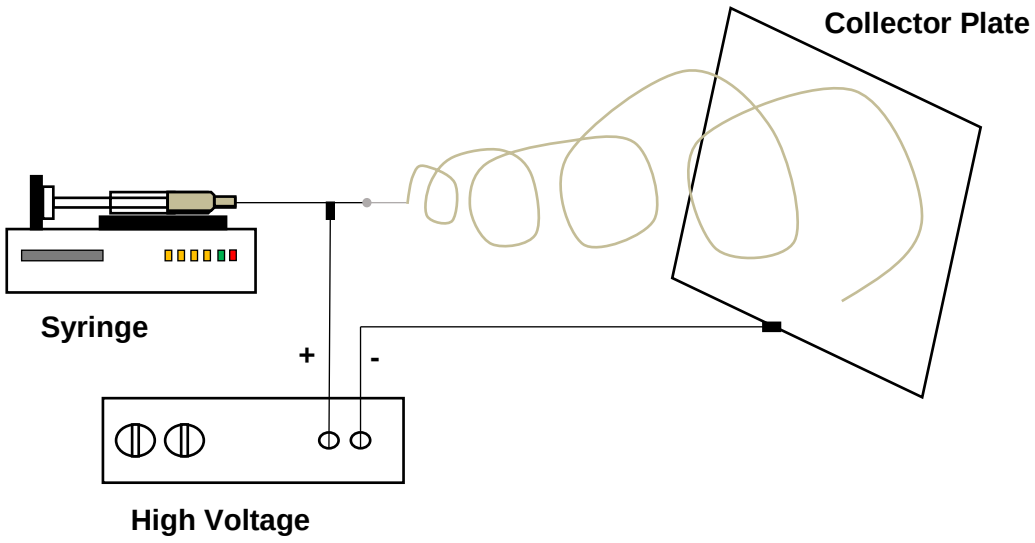

Figure 2.5-1: Typical experimental setup for solution electrospinning of polymeric material.

During the electrospinning process there are multiple parameters which have an influence on the fibre morphology. These parameters can be classified as process (solution flow rate, applied electric field, distance between needle and collector), solution (polymer concentration,

solvent, solution conductivity and viscosity) and environmental (temperature and humidity) parameters[38,40]. Depending on the polymer being used, each of the mentioned parameters will have a critical value at which optimally uniform fibres will be formed. This means that all these parameters have to be controlled in order to obtain reproducibility during the electrospinning process.

During the electrospinning process a Taylor cone will form at the needle tip. Its geometry is determined by the ratio of electrostatic repulsion, which is caused by the applied electric field, and the surface tension of the polymer solution[40]. As a result, the success of an electrospinning process can be gauged during operation by visual inspection of the Taylor cone geometry and the presence of a liquid-solid transition zone. The Taylor cone position and phase transition zone is shown in Figure 2.5-2.

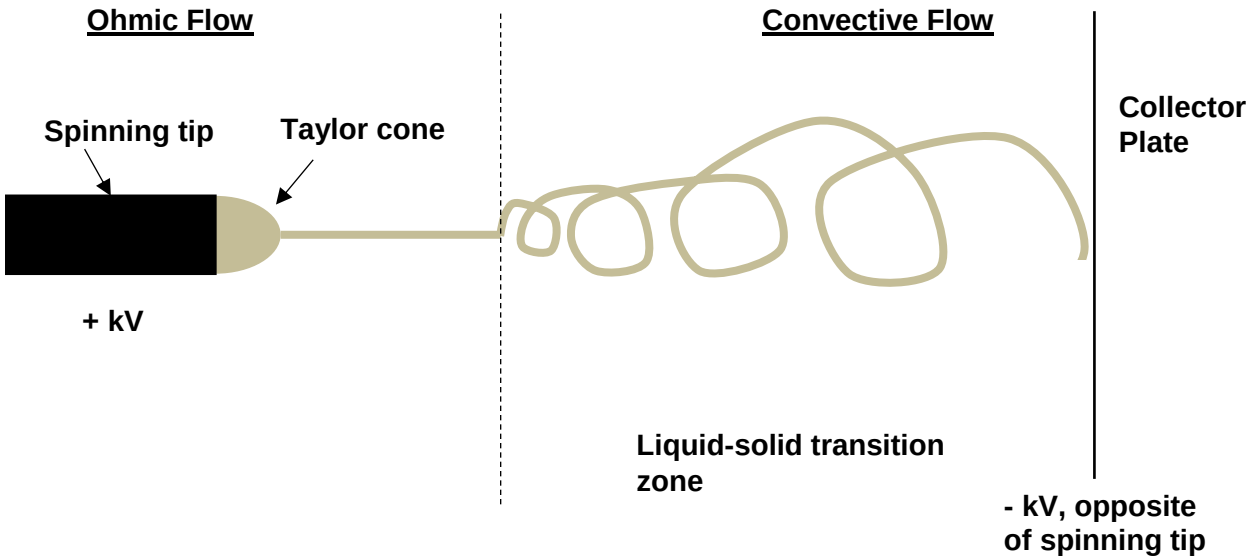

Figure 2.5-2: Illustration of Taylor cone formation and phase transition during electrospinning.

Previous research reports on the incorporation of biopolymers into electrospinning processes to modify composite properties[39,41,43]. This study will look at the use of electrospinning for the distribution of chitosan nanoparticles throughout polymer matrices and compare it to film forming techniques.

2.6 Fluorescence

Some of the major challenges associated with chitosan nanoparticle production include particle agglomeration and distribution when incorporated into a matrix. Methods such as scanning electron microscopy (SEM) are not always able to properly investigate the nanoparticle distribution as the particles are often imbedded within the matrix[1]. An alternative method for

such investigation is fluorescence spectroscopy, which is able to determine the degree of homogeneity of nanoparticle sizes and distribution.

Fluorescent dyes have have been used across multiple scientific disciplines, ranging from biochemistry to polymer science, to act as sensors and trackers[45]. The principle of fluorescence is based on the fact that molecules are able to absorb and emit light at specific wavelengths. The absorbance of photons leads to an increase in energy of the molecule[46]. This increased energy is emitted as light to return the molecule to a more favourable energy level. The emitted light is present at a higher wavelength, compared to the absorbed light, as not all the absorbed energy is lost through light emission. Figure 2.6-1 illustrates this phenomenon.

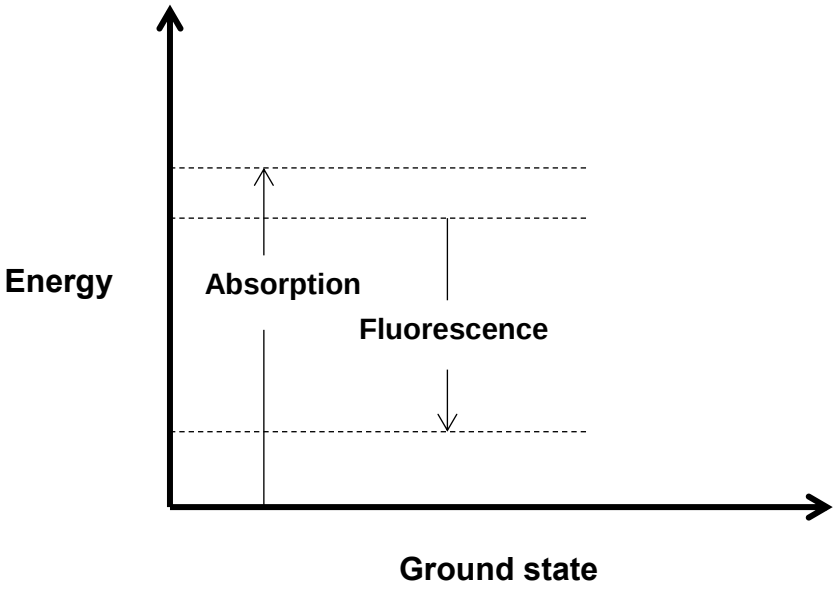

Figure 2.6-1: Illustration of the difference in energy of absorbed and emitted light due to fluorescence.

Fluorescent molecules are designed so that they absorb and emit light at specific wavelengths. An example such a fluorescent molecule is fluorescein. A common derivative of fluorescein is fluorescein isothiocyanate (FITC) which is excited by light at λ_{ex} = 490 nm and emits light at λ_{em} = 520 nm[47,48].

Chitosan possesses an amino and two hydroxyl groups which can be used for further functionalisation. This means that chitosan and its derivatives can be functionalised with a fluorescent marker such as FITC. Research has been done in this regard by considering the reaction between the primary amine of chitosan and the isothiocyanate group of FITC[46,48,49]. Figure 2.6-2 illustrates the reaction between chitosan and FITC.

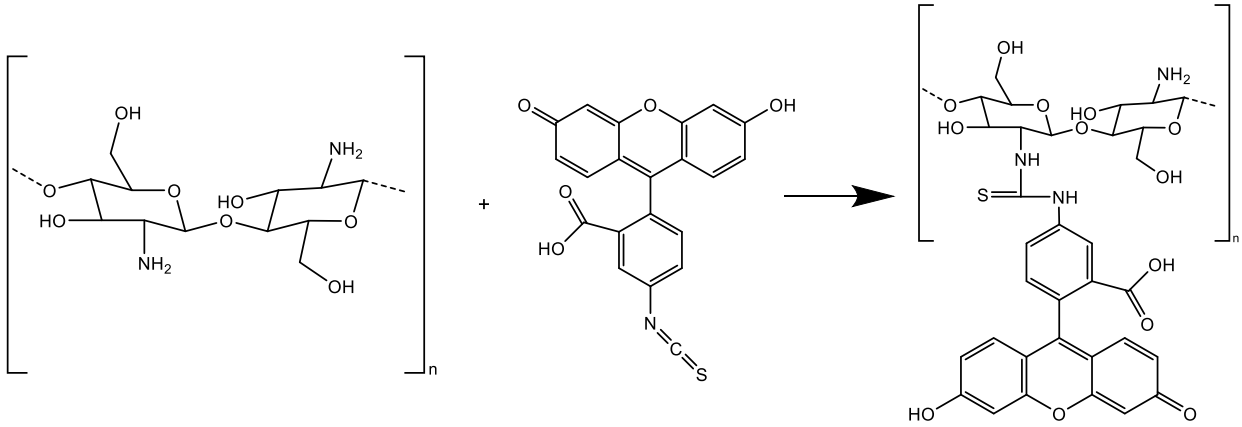

Figure 2.6-2: Reaction between fluorescein isothiocyanate (FITC) and fully deacetylated chitosan to produce a fluorescently labelled polymer.

2.7 Nanoparticle and nanocomposite characterisation methods

2.7.1 Fourier transform infrared (FTIR) spectroscopy

Fourier transform infrared (FTIR) spectroscopy is a simplistic, yet powerful, analysis method which is used extensively in the field of chemistry for sample characterisation[1,50–52]. A FTIR spectra is obtained by measuring the absorbance of infrared radiation, by a molecule, across a range of wavelengths. This provides a unique result for any molecule as similar functional groups will always display the same FTIR spectra. Through this principle, individual molecular constituents can be identified through comparison of experimental absorbance bands to known spectra.

The FTIR equipment can also be operated in various modes, specifically in transmission or attenuated total reflectance (ATR) modes[50]. Transmittance mode allows light to pass through the entire sample, which means that the sample must be transparent and of low thickness to allow the light to be captured as it exits the sample. The ATR method introduces light at an angle to the sample surface and as a result the light is reflected from the surface. This method requires less sample preparation and is a rapid identification method but the light only penetrates the sample surface and is therefore purely a surface analysis method[52].Therefore, ATR-FTIR can be useful for the characterisation of chitosan and the confirmation of any further functionalisation[18,53].

2.7.2 Nuclear magnetic resonance (NMR) spectroscopy

Chitin and chitosan have both been characterised extensively through the use of NMR spectroscopy[10,54–57]. Subjecting chitosan to NMR spectroscopy can provide important structural information, such as the degree of *N*-acetylation, which contributes to the physical property differences between chitin and chitosan[10,57]. Multiple NMR techniques can be used to

characterise chitin and chitosan. These include ^{1}H NMR, ^{13}C NMR and ^{15}N NMR[55]. It was found that ^{1}H NMR had desirable sensitivity towards determining the degree of *N*-acetylation, while ^{13}C NMR and ^{15}N NMR had better chemical shift dispersions[55,56]. This means that ^{13}C NMR and ^{15}N NMR can be used to investigate structural differences in chitosan after functionalisation. Therefore, ^{1}H NMR and ^{13}C NMR can be used to characterise chitosan and its functionalised derivatives[18,20,24,53,54,58].

2.7.3 Scanning electron microscopy (SEM)

A scanning electron microscope (SEM) investigates sample surfaces with an electron beam. The interaction between the incident electrons and the sample surface provides information on surface topology by measuring height differences on the surface[1,59]. The strength of the incident electrons can also be varied, usually between 2-40 keV, to vary the extent of surface penetration[59]. SEM has been used previously to image chitosan nanoparticles to confirm its presence and compare particle sizes and agglomeration during various preparation methods[15,29,60,61].

2.7.4 Thermogravimetric analysis (TGA)

Thermogravimetric analysis (TGA) is a thermal process whereby a sample of interest is subjected to a heating cycle, usually in the range of 25-600°C, in order to gain insight to the thermal stability of the sample. The weight loss of the sample is recorded during the heating cycle and the major weight loss event is an indication of the primary degradation phase. Previous studies have used TGA to determine the composition of composite materials, as long as the constituent components had thermal degradation events which did not overlap[62]. This type of analysis is useful prior to sample processing to ensure that materials are not degraded.

2.7.5 Differential scanning calorimetry (DSC)

DSC is a thermal analysis technique which provides sample information such as glass transition temperature, percentage crystallinity, crystalline melting point, thermal stability and more[1]. This is achieved by subjecting samples to thermal transitions by applying heating and cooling cycles to the samples. Heat flow is therefore measured across a temperature range to produce a DSC thermogram of the sample of interest. DSC analysis has been previously used on chitosan to indicate residual water content within the polymer and to determine thermal degradation temperatures[63,64]. Therefore, DSC could be used to investigate thermal properties of polymer composites with varying degrees of filler content. Furthermore, the influence of polymer morphology on thermal stability can be investigated by analysing similar polymers, or composites, in varying physical forms. This could include powdered polymers, melt-pressed films or electrospun fibres.

TGA is sometimes performed prior to DSC to ensure that samples do not degrade during the heating and cooling cycles of the DSC analysis.

2.7.6 Confocal fluorescence microscopy (CFM)

As mentioned earlier (Chapter 2.6) fluorescence can be used to investigate nanoparticle agglomeration and distribution when incorporated into a matrix. This can be achieved by comparing the fluorescence intensity throughout the sample. Unfortunately there are no standards for fluorescence intensity, which means that the results which are obtained from fluorescence microscopy are qualitative, rather than quantitative.

According to literature, the term confocal originates from the use of a pinhole in front of the detector to eliminate signals which are out of focus. By scanning different depths of a sample, and removing signals which are out of focus each time, it is possible to obtain multiple images which combine to produce a three-dimensional image[45]. A schematic representation of sample excitation during CFM is shown in Figure 2.7.6-1.

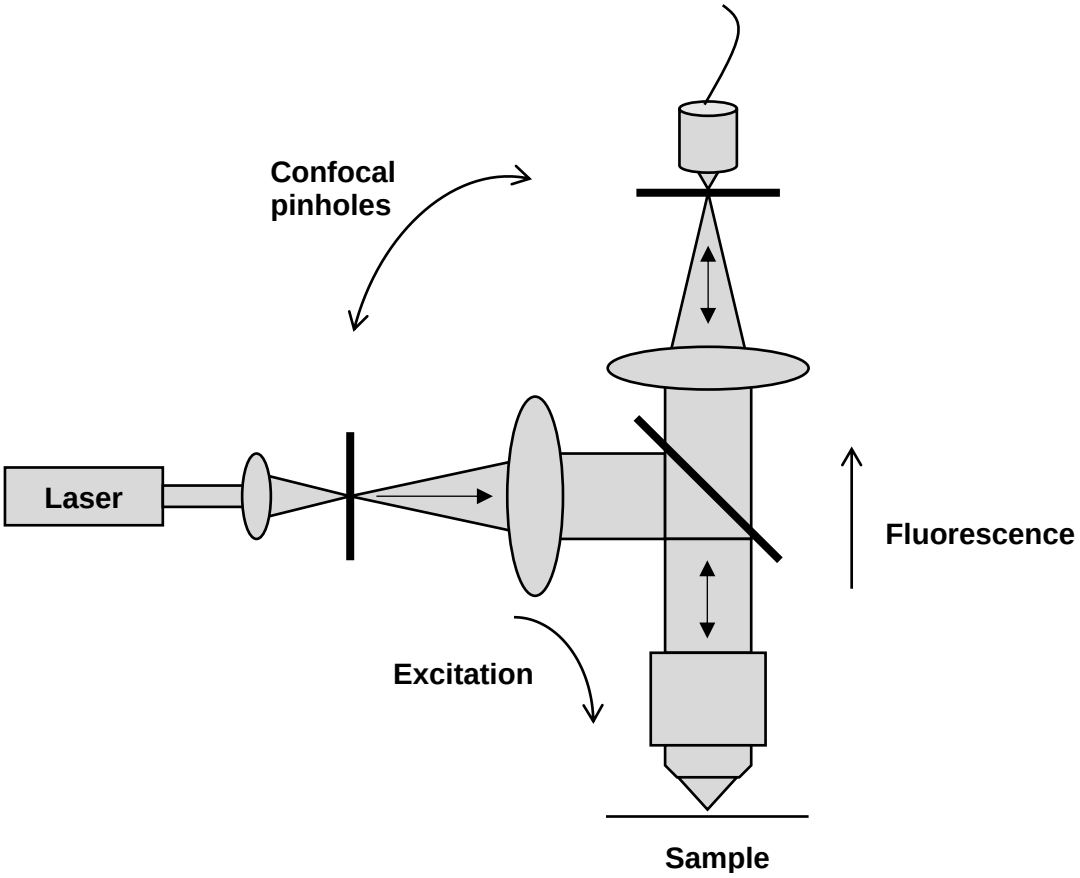

Figure 2.7.6-1: Diagram illustrating sample excitation and fluorescence during confocal fluorescence microscopy (CFM)[45].

2.7.7 Static contact angle (SCA) measurements and water uptake

The purpose of adding nanofillers to a polymer matrix is to change its physical and or chemical properties. One such property is the wettability of a polymer, which indicates the ability of the polymer to absorb water. In the case of packaging material it would be advantageous for the polymer to have low water absorption capabilities. One way of determining the hydrophobicity of a material is by measuring the water uptake of the material[65]. Another way is by calculating the static contact angle (SCA) between the material surface and water interface[66]. Figure 2.7.7-1 illustrates the measurable contact angle at the three-phase interface which is used to determine the hydrophobicity of a sample. A measurable angle with $\theta < 90°$ is predominantly associated with hydrophilic materials, whereas $90° < \theta < 150°$ is regarded as hydrophobic and $\theta > 150°$ super hydrophobic.

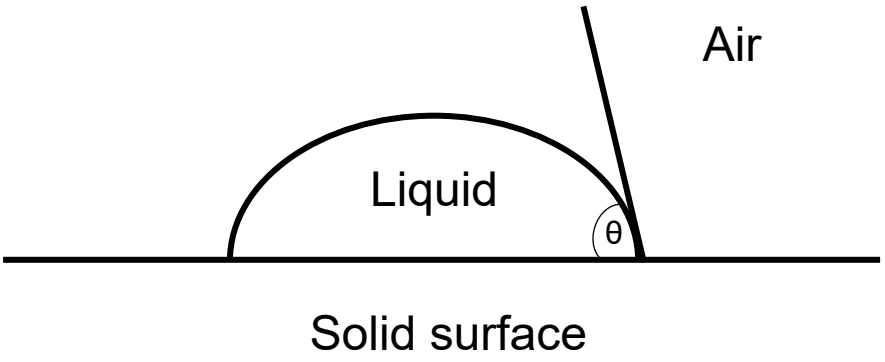

Figure 2.7.7-1: Three-phase interface used to calculate the static contact angle of a specific material for a specified liquid.

The surface roughness also plays a significant role in determining the wettability of a sample. Modes of wetting have been proposed to explain what happens during wetting. In the case of a smooth surface the applied liquid covers the entire surface area. For a roughened surface two modes of wetting can occur: a Wenzel mode can occur where the applied liquid penetrates the roughened surface and adheres to the surface, but the more common wetting mode is the Cassie mode. In this last mentioned mode air is trapped between the applied liquid and the roughened sample surface, resulting in air pockets and reducing the contact area between the sample and liquid interface[67]. The various wetting modes are shown in Figure 2.7.7-2.

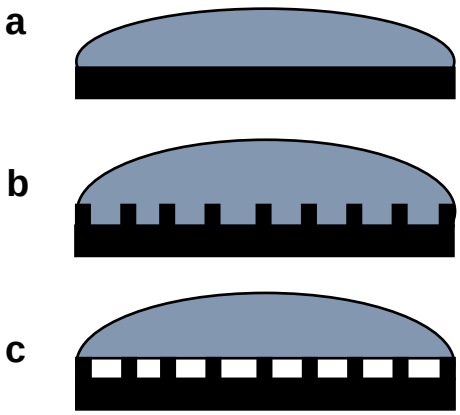

Figure 2.7.7-2: Illustration of surface wetting of (a) a smooth surface, (b) a Wenzel mode and (c) a Cassie mode[67].

2.7.8 Antimicrobial testing

The current interest in chitosan, and its derivatives, comes from them being natural, biodegradable, nontoxic polymers and possessing antimicrobial properties. This has led to research focussing on using chitosan in drug delivery systems or as composite material for the packaging industry. The specific chitosan derivative and bacteria being tested both influence the observed antimicrobial properties of the natural polymer. Therefore, comparison with literature must be done with care as most experimental results will be incomparable.

Although many studies have recorded the antimicrobial properties of chitosan derivatives, their exact mechanisms of action are still not fully understood. With that being said, there are some proposed mechanisms of action which have been widely accepted[13,68–70]. A review of the mechanism of antibacterial action of chitosan has led to four possible mechanisms which could be applicable for both Gram positive and negative bacteria[13].

Gram positive and negative bacteria possess cell walls with different compositions. Gram positive bacteria have an outer cell wall which consists of a thick peptidoglycan layer. This peptidoglycan layer is made up of negatively charged teichoic acids which are covalently linked with *N*-acetylmuramic acid. Gram negative bacteria possesses a thin peptidoglycan layer but is covered by an outer membrane. This outer membrane consists mainly of lipoprotein and lipopolysaccharide[13]. In both cases chitosan has to interact with the bacterial surface.

A widely accepted model is the ionic interaction between the cationic chitosan and anionic components on the bacterial surface. This model requires the presence of a positive charge in the chitosan backbone. For Gram positive bacteria, this means the peptidoglycans of the cell wall are hydrolysed and leads to intracellular leakage.

The second mechanism focuses on Gram negative bacteria and it proposes that chitosan bonds ionically to the surface of the cell and prevents the flow of nutrients into the cell. Figure 2.7.8-1 illustrates the first two proposed mechanisms.

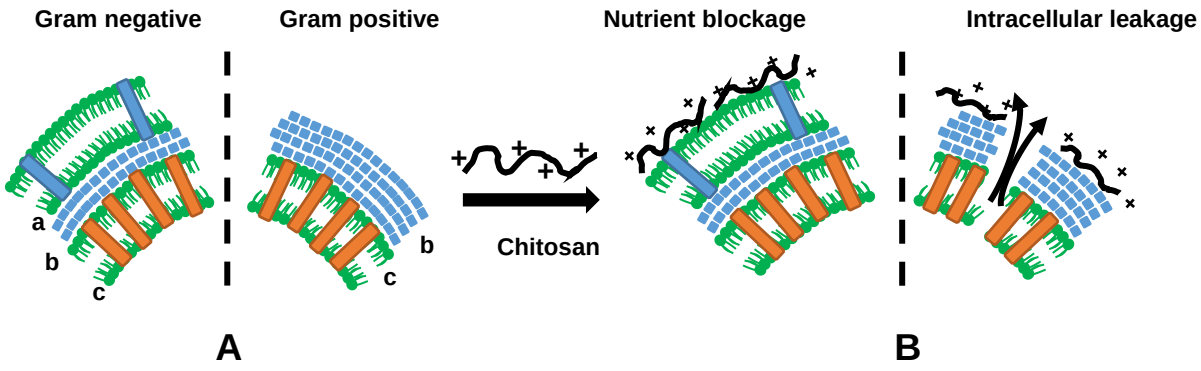

Figure 2.7.8-1: Proposed modes of action of chitosan on Gram positive and negative bacteria (A) before and (B) after the introduction of chitosan. Multiple layers where a = outer layer, b = peptidoglycan layer and c = cytoplasmic layer[13].

The third mechanism proposes that chitosan can penetrate the microbial cell and inhibit mRNA synthesis by binding to the DNA of the cell[70]. This method is unlikely to occur in high molecular weight chitosan or chitosan derivatives but its limitations might be overcome by making use of nanoparticles to ensure the chitosan penetrates the cell. The final mechanism proposes that chitosan, with unprotonated amino groups, has metal ion chelating properties and can affect the metal ions present in the bacterial surface. The bonding between chitosan and the metal ions will then inhibit the growth of the microorganism[13].

Based on these models, it is widely accepted that chitosan has an electrostatic interaction with the outer surface of the fungi or bacteria and leads to surface rupture and, ultimately, cellular leakage.

2.7.9 Tensile testing

Tensile testing is a simple technique used to obtain mechanical property information of materials. The material in question is subjected to a constant applied force in one direction until the elongation of the material results in its complete failure. The toughness, strength and tensile modulus of a material can be investigated from these experiments[1].

This type of analysis is useful in determining the influence of filler content on the mechanical properties of composite materials. Previous studies have looked at the addition of cellulose nanowhiskers into polymer matrices and tensile testing has been used to investigate the mechanical properties of chitosan/polypropylene composite films[1,32].

2.8 References

1. Du Toit, M. L. Incorporation of polysaccharide nanowhiskers into a poly (ethylene-co-vinyl alcohol) matrix (MSc). (University Stellenbosch, 2013).

2. Park, S. Il, Marsh, K. S. & Dawson, P. Application of chitosan-incorporated LDPE film to sliced fresh red meats for shelf life extension. *Meat Sci.* **85**, 493–499 (2010).

3. Vasile, C., Darie, R. N., Cheaburu-Yilmaz, C. N., Pricope, G. M., Bračič, M., Pamfil, D., Hitruc, G. E. & Duraccio, D. Low density polyethylene - Chitosan composites. *Compos. Part B Eng.* **55**, 314–323 (2013).

4. Deng, P., Liu, M., Zhang, W. & Sun, J. Preparation and physical properties of enhanced radiation induced crosslinking of ethylene-vinyl alcohol copolymer (EVOH). *Nucl. Instruments Methods Phys. Res. Sect. B Beam Interact. with Mater. Atoms* **258**, 357–361 (2007).

5. Cabedo, L., Lagarón, J. M., Cava, D., Saura, J. J. & Giménez, E. The effect of ethylene content on the interaction between ethylene-vinyl alcohol copolymers and water-II: Influence of water sorption on the mechanical properties of EVOH copolymers. *Polym. Test.* **25**, 860–867 (2006).

6. López-Rubio, A., Lagaron, J. M., Giménez, E., Cava, D., Hernandez-Muñoz, P., Yamamoto, T. & Gavara, R. Morphological alterations induced by temperature and humidity in ethylene-vinyl alcohol copolymers. *Macromolecules* **36**, 9467–9476 (2003).

7. Mokwena, K. K. & Tang, J. Ethylene Vinyl Alcohol: A Review of Barrier Properties for Packaging Shelf Stable Foods. *Crit. Rev. Food Sci. Nutr.* **52**, 640–650 (2012).

8. Martínez-Abad, A., Lagaron, J. M. & Ocio, M. J. Development and characterization of silver-based antimicrobial ethylene-vinyl alcohol copolymer (EVOH) films for food-packaging applications. *J. Agric. Food Chem.* **60**, 5350–5359 (2012).

9. Malpass, D. B. *Introduction to Industrial Polyethylene*. *Introduction to Industrial Polyethylene: Properties, Catalysts, and Processes* (John Wiley & Sons, Inc., 2010). doi:10.1002/9780470900468.

10. Rinaudo, M. Chitin and chitosan: Properties and applications. *Prog. Polym. Sci.* **31**, 603–632 (2006).

11. Muxika, A., Etxabide, A., Uranga, J., Guerrero, P. & de la Caba, K. Chitosan as a bioactive polymer: Processing, properties and applications. *Int. J. Biol. Macromol.* **105**, 1358–1368 (2017).

12. Nasrin, R., Biswas, S., Rashid, T. U., Afrin, S., Jahan, R. A., Haque, P. & Rahman, M. M.

Preparation of Chitin-PLA laminated composite for implantable application. *Bioact. Mater.* **2**, 199–207 (2017).

13. Sahariah, P. & Másson, M. Antimicrobial Chitosan and Chitosan Derivatives: A Review of the Structure-Activity Relationship. *Biomacromolecules* **18**, 3846–3868 (2017).

14. Ryan, C., Alcock, E., Buttimer, F., Schmidt, M., Clarke, D., Pemble, M. & Bardosova, M. Synthesis and characterisation of cross-linked chitosan composites functionalised with silver and gold nanoparticles for antimicrobial applications. *Sci. Technol. Adv. Mater.* **18**, 528–540 (2017).

15. Jothimani, B., Sureshkumar, S. & Venkatachalapathy, B. Hydrophobic structural modification of chitosan and its impact on nanoparticle synthesis – A physicochemical study. *Carbohydr. Polym.* **173**, 714–720 (2017).

16. Fan, W., Yan, W., Xu, Z. & Ni, H. Formation mechanism of monodisperse, low molecular weight chitosan nanoparticles by ionic gelation technique. *Colloids Surfaces B Biointerfaces* **90**, 21–27 (2012).

17. Elgadir, M. A., Uddin, M. S., Ferdosh, S., Adam, A., Chowdhury, A. J. K. & Sarker, M. Z. I. Impact of chitosan composites and chitosan nanoparticle composites on various drug delivery systems: A review. *J. Food Drug Anal.* **23**, 619–629 (2015).

18. Smit, M. Polymer-coated magnetic nanoparticles and modified polymer nanofibers for the efficient capture of Mycobacterium tuberculosis (Mtb) (MSc). (Stellenbosch University, 2018).

19. Guo, Z., Xing, R., Liu, S., Zhong, Z., Ji, X., Wang, L. & Li, P. Antifungal properties of Schiff bases of chitosan, N-substituted chitosan and quaternized chitosan. *Carbohydr. Res.* **342**, 1329–1332 (2007).

20. Mourya, V. K., Inamdar, N. N. & Tiwari, A. Carboxymethyl chitosan and its applications. *Adv. Mater. Lett.* **1**, 11–33 (2010).

21. Anitha, A., Divya Rani, V. V., Krishna, R., Sreeja, V., Selvamurugan, N., Nair, S. V., Tamura, H. & Jayakumar, R. Synthesis, characterization, cytotoxicity and antibacterial studies of chitosan, O-carboxymethyl and N,O-carboxymethyl chitosan nanoparticles. *Carbohydr. Polym.* **78**, 672–677 (2009).

22. Sugimoto, M., Morimoto, M., Sashiwa, H., Saimoto, H. & Shigemasa, Y. Preparation and characterization of water-soluble chitin and chitosan derivatives. *Carbohydr. Polym.* **36**, 49–59 (1998).

23. Bakshi, P. S., Selvakumar, D., Kadirvelu, K. & Kumar, N. S. Comparative study on

antimicrobial activity and biocompatibility of N-selective chitosan derivatives. *React. Funct. Polym.* **124**, 149–155 (2018).

24. Lin, C. C. & Lin, C. W. Preparation of N,O-carboxymethyl chitosan nanoparticles as an insulin carrier. *Drug Deliv.* **16**, 458–464 (2009).

25. Kusuma, H. S., Al-sa'bani, A. F. & Darmokoesoemo, H. N,O-Carboxymethyl Chitosan: An Innovation in New Natural Preservative from Shrimp Shell Waste with a Nutritional Value and Health Orientation. *Procedia Food Sci.* **3**, 35–51 (2015).

26. Xu, Y. & Du, Y. Effect of molecular structure of chitosan on protein deli v ery properties of chitosan nanoparticles. *Int. J. Pharm.* **250**, 215–226 (2003).

27. Fan, W., Yan, W., Xu, Z. & Ni, H. Formation mechanism of monodisperse, low molecular weight chitosan nanoparticles by ionic gelation technique. *Colloids and Surfaces B: Biointerfaces* vol. 90 21–27 (2012).

28. Kocak, N., Sahin, M., Akin, I., Kus, M. & Yilmaz, M. Microwave Assisted Synthesis of Chitosan Nanoparticles. *J. Macromol. Sci. Part A* **48**, 776–779 (2011).

29. Thandapani, G., Supriya Prasad, P., Sudha, P. N. & Sukumaran, A. Size optimization and in vitro biocompatibility studies of chitosan nanoparticles. *Int. J. Biol. Macromol.* **104**, 1794–1806 (2017).

30. Anitha, A., Maya, S., Deepa, N., Chennazhi, K. P., Nair, S. V. & Jayakumar, R. Curcumin-Loaded N,O-Carboxymethyl Chitosan Nanoparticles for Cancer Drug Delivery. *J. Biomater. Sci. Polym. Ed.* **23**, 1381–1400 (2012).

31. Bugnicourt, L., Alcouffe, P. & Ladavière, C. Elaboration of chitosan nanoparticles: Favorable impact of a mild thermal treatment to obtain finely divided, spherical, and colloidally stable objects. *Colloids Surfaces A Physicochem. Eng. Asp.* **457**, 476–486 (2014).

32. Tanjung, F. A., Husseinsyah, S., Hussin, K. & Hassan, A. Mechanical and thermal properties of organosolv lignin/sodium dodecyl sulphate binary agent-treated polypropylene/chitosan composites. *Polym. Bull.* **73**, 1427–1445 (2016).

33. Topolniak, I., Gardette, J. L. & Therias, S. Influence of zeolite nanoparticles on photostability of ethylene vinyl alcohol copolymer (EVOH). *Polym. Degrad. Stab.* **121**, 137–148 (2015).

34. Barkoula, N. M., Alcock, B., Cabrera, N. O. & Peijs, T. Fatigue properties of highly oriented polypropylene tapes and all-polypropylene composites. *Polym. Polym. Compos.* **16**, 101–113 (2008).

35. Hein, S., Wang, K., Stevens, W. F. & Kjems, J. Chitosan composites for biomedical applications: status, challenges and perspectives. *Mater. Sci. Technol.* **24**, 1053–1061 (2008).

36. Peniche, C., Argüelles-Monal, W. & Goycoolea, M. Chitin and Chitosan : Major Sources , Properties and Applications. *Monomers, Polym. Compos. from Renew. Resour.* **1**, 517–542 (2008).

37. Fernandez-Saiz, P., Ocio, M. J. & Lagaron, J. M. Antibacterial chitosan-based blends with ethylene-vinyl alcohol copolymer. *Carbohydr. Polym.* **80**, 874–884 (2010).

38. Keulder, L. The preparation of polyolefin nanofibres by solution electrospinning (PhD). (University Stellenbosch, 2013).

39. Zong, H., Xia, X., Liang, Y., Dai, S., Alsaedi, A., Hayat, T., Kong, F. & Pan, J. H. Designing function-oriented artificial nanomaterials and membranes via electrospinning and electrospraying techniques. *Mater. Sci. Eng. C* **92**, 1075–1091 (2018).

40. Haider, A., Haider, S. & Kang, I.-K. A comprehensive review summarizing the effect of electrospinning parameters and potential applications of nanofibers in biomedical and biotechnology. *Arab. J. Chem.* **11**, 1165–1188 (2018).

41. Sun, K. & Li, Z. H. Preparations, properties and applications of chitosan based nanofibers fabricated by electrospinning. *Express Polym. Lett.* **5**, 342–361 (2011).

42. Hulsey, S., Absar, S. & Choi, H. Comparative Study of Polymer Dissolution Techniques for Electrospinning. *Procedia Manuf.* **10**, 652–661 (2017).

43. Martínez-Sanz, M., Olsson, R. T., Lopez-Rubio, A. & Lagaron, J. M. Development of electrospun EVOH fibres reinforced with bacterial cellulose nanowhiskers. Part I: Characterization and method optimization. *Cellulose* **18**, 335–347 (2011).

44. Kenawy, E. R., Layman, J. M., Watkins, J. R., Bowlin, G. L., Matthews, J. A., Simpson, D. G. & Wnek, G. E. Electrospinning of poly(ethylene-co-vinyl alcohol) fibers. *Biomaterials* **24**, 907–913 (2003).

45. Le Grange, M. The use of fluorescence to probe the morphology changes in complex polymers (MSc). (University Stellenbosch, 2015).

46. Osvaldová, P. Fluorescence labelling of chitosan and its cationic derivatives for biological studies (MSc). (University of Iceland, 2017).

47. Nielsen, L. J., Eyley, S., Thielemans, W. & Aylott, J. W. Dual fluorescent labelling of cellulose nanocrystals for pH sensing. *Chem. Commun.* **46**, 8929–8931 (2010).

48. Zhao, J. & Wu, J. Preparation and Characterization of the Fluorescent Chitosan Nanoparticle Probe. *Chinese J. Anal. Chem.* **34**, 1555–1559 (2006).

49. Huang, M., Ma, Z., Khor, E. & Lim, L. Y. Uptake of FITC-chitosan nanoparticles by A549 cells. *Pharm. Res.* **19**, 1488–1494 (2002).

50. Steiner, G. & Koch, E. Trends in Fourier transform infrared spectroscopic imaging. *Anal. Bioanal. Chem.* **394**, 671–678 (2009).

51. Ngo, A. N., Ezoulin, M. J. M., Murowchick, J. B., Gounev, A. D. & Youan, B. B. C. Sodium Acetate Coated Tenofovir-Loaded Chitosan Nanoparticles for Improved Physico-Chemical Properties. *Pharm. Res.* **33**, 367–383 (2016).

52. Xie, Y., Xu, S., Hu, Y., Chen, W., He, Y. & Shi, X. Rapid identification and classification of staphylococcus aureus by attenuated total reflectance fourier transform infrared spectroscopy. *J. Food Saf.* **32**, 176–183 (2012).

53. Chen, S. C., Wu, Y. C., Mi, F. L., Lin, Y. H., Yu, L. C. & Sung, H. W. A novel pH-sensitive hydrogel composed of N,O-carboxymethyl chitosan and alginate cross-linked by genipin for protein drug delivery. *J. Control. Release* **96**, 285–300 (2004).

54. Sajomsang, W., Gonil, P. & Tantayanon, S. Antibacterial activity of quaternary ammonium chitosan containing mono or disaccharide moieties: Preparation and characterization. *Int. J. Biol. Macromol.* **44**, 419–427 (2009).

55. Kasaai, M. R. Determination of the degree of N-acetylation for chitin and chitosan by various NMR spectroscopy techniques: A review. *Carbohydr. Polym.* **79**, 801–810 (2010).

56. Abdel-Rahman, R. M., Hrdina, R., Abdel-Mohsen, A. M., Fouda, M. M. G., Soliman, A. Y., Mohamed, F. K., Mohsin, K. & Pinto, T. D. Chitin and chitosan from Brazilian Atlantic Coast: Isolation, characterization and antibacterial activity. *Int. J. Biol. Macromol.* **80**, 107–120 (2015).

57. Haque, A., Wang, Z., Chandra, S., Dong, B., Khan, L. & Hamlen, K. W. FUSION. in *Proceedings of the 2017 ACM on Conference on Information and Knowledge Management - CIKM '17* vol. 151 919–928 (ACM Press, 2017).

58. Hayes, E. R. N,O-Carboxymethyl chitosan and preparative method thereof. (1986).

59. Vernon-Parry, K. D. Scanning electron microscopy: an introduction. *III-Vs Rev.* **13**, 40–44 (2000).

60. Bugnicourt, L. & Ladavière, C. Interests of chitosan nanoparticles ionically cross-linked with tripolyphosphate for biomedical applications. *Prog. Polym. Sci.* **60**, 1–17 (2016).

61. Tran, H. V., Tran, L. D., Ba, C. T., Vu, H. D., Nguyen, T. N., Pham, D. G. & Nguyen, P. X. Synthesis, characterization, antibacterial and antiproliferative activities of monodisperse chitosan- based silver nanoparticles. *Colloids Surfaces A Physicochem. Eng. Asp.* **360**, 32–40 (2010).

62. Mahadik, D. B., Jung, H. N. R., Han, W., Cho, H. H. & Park, H. H. Flexible, elastic, and superhydrophobic silica-polymer composite aerogels by high internal phase emulsion process. *Compos. Sci. Technol.* **147**, 45–51 (2017).

63. Klein, M. P., Nunes, M. R., Rodrigues, R. C., Benvenutti, E. V., Costa, T. M. H., Hertz, P. F. & Ninow, J. L. Effect of the support size on the properties of β-galactosidase immobilized on chitosan: Advantages and disadvantages of macro and nanoparticles. *Biomacromolecules* **13**, 2456–2464 (2012).

64. Wang, Z., Zeng, R., Tu, M. & Zhao, J. Synthesis, characterization of biomimetic phosphorylcholine-bound chitosan derivative and in vitro drug release of their nanoparticles. *J. Appl. Polym. Sci.* **128**, 153–160 (2013).

65. Wang, X., Wei, J., Chen, J. & Tang, S. Improvement of surface hydrophilicity, water uptake, biodegradability, and cytocompatibility through the incorporation of chitosan oligosaccharide into poly(l-lactide). *J. Appl. Polym. Sci.* **135**, 1–9 (2018).

66. Yüce, M. Y., Demirel, A. L. & Menzel, F. Tuning the surface hydrophobicity of polymer/nanoparticle composite films in the wenzel regime by composition. *Langmuir* **21**, 5073–5078 (2005).

67. Milne, A. J. B., Elliott, J. A. W., Zabeti, P., Zhou, J. & Amirfazli, A. Model and experimental studies for contact angles of surfactant solutions on rough and smooth hydrophobic surfaces. *Phys. Chem. Chem. Phys.* **13**, 16208–16219 (2011).

68. Tan, H., Ma, R., Lin, C., Liu, Z. & Tang, T. Quaternized chitosan as an antimicrobial agent: Antimicrobial activity, mechanism of action and biomedical applications in orthopedics. *Int. J. Mol. Sci.* **14**, 1854–1869 (2013).

69. Khalil, A. M., Abdel-Monem, R. A., Darwesh, O. M., Hashim, A. I., Nada, A. A. & Rabie, S. T. Synthesis, Characterization, and Evaluation of Antimicrobial Activities of Chitosan and Carboxymethyl Chitosan Schiff-Base/Silver Nanoparticles. *J. Chem.* **2017**, (2017).

70. Divya, K. & Jisha, M. S. Chitosan nanoparticles preparation and applications. *Environ. Chem. Lett.* **16**, 101–112 (2018).

CHAPTER 3

EXPERIMENTAL

3.1 Materials

Chitosan (≥ 75% deacetylated) was used for the synthesis of a quaternary ammonium chitosan derivative (qC12) and *N,O*-carboxymethyl chitosan (*N,O*-CMC). The viscosity of the used chitosan (≥ 75% deacetylated) was determined to be 190-322 mPa.s, 1 wt% in 1% acetic acid (25°C, Brookfield). For the sake of comparison, the viscosity of advertised medium molecular weight chitosan was measured to be 80-177 mPa.s, 1 wt% in 1% acetic acid (25°C, Brookfield). Furthermore, chitosan and its synthesised derivatives were also used for nanoparticle production. The following chemicals were purchased from Sigma-Aldrich: sodium tripolyphosphate (technical grade, 85%), poly(vinyl alcohol-co-ethylene) with ethylene mole content of 27%, 38% and 44%, respectively, fluorescein 5(6)-isothiocyanate (≥ 90%), dimethyl amine solution (40 wt. % in H_2O), sodium borohydride (99%), 1-methyl-2-pyrrolidone (≥ 99.0%), 1-bromododecane (97%), acetic acid-d_4 (≥ 99.5 atom % D), and isopropanol (99.5%). Chemicals purchased from Merck were as follow: acetic acid (glacial), hydrochloric acid (32 wt. %), isobutyraldehyde (≥ 98%), formaldehyde solution (min 37 wt. %), deuterium oxide (D_2O) (99.96% for NMR) and dimethyl sulfoxide (Merck, purity (GC) ≥ 99%). Sodium hydroxide pearls (98-100.5%) was purchased from SCIENCEWORLD and chloroacetic acid flakes (99%) from ACROS. Low-density polyethylene (LDPE, Batch: LM2065), which was obtained from Sasol, was also used as a matrix. Freezer stock cultures of *Staphylococcus aureus* (*S. aureus*) were used for antimicrobial testing. Nitrotetrazolium Blue chloride (NBT) and alamarBlue was used for cell viability studies. Lastly, readily available methanol (≥ 99.5%), ethanol (≥ 99.5%), xylene (reagent grade), acetone (≥ 99.5%) and distilled water was used as needed.

3.2 Methods

As discussed in Chapter 2, chitosan possesses multiple functional groups. This includes hydroxyl and amino groups. These functional groups were investigated for possible functionalisation to influence polymer hydrophobicity and antimicrobial properties, relative to unmodified chitosan[1]. The relationship between chitosan hydrophobicity and antimicrobial properties is still not fully understood but the general observed trend is that hydrophobicity promotes antimicrobial properties[1]. The influence of the selected modification was determined by exposure to gram positive and gram negative bacteria, testing of hydrophobicity and evaluating the nanoparticle dispersions within polymer matrices.

3.2.1 Synthesis of quaternary chitosan derivative

The chitosan amine group was functionalised to create a quaternary ammonium chitosan derivative. A three-step process was followed[2]. Reagent amounts listed below were for a single reaction. These reactions were performed multiple times to synthesise appropriate amounts of quaternary chitosan for the purpose of nanoparticle production.

3.2.1.1 Synthesis of 3-dimethylamino-2,2-dimethylpropanal

The first step involved synthesising 3-dimethylamino-2,2-dimethylpropanal as modification agent, as shown in Figure 3.2.1-1. This was achieved by reacting equimolar amounts of isobutyraldehyde (50.40 g, 0.7 mol), aqueous formaldehyde solution (56.7 g, 0.7 mol) and a 40 % dimethylamine solution (78.75 g, 0.7 mol)[3]. The reaction was heated to 100°C and purged with N_2 gas for 5 hours. Afterwards, the N_2 gas was vented and the solution was refluxed for 24 hours.

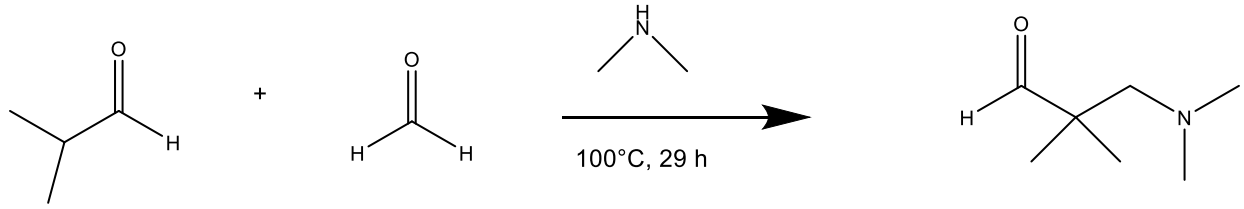

Figure 3.2.1-1: Synthesis of 3-dimethylamino-2,2-dimethylpropanal.

Figure 3.2.1-2 shows the different organic (bottom) and aqueous (top) layers, prior to separation. The separated organic phase was placed in a rotary evaporator at 80°C to remove additional aqueous solution.

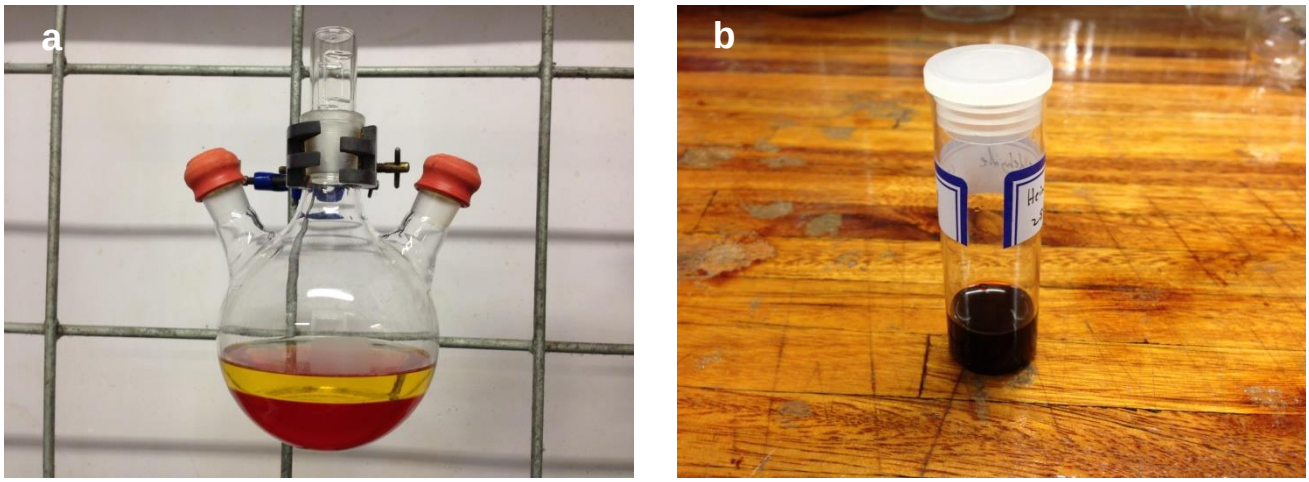

Figure 3.2.1-2: Gravity separated organic (bottom) and aqueous (top) layers with the orange organic layer containing 3-dimethylamino-2,2-dimethylpropanal (a) before separation and (b) 3-dimethylamino-2,2-dimethylpropanal after separation.

3.2.1.2 Synthesis of N-substituted chitosan

The second step involved synthesising *N*-substituted chitosan by using a reducing agent, $NaBH_4$, and the modification agent, 3-dimethylamino-2,2-dimethylpropanal, synthesised as described in the previous section[4]. The reaction scheme for this step is shown in Figure 3.2.1-3. Chitosan (3 g) was dissolved at room temperature in a 0.5% (w/v) acetic acid solution (300 mL). The modification agent (6.46 g, 0.05 mol) was added while being stirred. The reducing agent, $NaBH_4$ (5.68 g, 0.15 mol), was added as a 10 wt% solution (51 mL distilled water) to control the foaming which occurred during the addition to the reaction. The $NaBH_4$ was added 24 hours after the addition of the 3-dimethylamino-2,2-dimethylpropanal, and was allowed to react for an additional 24 hours. The *N*-substituted chitosan was then precipitated in acetone, filtered and dried for 24 hours at 60°C in a vacuum oven.

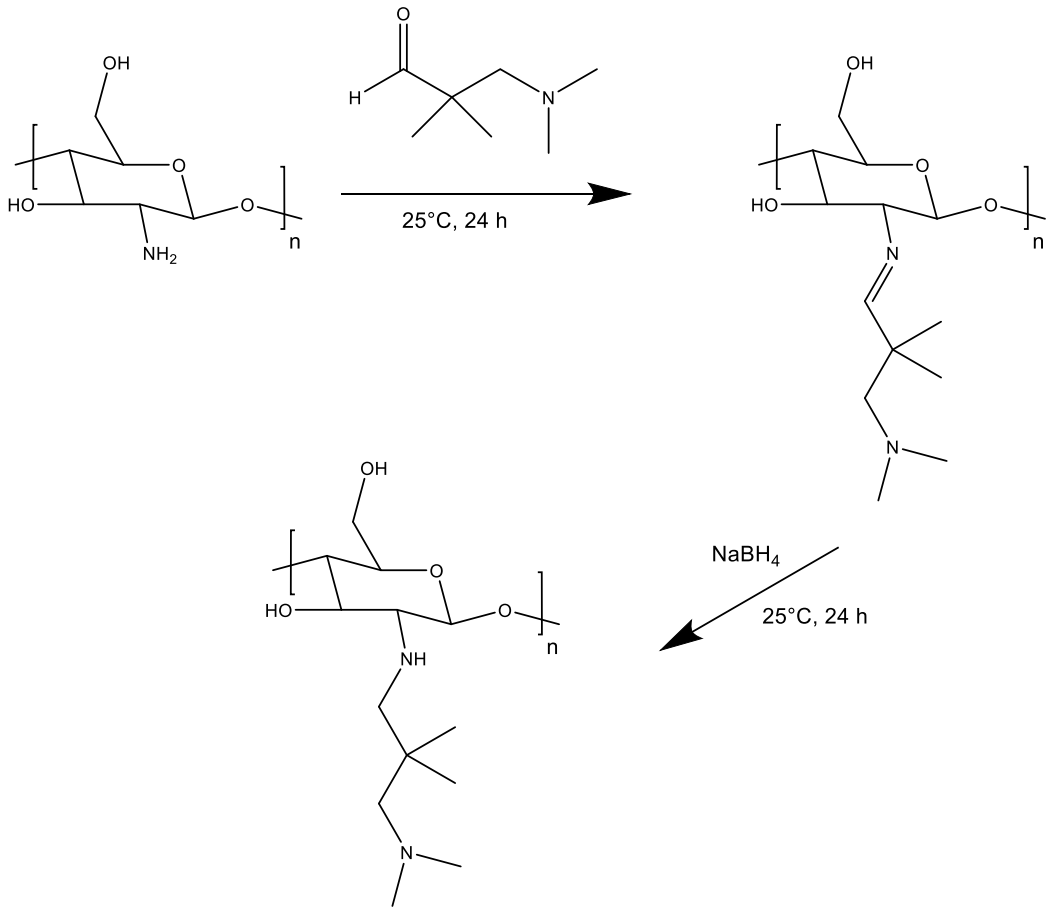

Figure 3.2.1-3: Synthesis of *N*-substituted chitosan using $NaBH_4$ and 3-dimethylamino-2,2-dimethylpropanal.

3.2.1.3 Synthesis of quaternary chitosan derivative (qC12)

The third and final step of the synthesis of quaternary ammonium chitosan involved the reaction of *N*-substituted chitosan with alkyl bromine. The reaction scheme in Figure 3.2.1-4 shows the

addition of an alkyl chain, which is twelve carbon atoms long, to the *N*-substituted chitosan. *N*-substituted chitosan (3 g) was suspended in *N*-methyl-2-pyrrolidone (150 mL) and acetic acid (1.5 mL) for 24 hours. 1-Bromododecane (27 g, 0.108 mol) was added dropwise, where after the reaction mixture was heated to 100°C and stirred for 48 hours. A yellow product formed, was precipitated in acetone, filtered and then dried for 24 hours at 60°C. This final product was used further for nanoparticle production.

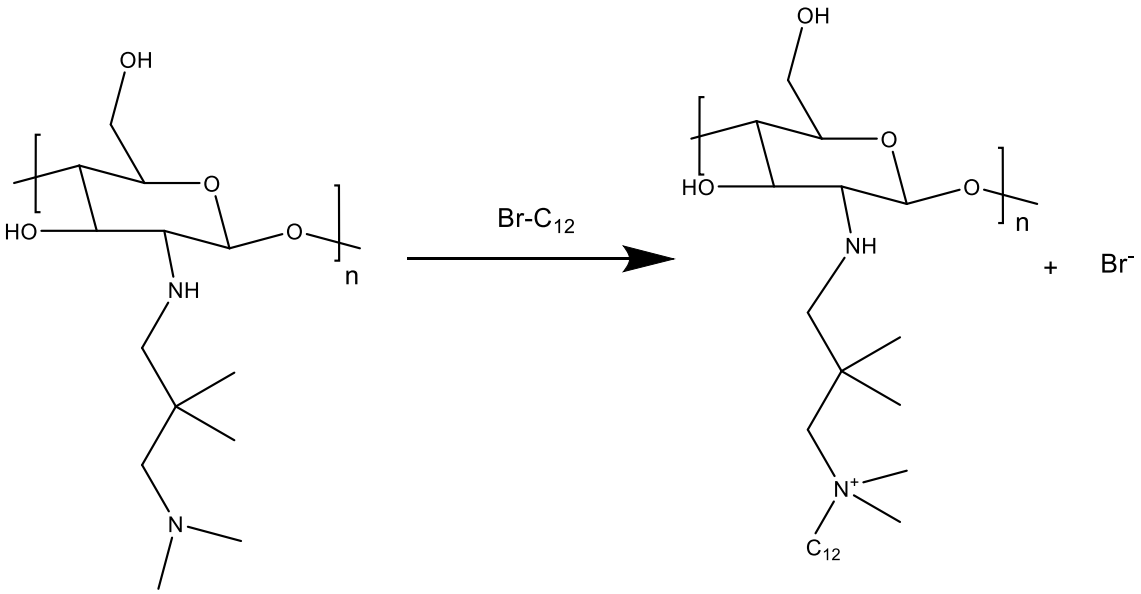

Figure 3.2.1-4: Synthesis of a quaternary ammonium chitosan (qC12) derivative from *N*-substituted chitosan.

3.2.2 N,O-carboxymethyl chitosan (*N,O*-CMC) derivative

N,O-carboxymethyl chitosan was synthesised to produce a chitosan derivative with a higher degree of hydrophilicity when compared to unmodified chitosan. A patented method by Hayes was followed[5]. The reaction scheme of the *N,O*-carboxymethylation is shown in Figure 3.2.2-1.

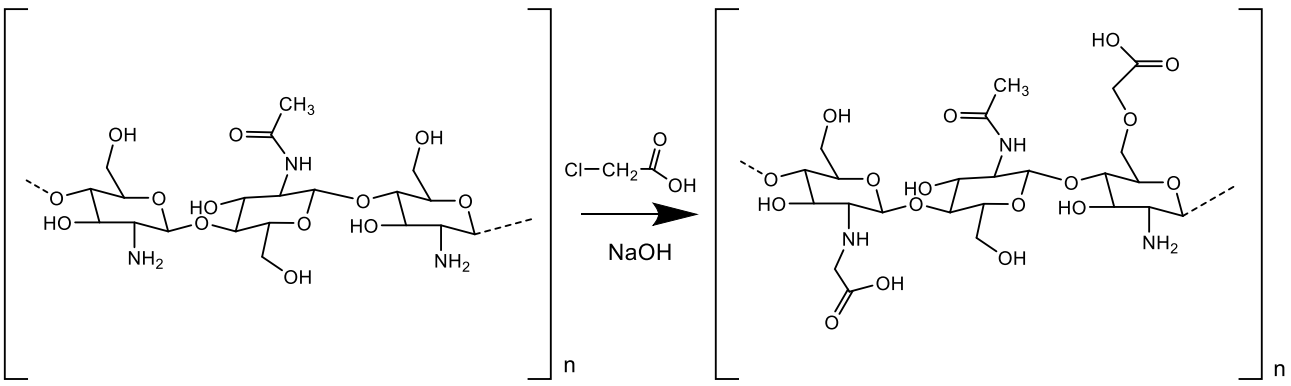

Figure 3.2.2-1: Chitosan functionalisation to *N,O*-carboxymethyl chitosan (*N,O*-CMC).

Chitosan (2 g) was added to isopropanol (20 mL) at 25°C. A 10 N solution of NaOH (2.016 g, 0.050 mol, 5.04 mL) was added as 6 portions in 4 minute intervals. The reaction was stirred for 45 minutes. Monochloroacetic acid (2.4 g, 0.025 mol) was added as 5 portions in 5 minute intervals. Afterwards, the reaction was heated to 60°C and stirred for 3 hours.

Distilled water (1.70 mL) was added to the mixture and the resulting pH was adjusted to 7 using glacial acetic acid and a pH meter. The resulting product was filtered and washed in 30 mL of a 70:30 (v/v) methanol/water mixture. Thereafter, the product was dispersed in dry methanol (30 mL), filtered and dried overnight at 60°C.

3.2.3 Nanoparticle production of chitosan and its derivatives

3.2.3.1 Production of unmodified chitosan nanoparticles

Unmodified chitosan nanoparticles were prepared by the ionotropic gelation method described by Xu & Du[6]. Chitosan (500 mg) was dissolved in 100 mL of a 1% (w/v) acetic acid solution and stirred at 400 rpm and 25°C. Sodium tripolyphosphate (TPP) (250 mg) was dissolved in distilled water (100 mL), where after the two different solutions were added together with a chitosan:TPP weight ratio of 2:1. The combined solution was stirred at 400 rpm for 30 mins before being centrifuged at 4200 rpm for 10 minute intervals. The supernatant was discarded, distilled water was added to the remaining nanoparticles and the centrifugation step was repeated. As soon as the supernatant appeared clear of unreacted reagents the chitosan nanoparticles were suspended in distilled water, sonicated for an hour and placed into dialysis tubing for a week to ensure neutralisation of the nanoparticles. The dialysis water was replaced twice a day. After dialysis, the remaining nanoparticles were sonicated for an hour to reduce agglomeration and lyophilised, prior to being incorporated into different polymer matrices.

3.2.3.2 Production of quaternary chitosan nanoparticles

The same experimental procedure was used as with the unmodified chitosan. Varying qC12:TPP weight ratios were investigated but ratios higher than 2:1 proved to result in insufficient crosslinking. Therefore, in order to obtain a maximum yield the weight ratio of 2:1 remained unchanged.

3.2.3.3 Production of N,O-carboxymethyl chitosan (N,O-CMC) nanoparticles

An ionotropic gelation method was used for the production of *N,O*-CMC nanoparticles, as described by Anitha *et al*[7]. *N,O*-carboxymethyl chitosan (500 mg) was dissolved in a 0.75% (w/v) acetic acid solution (100 mL). The addition of acetic acid to the solution was necessary to protonate the *N,O*-CMC amine group so that crosslinking could occur. TPP (100 mg) was dissolved in distilled water (40 mL) and added to the *N,O*-CMC solution. The mixture was

stirred for 30 minutes at 400 rpm and 25°C. The nanoparticles were centrifuged in 10 minute intervals at 5000 rpm and washed with distilled water until the supernatant appeared clear. The remaining nanoparticles were placed in dialysis tubing for a week to reach a neutral pH of 7. The dialysis water was replaced twice a day. The same sonication and lyophilisation method was used as described in the case of the unmodified chitosan nanoparticles.

3.2.4 Preparation of poly(vinyl alcohol-co-ethylene) (EVOH) nanocomposite films

The lyophilised nanoparticles were incorporated into EVOH films of varying ethylene content. From here on EVOH27, EVOH38 and EVOH44 denotes EVOH copolymers with an ethylene mole content of 27, 38 and 44%, respectively. Each EVOH polymer (500 mg) was dissolved under reflux at 100°C in a 70:30 (v/v) isopropanol/water solvent mixture (20 mL) for two hours. This produced solutions with a polymer content of 3 wt%. A 50:50 (m/m) blend of Irganox 1010 and Irgafos 165 was added as thermal stabilisers. The stabilisers were added as 2 wt%, relative to the polymer content. The previously lyophilised nanoparticles were suspended in distilled water (10 mg/mL) and sonicated for an hour to redisperse the particles and reduce nanoparticle agglomeration. Thereafter, the nanoparticles were added to the polymer solution for the final 30 minutes of the dissolution process. This process was followed for all three variants of EVOH polymers and for the unmodified as well as quaternary ammonium chitosan nanoparticles. The nanocomposites which contained *N,O*-CMC nanoparticles had to be prepared by dissolving EVOH and suspending the nanoparticles in dimethyl sulfoxide (DMSO). It was found that the *N,O*-CMC nanoparticles agglomerated in isopropanol/water mixtures and could therefore not be distributed throughout the EVOH matrices. The nanocomposite materials discussed above were produced with nanoparticle content up to 8 wt%, relative to the EVOH content.

After the complete dissolution of the EVOH pellets and the introduction of the nanoparticles the solutions were cast into glass petri dishes and left open to the atmosphere to allow the solvent to evaporate overnight. Afterwards, the films were placed in a vacuum oven at 40°C for 24 hours to ensure no solvent was retained within the films. The composites which were dissolved in DMSO were kept in the vacuum oven at 60°C for one week. The dried films were crushed into powders, using a mortar and pestle, as the solvent casting method did not produce films of uniform thickness. These powders were used further to produce uniform composite films and electrospun nanofibres.

Table 3.2.4-1 summarises the different components used for the preparation of the nanocomposite films.

Table 3.2.4-1: Summary of nanocomposite materials used in the case of the EVOH matrices

Polymer	Filler material	Nanoparticle loading (wt%)	Solvent
Poly(vinyl alcohol-co-ethylene) (EVOH27)	Unmodified chitosan nanoparticles	0%	Isopropanol/water 70:30 (v/v)
		1%	
		3%	
		5%	
		8%	
	Quaternary ammonium chitosan nanoparticles	1%	
		3%	
		5%	
		8%	
	Carboxymethyl chitosan nanoparticles	1%	Dimethyl sulfoxide
		3%	
		5%	
		8%	
Poly(vinyl alcohol-co-ethylene) (EVOH38)	Unmodified chitosan nanoparticles	0%	Isopropanol/water 70:30 (v/v)
		1%	
		3%	
		5%	
		8%	
	Quaternary ammonium chitosan nanoparticles	1%	
		3%	
		5%	
		8%	
	Carboxymethyl chitosan nanoparticles	1%	Dimethyl sulfoxide
		3%	
		5%	
		8%	
Poly(vinyl alcohol-co-ethylene) (EVOH44)	Unmodified chitosan nanoparticles	0%	Isopropanol/water 70:30 (v/v)
		1%	
		3%	
		5%	
		8%	
	Quaternary ammonium chitosan nanoparticles	1%	
		3%	
		5%	
		8%	
	Carboxymethyl chitosan nanoparticles	1%	Dimethyl sulfoxide
		3%	
		5%	
		8%	

A Graseby Specac manual hydraulic press was used to create uniform composite films. Nanocomposite powder (100 mg) was placed between two teflon sheets and subjected to heating so that the EVOH matrices would melt. The composites were heated to 200, 176 and 163°C for the EVOH27, EVOH38 and EVOH44 matrices, respectively. After 1 minute of heating, a loading of 3 tons was applied to the sample for 2 minutes. This process was repeated three times for each sample with the aim to improve the nanoparticle distribution throughout the film. Film thickness was confirmed using a micrometer.

3.2.5 Preparation of low-density polyethylene (LDPE) nanocomposite films

A similar film forming process was followed for the preparation of LDPE nanocomposite films, as discussed in Chapter 3.2.4. However, in this case the LDPE was dissolved in xylene for one hour under reflux at 90°C. All three variations of nanoparticles were suspended in DMSO as none would disperse in xylene and only two dispersed in the isopropanol/water blend. The solvent cast films were left in a vacuum oven at 40°C for 24 hours. Finally, the melt-pressing process was also similar to the EVOH nanocomposites, except that the LDPE nanocomposites were melted at 110°C. Table 3.2.5-1 summarises the components used to prepare the LDPE nanocomposite films.

Table 3.2.5-1: Summary of nanocomposite materials used in the case of the LDPE matrices

Polymer	Filler material	Nanoparticle loading (wt%)	Solvent
Low-density polyethylene (LDPE)	Unmodified chitosan nanoparticles	0%	Xylene (matrix), Dimethyl sulfoxide (filler)
		1%	
		3%	
		5%	
		8%	
	Quaternary ammonium chitosan nanoparticles	1%	
		3%	
		5%	
		8%	
	Carboxymethyl chitosan nanoparticles	1%	
		3%	
		5%	
		8%	

3.2.6 Preparation of poly(vinyl alcohol-co-ethylene) (EVOH) nanocomposite fibres

Nanofibres were electrospun using the same nanocomposite powders which were used to create polymer films. An in-house built electrospinning setup was used, as shown in Figure 3.2.6-1 and discussed in Chapter 2. Nanocomposites containing EVOH27, EVOH38 and

EVOH44 were dissolved in DMSO to make up polymer solutions of 20, 15 and 15 wt%, respectively. Electrospinning was done at a polymer solution flow rate of 0.002 mL/min, a tip to collector distance (TCD) of 25 cm and an applied voltage of 10 kV. These were the initial operating conditions and were manipulated as the polymer solution composition changed. The nanofibres were collected onto an aluminium plate for further analysis.

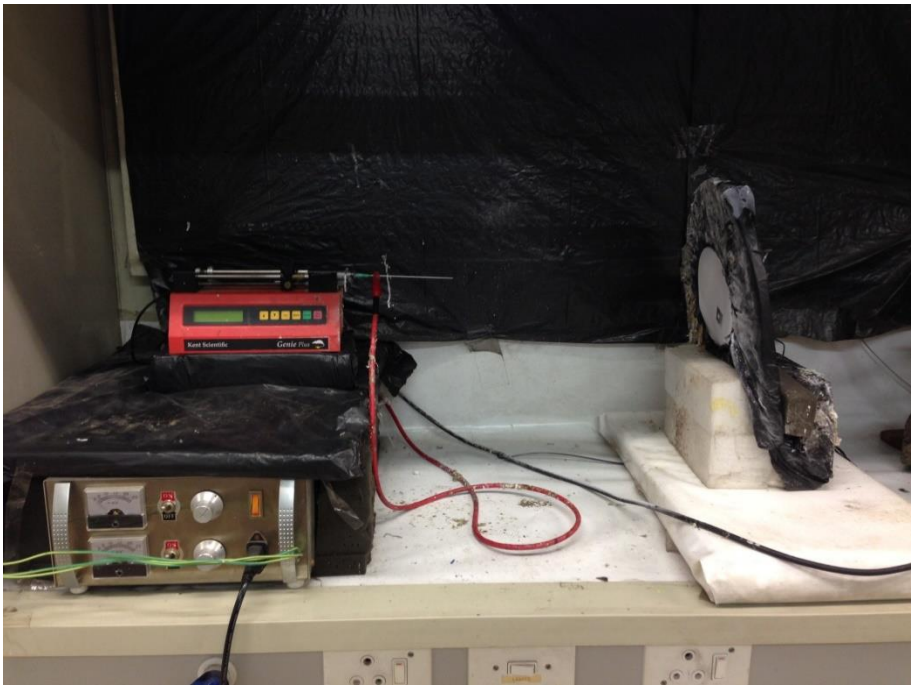

Figure 3.2.6-1: Illustration of the electrospinning setup used to produce nanofibres.

3.2.7 Fluorescent labelling of chitosan nanoparticles and its derivatives

A single fluorescent labelling method was followed for all three chitosan nanoparticle derivatives[8–10]. Lyophilised nanoparticles (250 mg) were suspended in distilled water (25 mL) and sonicated for an hour. Fluorescein isothiocyanate (FITC) (10.8 mg) was also suspended and sonicated in water (1 mL) for 10 minutes, prior to being added to the nanoparticles. The solution was stirred in the dark for 72 hours, centrifuged and washed with water. Thereafter, the nanoparticles were placed in dialysis tubing with distilled water for 7 days to remove any remaining impurities and fluorescent dye. The dialysis water was replaced twice a day to ensure a concentration gradient across the dialysis membrane. After a week of dialysis the labelled nanoparticles were lyophilised.

3.3 Characterisation techniques

3.3.1 Attenuated total reflectance - Fourier transform infrared (ATR-FTIR) spectroscopy

Infrared spectra data was obtained using a Thermo-Fisher Nicolet iS10 instrument in attenuated total reflectance (ATR) mode with a diamond ATR crystal. The spectra of all samples were produced from 64 individual scans, with a resolution of 4 cm^{-1}. Spectra were recorded in the range of 4000 cm^{-1} to 650 cm^{-1}. Data acquisition and processing were performed on Thermo-Fischer Scientific Inc. Omnic 8.1 software. No sample preparation was required as samples were analysed in the solid state.

3.3.2 Nuclear magnetic resonance (NMR) spectroscopy

Chitosan and its functionalised derivatives were subjected to ^{1}H NMR and ^{13}C NMR for structural analysis. Samples were analysed by 300, 400 and 600 MHz Agilent NMR spectrometers. The functionalised *N,O*-CMC was dissolved in D_2O, while the remaining samples were dissolved in 70:30 (v/v) mixtures of D_2O: Acetic acid-d_4. A Dual Broad Band Probe and 5 mm Indirect Detection PFG Probe was used for the ^{13}C NMR and ^{1}H NMR, respectively.

3.3.3 Scanning electron microscopy (SEM)

A Zeiss MERLIN Scanning Electron Microscope, together with Zeiss SmartSEM software, was used to obtain SEM micrographs of samples. All submitted samples were attached to double sided carbon tape and mounted onto specimen stubs. The fixed samples were subjected to a carbon coating process to make the sample surfaces electrically conductive. Samples which were submitted for elemental analysis were coated with a gold layer.

3.3.4 Thermogravimetric analysis (TGA)

The thermal stability of chitosan and its synthesised derivatives were evaluated with a TGA Q500 TA instrument. Samples were weighed off (1-5 mg) and placed in aluminium pans. Each sample was subjected to a heating cycle of 10°C/min up to a temperature of 600°C. The weight loss of the sample was recorded throughout and was used to determine the temperature at which the chitosan samples started to degrade.

3.3.5 Differential scanning calorimetry (DSC)

DSC was performed by using a DSC Q100 TA instrument. Nanocomposite samples of EVOH and LDPE were analysed to gather thermal data. Samples with varying filler content were sent through a similar analysis to investigate the influence of filler content on the thermal properties of the nanocomposites. Samples were weighed off (4-7 mg) and placed in DSC aluminium pans. All samples were subjected to three heating cycles. The first heating cycle was intended

to remove any thermal history the samples might have had. The first cycle heated the samples to 200°C and maintained it for 5 minutes. The second cycle cooled the sample down to 0°C. The third cycle increased the temperature to 200°C once again. All three heating cycles progressed at a rate of 10°C/min. The N_2 gas flow rate was kept constant at 2 mL/min and the thermal properties of the samples were recorded for the second and third temperature cycles.

3.3.6 Fluorescence spectroscopy

A Perkin Elmer LS 50 B luminescence spectrometer was used to analyse neat fluorescent dye and fluorescently labelled nanoparticles. This was done to confirm the attachment of the fluorescent dye to the nanoparticles and to determine the absorbance and emission wavelengths of the dye. The labelled nanoparticles and neat dye were suspended with distilled water prior to being transferred into spectrometer cuvettes.

The spectrometer performed a pre-scan on the neat FITC dye, which was suspended in distilled water, and was operated between wavelengths of 200-700 nm. From the pre-scan it was found that the FITC dye, in distilled water, was excited by light at a wavelength of 490 nm and emitted light at 519 nm. Therefore, the FITC-labelled nanoparticles were excited using light with a wavelength of 490 nm and if the nanoparticles emitted light at 519 nm it would confirm that the FITC dye successfully attached to the nanoparticles.

3.3.7 Confocal fluorescence microscopy (CFM)

A Carl Zeiss Confocal LSM 780 Elyra S1 was used for CFM sample analysis. Samples which contained fluorescently labelled nanoparticles, as discussed in Chapter 3.2.7, were submitted for confocal microscopy to probe the distribution of nanoparticles throughout polymer matrices. This was done by investigating varying magnifications and by performing z-stack analysis on nanocomposite samples. A z-stack provided a 3-dimensional representation of the nanoparticle distribution within the nanocomposites, by probing different depths of the samples. A laser with a wavelength of 488 nm was used as this was close to the excitation wavelength of the FITC fluorescent dye.

Samples were placed onto microscope slides and enclosed with a cover slip to protect the microscope objectives and prevent sample movement during analysis.

3.3.8 Static contact angle (SCA) measurements

A Krüss Drop Shape Analyzer was used to perform water contact angle tests on the nanocomposite films and fibres. A water droplet (2 µL) was deposited onto the sample surface and the contact angle was measured after 3 seconds using Advanced Laboratories Solutions software. Contact angle results were taken as the average of 10 measurements. Water contact angle measurements were done under ambient conditions of 25°C and 61% relative humidity.

3.3.9 Water uptake

Water uptake measurements were taken of all nanocomposite films and fibres to supplement water contact angle results. The composite samples were placed in distilled water (0.5 mg/mL) and heated to 37°C. Weight measurements were taken in triplicate over 2 hour periods. The formula below was used to determine the water uptake of each film

$$Water\ uptake\ (\%) = 100\ \times (W_t - W_o)/W_t \qquad \text{Equation 3.3.9-1}$$

with W_o as the initial composite weight and W_t being the composite weight at the measured time. The composite fibres were subjected to similar tests but they were submerged in distilled water for at least 24 hours to determine maximum water uptake.

3.3.10 UV-vis spectroscopy

An Analytik Jena - Specord 210 Plus UV/Vis photometer was used to evaluate the transparency of the nanocomposite films as the nanoparticle loading was increased. The transparency of the films was measured by fixing the solid films to the surface of the measuring cuvette and ensuring that the film surface remained smooth. Any creases on the film could negatively impact reproducibility. The slit size was kept at a standard 1 nm resolution, the lamp change occurred at 320 nm, the amount of data points was set at 0.1 nm intervals and the measuring speed was 50 nm/s. The maximum scan range of 190 – 1100 nm was used for all composite films. All sampling was performed in triplicate to ensure reproducibility and a blank cuvette was used as a reference.

3.3.11 Antimicrobial testing

Antimicrobial studies were performed on the created nanocomposite materials by making use of a modified disk diffusion method. Figure 3.3.11-1 shows the layout of the tested nanocomposite samples.

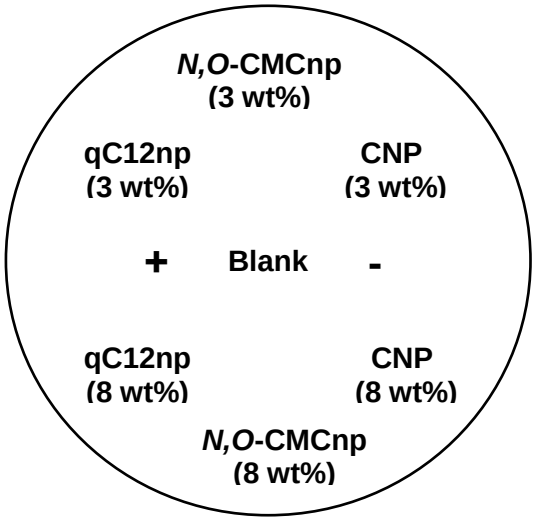

Figure 3.3.11-1: Top view layout of nanocomposite samples in LB media and petri dishes.

Freezer stock cultures of *S. aureus* were grown overnight in Luria Bertani (LB) media. The *S. aureus* was diluted to 10^5 colony forming units (CFUs)/mL and 0.5 mL was streaked out onto LB agar plates. This produced approximately 800 organisms per cm^2 of sample. Each sample was exposed to the organisms for 5 seconds before it was turned upwards. By turning the exposed sample area to face upwards, direct inhibition and halo formation could be observed for each sample, after incubation. Direct inhibition was tested immediately by staining the exposed sample areas with 5 µL of 3% alamarBlue solution. Metabolic activity of the organisms was shown by the colour change of the alamarBlue from blue to pink. The plates were then incubated for 72 hours at 37°C to investigate halo formation and the evolution of the direct inhibition. After the incubation period, the agar plates were stained with NBT to visualise the growth inhibition caused by the nanocomposite samples.

3.3.12 Rheometry

An Anton Paar Modular Compact Rheometer MCR 302 was used to conduct rheology experiments. Data analysis was performed using RheoCompass software. Nanocomposite electrospinning solutions were subjected to flow curve analysis at 22°C to observe the relationship between nanoparticle content and electrospinning solution viscosity.

3.3.13 Tensile testing

Tensile testing was performed on an INSTRON 4444 with INSTRON Series IX software at 20°C and 65% relative humidity. Experiments were performed with a constant ramp rate of 2 kN/min and speed of 50 mm/min. The LDPE and EVOH44 nanocomposite powders were shaped into dumbbells using a Graseby Specac manual hydraulic press and a dumbbell stencil with dimensions shown in Figure 3.3.13-1. Dumbbell thickness varied in the range of 0.66-0.82 mm. Each nanocomposite sample was tested 5 times and the thickness of each sample was measured to improve the accuracy of the stress-strain curves.

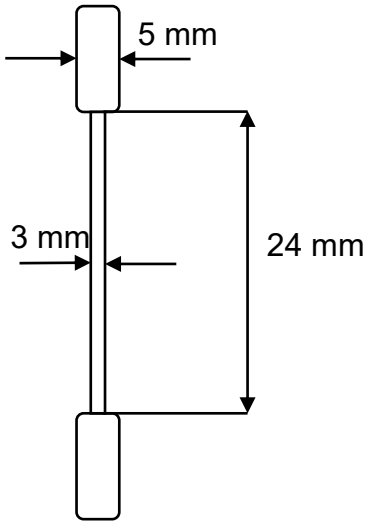

Figure 3.3.13-1: Dumbbell stencil dimensions used for tensile testing sample preparations.

3.4 References

1. Sahariah, P. & Másson, M. Antimicrobial Chitosan and Chitosan Derivatives: A Review of the Structure-Activity Relationship. *Biomacromolecules* **18**, 3846–3868 (2017).

2. Smit, M. Polymer-coated magnetic nanoparticles and modified polymer nanofibers for the efficient capture of Mycobacterium tuberculosis (Mtb) (MSc). (Stellenbosch University, 2018).

3. Bernhagen, W., Falk, V., Springer, H., Weber, J., Wiebus, E. & Kniep, C. Process for preparing 3-dimethylamino-2,2-dimethylpropanal. (1985).

4. Guo, Z., Xing, R., Liu, S., Zhong, Z., Ji, X., Wang, L. & Li, P. Antifungal properties of Schiff bases of chitosan, N-substituted chitosan and quaternized chitosan. *Carbohydr. Res.* **342**, 1329–1332 (2007).

5. Hayes, E. R. N,O-Carboxymethyl chitosan and preparative method thereof. (1986).

6. Xu, Y. & Du, Y. Effect of molecular structure of chitosan on protein deli v ery properties of chitosan nanoparticles. *Int. J. Pharm.* **250**, 215–226 (2003).

7. Anitha, A., Maya, S., Deepa, N., Chennazhi, K. P., Nair, S. V. & Jayakumar, R. Curcumin-Loaded N,O-Carboxymethyl Chitosan Nanoparticles for Cancer Drug Delivery. *J. Biomater. Sci. Polym. Ed.* **23**, 1381–1400 (2012).

8. Huang, M., Ma, Z., Khor, E. & Lim, L. Y. Uptake of FITC-chitosan nanoparticles by A549 cells. *Pharm. Res.* **19**, 1488–1494 (2002).

9. Geisberger, G., Gyenge, E. B., Maake, C. & Patzke, G. R. Trimethyl and carboxymethyl chitosan carriers for bio-active polymer-inorganic nanocomposites. *Carbohydr. Polym.* **91**, 58–67 (2013).

10. Osvaldová, P. Fluorescence labelling of chitosan and its cationic derivatives for biological studies (MSc). (University of Iceland, 2017).

CHAPTER 4

RESULTS AND DISCUSSION – CHARACTERISATION OF FUNCTIONALISED CHITOSAN NANOPARTICLES

4.1 Introduction

Chitosan was functionalised to change the hydrophilic nature of the polymer as described in Chapter 3.2.1 and Chapter 3.2.2. Unmodified chitosan and the two functionalised derivatives underwent ionotropic crosslinking with sodium tripolyphosphate (TPP) to produce nanoparticles. The functionalised chitosan and produced nanoparticles were characterised by techniques such as fourier transform infrared spectroscopy (FTIR), nuclear magnetic resonance (NMR), thermogravimetric analysis (TGA), scanning electron microscopy (SEM) and fluorescence spectroscopy. The hydrophobic quaternary ammonium chitosan derivative will be referred to as qC12 and the hydrophilic *N,O*-carboxymethyl chitosan derivative will be referred to as *N,O*-CMC in this chapter. Unmodified chitosan nanoparticles will be referred to as CNP, quaternary ammonium chitosan as qC12np and *N,O*-carboxymethyl chitosan as *N,O*-CMCnp.

4.2 Fourier transform infrared (FTIR) analysis

4.2.1 Unmodified chitosan nanoparticles

The FTIR spectra of unmodified chitosan, TPP and unmodified chitosan nanoparticles can be seen in Figure 4.2.1-1. In the spectrum for unmodified chitosan, the broad band at 3356 cm^{-1} is assigned to N-H and O-H stretching vibrations[1,2]. The bands at 2900 cm^{-1} and 2873 cm^{-1} are assigned to symmetric and anti-symmetric C-H stretching vibrations. The presence of amide groups are confirmed by amide I (1644 cm^{-1}), amide II (1579 cm^{-1}) and amide III (1316 cm^{-1}). The $–CH_2$ bending and O-H deformation vibrations are represented by the bands present at 1418 cm^{-1} and 1374 cm^{-1}.

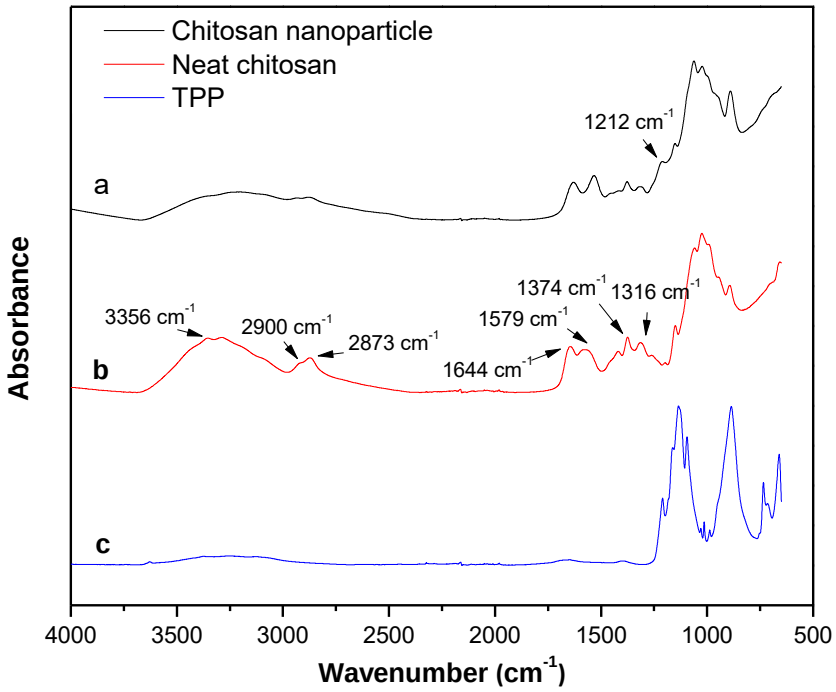

Figure 4.2.1-1: ATR-FTIR spectra of (a) unmodified chitosan nanoparticles, (b) unmodified chitosan and (c) TPP.

The characteristic bands of the unmodified chitosan were compared to the spectrum of CNPs, which consist of unmodified chitosan and TPP. The band associated with the stretching vibrations of N-H and O-H became wider for the CNPs. This indicates enhanced hydrogen bond interaction[1,2]. The amide II band shifted to a lower wavenumber in the nanoparticle spectrum. This is attributed to the interaction of TPP anions with the amino group of chitosan[1,2]. The peak at 1212 cm^{-1} is assigned to P=O stretching of TPP. This indicates the presence of TPP in the CNP samples.

4.2.2 Quaternary chitosan (qC12) nanoparticles

Figure 4.2.2-1 illustrates the different FTIR spectra of unmodified chitosan, *N*-substituted chitosan and quaternised chitosan. The peaks at 1406 cm^{-1} and 1349 cm^{-1} for *N*-substituted chitosan are assigned to methyl bending vibrations[3,4]. With regards to the quaternised chitosan, the peak at 1641 cm^{-1} is assigned to the quaternary ammonium salt[3,5]. The bands at 2924 cm^{-1} and 2855 cm^{-1} are assigned to C-H stretches which are present in the quaternised chitosan. This was due to the alkyl chain which was substituted onto the chitosan polymer and thus suggests successful quaternisation of the unmodified chitosan[3,6]. The peak at 1375 cm^{-1} is associated with the bending vibration of the methyl group, while the series of bands between 1150 cm^{-1} and 1350 cm^{-1} indicate the methylene bending vibrations of the attached alkyl chain[3,6].

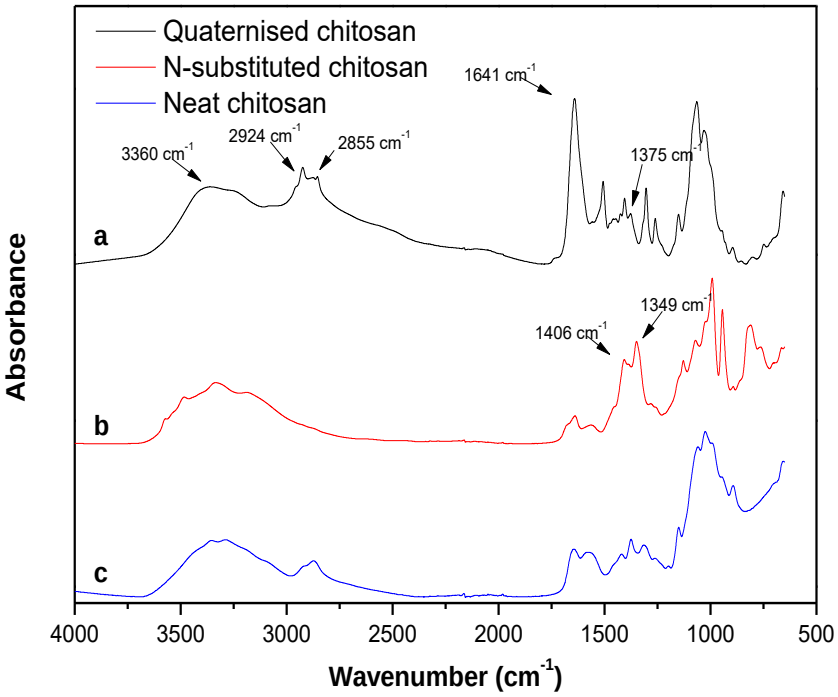

Figure 4.2.2-1: ATR-FTIR spectra of (a) quaternised chitosan, (b) *N*-substituted chitosan and (c) unmodified chitosan.

As mentioned in Chapter 4.2.1, the N-H and O-H stretching band became larger for the FTIR spectra of the quaternised chitosan nanoparticles and indicated increased hydrogen bond interaction. The presence of the TPP crosslinker is confirmed through its characteristic peaks at 1216 cm^{-1} for P=O stretching and 1062 cm^{-1} for P-O bending, as shown in Figure 4.2.2-2.

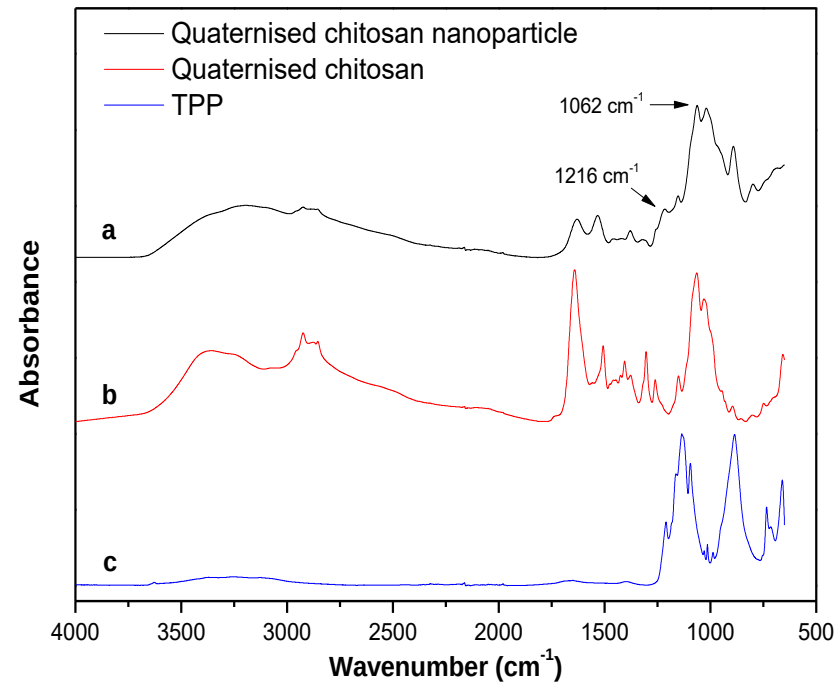

Figure 4.2.2-2: ATR-FTIR spectra of (a) quaternised chitosan nanoparticles, (b) quaternised chitosan and (c) TPP.

4.2.3 N,O-carboxymethyl chitosan (N,O-CMC) particles

Figure 4.2.3-1 shows the FTIR spectra for unmodified chitosan and its *N,O*-CMC derivative. Regarding the spectra for the unmodified chitosan, the peak at 1644 cm^{-1} corresponds to the amino group in the biopolymer. When compared to the *N,O*-CMC spectra it is noted that there is a strong peak at 1579 cm^{-1} which is assigned to the carboxylic acid salt ($-COO^-$ stretch) of the functionalisation. This suggests successful carboxymethyl addition to the chitosan polymer.

In the *N,O*-CMC spectra it is noted that the peak associated with the primary hydroxyl group of chitosan shows a decrease in intensity relative to the secondary hydroxyl group peak, which isn't influenced by the functionalisation. The decrease in relative intensity of the primary- and secondary hydroxyl groups suggests that *O*-substitution did indeed take place and confirms *N,O*-functionalisation[7,8].

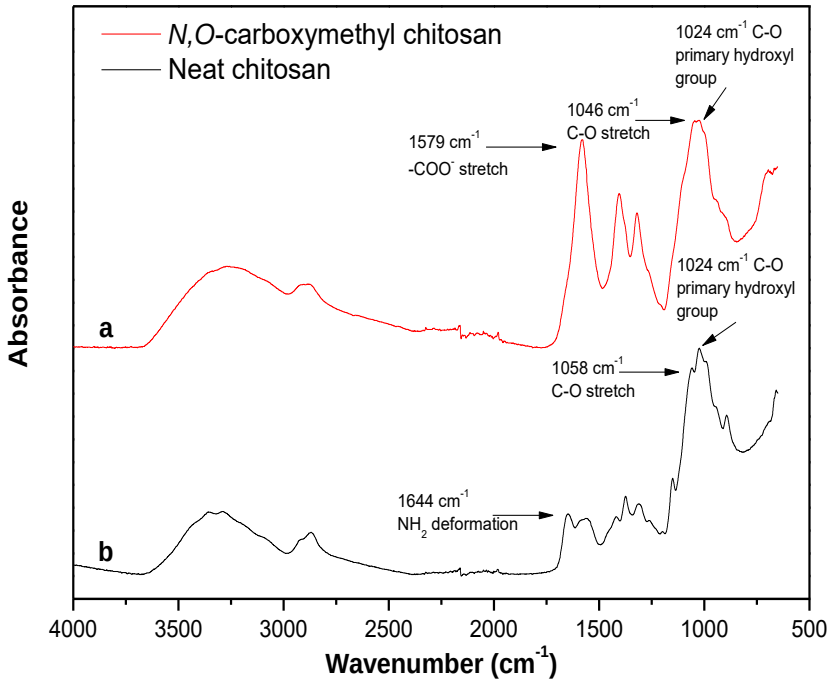

Figure 4.2.3-1: ATR-FTIR spectra of (a) *N,O*-carboxymethyl chitosan and (b) unmodified chitosan (bottom).

The FTIR data in Figure 4.2.3-2 shows the spectra of *N,O*-CMC and its produced nanoparticles. The appearance of the peak at 1618 cm^{-1} for the nanoparticle spectra is attributed to the interaction between the phosphate groups of the TPP crosslinker and the *N,O*-CMC ammonium ions[9].

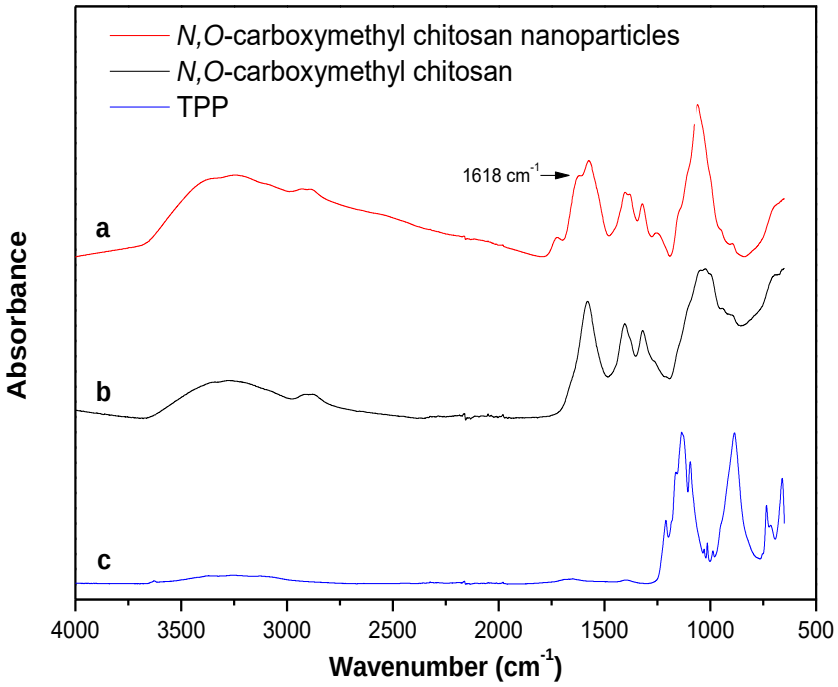

Figure 4.2.3-2: ATR-FTIR spectra of (a) *N,O*-carboxymethyl chitosan nanoparticles, (b) *N,O*-carboxymethyl chitosan and (c) TPP.

4.3 Nuclear Magnetic Resonance (NMR) analysis

4.3.1 Unmodified chitosan

The chitosan that was used in this research was purchased with a reported degree of *N*-deacetylation (DDA) of >75%. This was confirmed by ^{1}H NMR and reported below.

The ^{1}H NMR of the unmodified chitosan is shown in Figure 4.3.1-1. The peak at 4.90 ppm represents the methine protons of the carbon 1 (C1) on the chitosan backbone. The peak at 3.92 ppm can be assigned to the C3 and C4 methine protons, together with the C6 methylene protons. The C5 methine proton can be assigned to the overlapping peak area at 3.74 ppm. The methine proton at C2 can be assigned to the peak at 3.21 ppm and was used as a reference peak for the calculation of the DDA. Previous studies have used the methine proton peak at C1 for these calculations but this signal was overlapped by the peak signals of the solvent system[10]. The peak at 1.28 ppm represents the acetamido groups of the chitin residue and was also used in calculating the DDA.

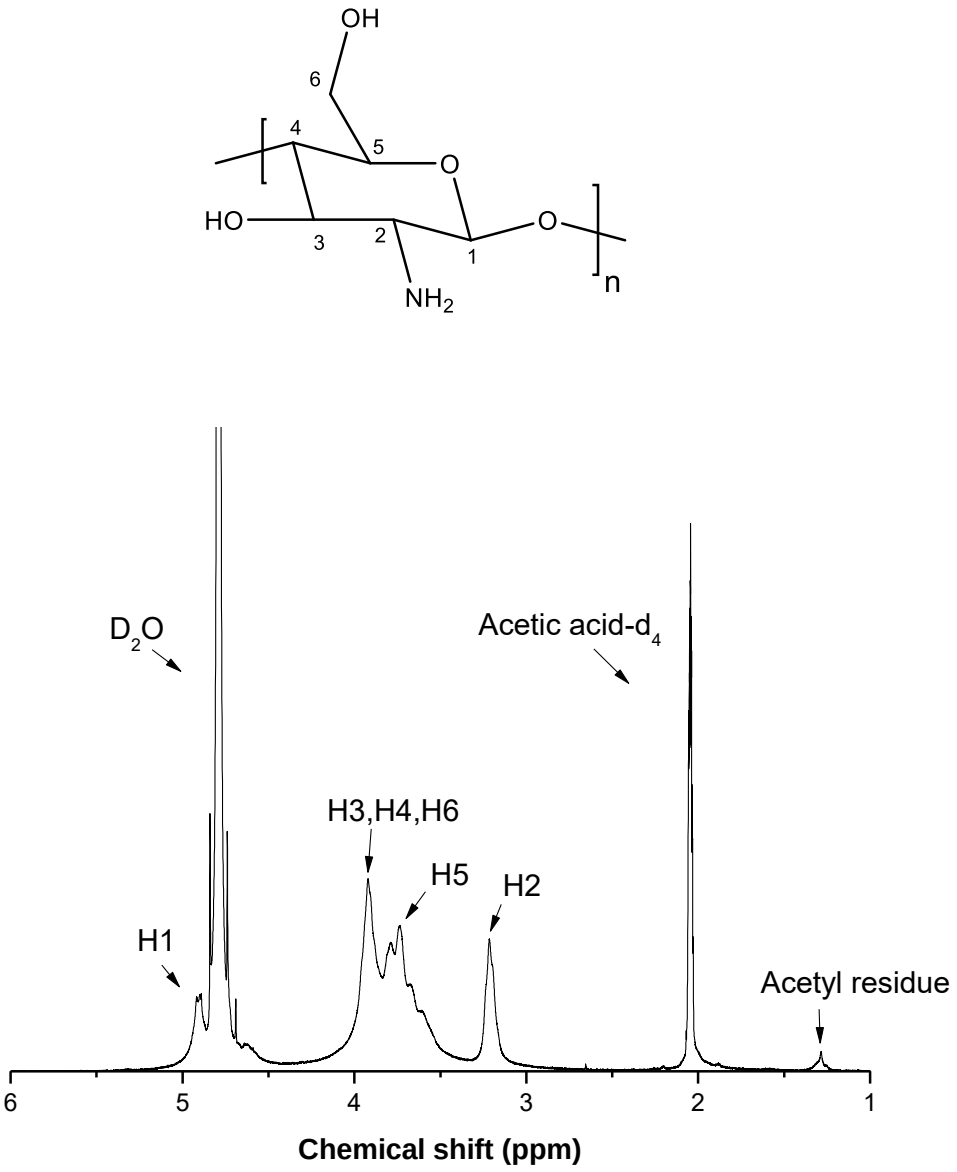

Figure 4.3.1-1: ^{1}H NMR spectrum of unmodified chitosan dissolved in D_2O/acetic acid-d_4 (70:30, v/v) at 60°C.

The DDA was calculated by using Equation 4.3-1, where H_2 is the methine proton on the C2 carbon and H_{Ac} is the acetyl residue signal.

$$\text{DDA } \% = \frac{H_2}{H_2 + \frac{H_{Ac}}{3}} \times 100 \qquad \text{Equation 4.3-1}$$

It was found that the DDA was 97% and, therefore, within specifications of the stated DDA of >75%.

The unmodified chitosan structure was characterised further by ^{13}C NMR and the spectrum is shown in Figure 4.3.1-2. The chemical shift at 98.22 ppm can be assigned to C1, 77.77 ppm to C4, 75.29 ppm to C5, 70.69 ppm to C3, 60.81 ppm to C6 and 56.41 ppm to C2. The peaks adjacent to or overlapping the solvent signals are assigned to methyl and carbonyl groups of the residual monomeric chitin.

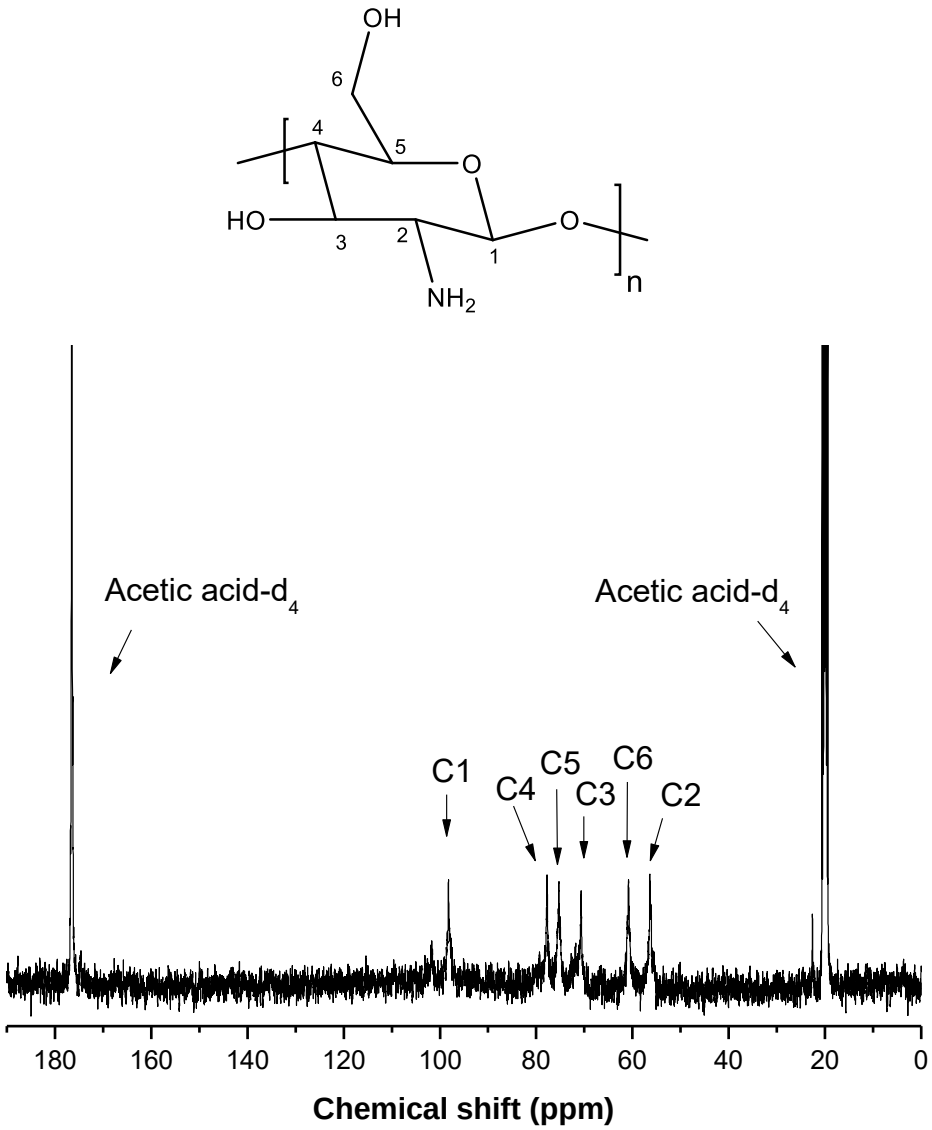

Figure 4.3.1-2: ^{13}C NMR spectrum of unmodified chitosan dissolved in D_2O/acetic acid-d_4 (70:30, v/v) at 60°C.

4.3.2 Quaternary chitosan (qC12)

a) 3-dimethylamino-2,2-dimethylpropanal

The NMR results of the intermediate aldehyde product are shown below. The notation below corresponds to the labelled carbon atoms in Figure 4.3.2-1. The ^{1}H NMR (600 MHz, D_2O) peaks (ppm) can be assigned as follow: 8.38 (1H, H1), 3.33 (2H, H3), 2.81 (6H, H4 & H5), 1.19 (6H, H6 & H7). The ^{13}C NMR (600 MHz, D_2O) peaks (ppm) can be assigned as follow: 170.59 (C1), 68.67 (C3), 45.58 (C4, C5), 42.46 (C2), 24.63 (C6, C7).

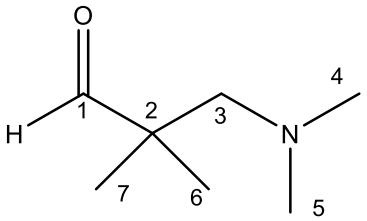

Figure 4.3.2-1: Chemical structure of 3-dimethylamino-2,2-dimethylpropanal with numbered carbon atoms.

b) *N*-substituted chitosan

Significant peaks (ppm) from the ^{1}H NMR (600 MHz, D_2O/acetic acid-d_4 (70:30, v/v) are as follow: 4.61 (1H, H1), 3.63 (4H, H3, H4 & H6), 3.51 (1H, H5), 2.91 (1H, H2), 2.64 (-N(CH_3)$_2$), 0.98 (6H, H12 & H13). ^{13}C NMR (300 MHz, D_2O/acetic acid-d_4 (70:30, v/v) (ppm) 99.25 (C1), 78.27 (C4), 76.47 (C5), 71.71 (C3), 61.68 (C6), 57.49 (C2), 51.90 (C7), 46.70 (-N(CH_3)$_2$), 25.41 (C12, C13). Figure 4.3.2-2 shows the labelled structure of *N*-substituted chitosan.

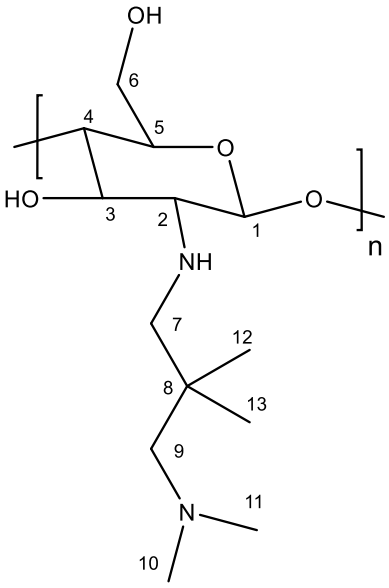

Figure 4.3.2-2: Chemical structure of *N*-substituted chitosan with numbered carbon atoms.

c) Quaternary chitosan derivative

The ^{1}H NMR spectrum of qC12 is shown in Figure 4.3.2-3. The peak at 4.50 ppm can be assigned to the methine H1 of the unmodified chitosan. The overlapping peaks in the chemical shift range 3.52-3.22 ppm can be assigned to H10, H6, H5, H4 and H3. Two methyl carbons are attached to the quaternary amine. The protons of the methyl carbons (H24 and H25) can be assigned to the peak at 2.92 ppm. The protons, H2 and H7, represent the peaks at 2.77 and 2.45 ppm, respectively. The protons of the two methyl carbons (H22 and H23) can be assigned to the peak at 1.87 ppm. The protons of H22-H25 and the signal peaks associated with the inner alkyl chain were used to confirm successful functionalisation. The peaks at 1.51 ppm represent the protons of the attached inner alkyl chain and 0.74 ppm represents the terminal methyl protons (H21). The acetyl residue from chitin, as with the unmodified chitosan, was still present in the ^{1}H NMR spectrum and can be assigned to the peak at 0.32 ppm.

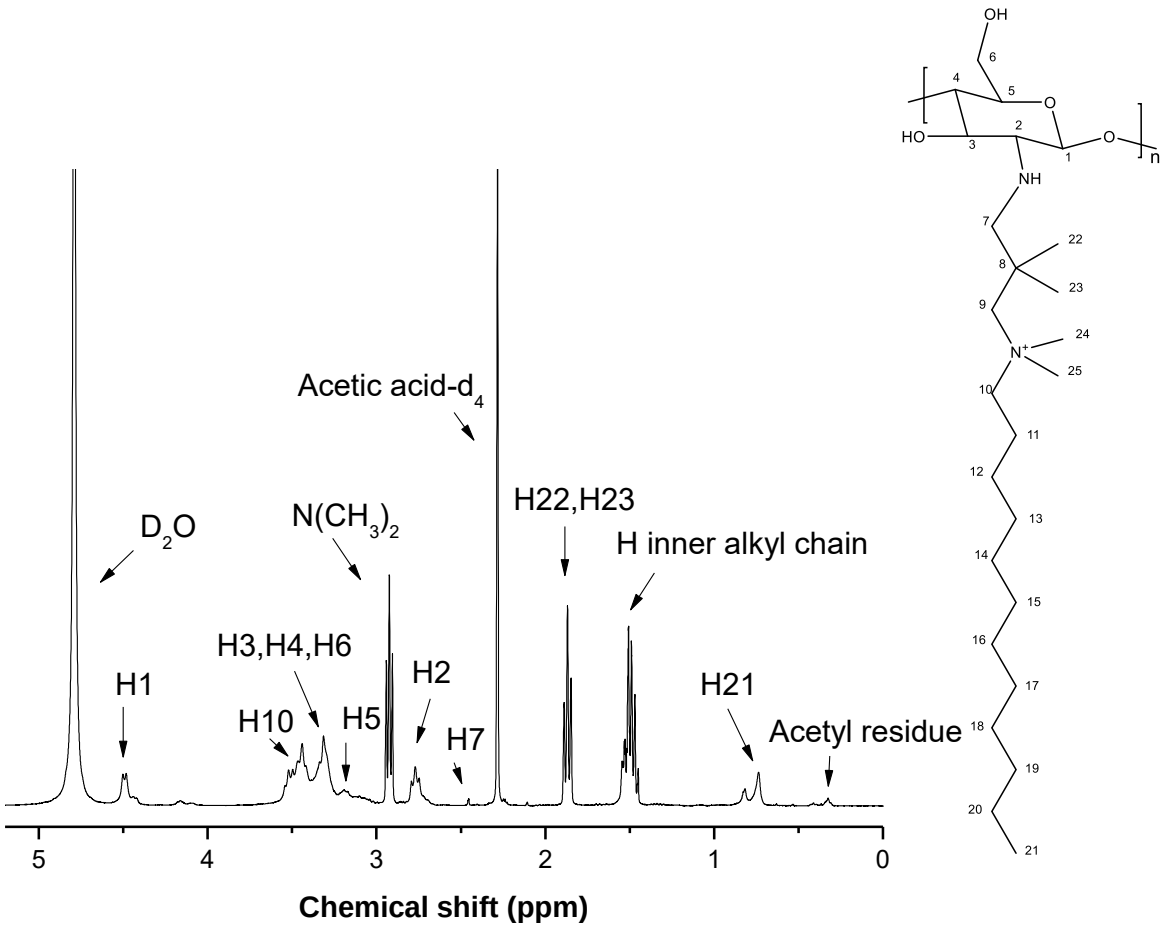

Figure 4.3.2-3: ^{1}H NMR spectrum of qC12 dissolved in D_2O/acetic acid-d_4 (70:30, v/v) at 60°C.

The degree of chitosan quaternisation (DQ %) was determined by analysing the ^{1}H NMR spectrum of CS-qC12. Equation 4.3-2 was used for this purpose, where H21 represents the

addition of the alkyl chains to the quaternary amine and H1 represents the chitosan backbone. The degree of quaternisation was calculated to be 87 % for the qC12 derivative.

$$DQ\ \% = \left[1 - \left(\frac{\left[\frac{H_{21}}{3}\right]}{H_1}\right)\right] \times 100 \qquad \text{Equation 4.3-2}$$

The ^{13}C NMR spectrum of qC12 is shown in Figure 4.3.2-4. The unmodified chitosan backbone was identified, similarly to Figure 4.3.1-2, and described by C1 to C6. The additional upfield signals describe the quaternisation. The methyl carbons (C24 and C25) of the quaternary amine can be assigned to 53.35 ppm and the methyl carbons (C22 and C23) to 33.83 ppm. The peaks at 32.53 ppm represent the methylene carbons of the attached alkyl chain but the terminal methyl carbon (C21) is represented by the peak at 20.35 ppm.

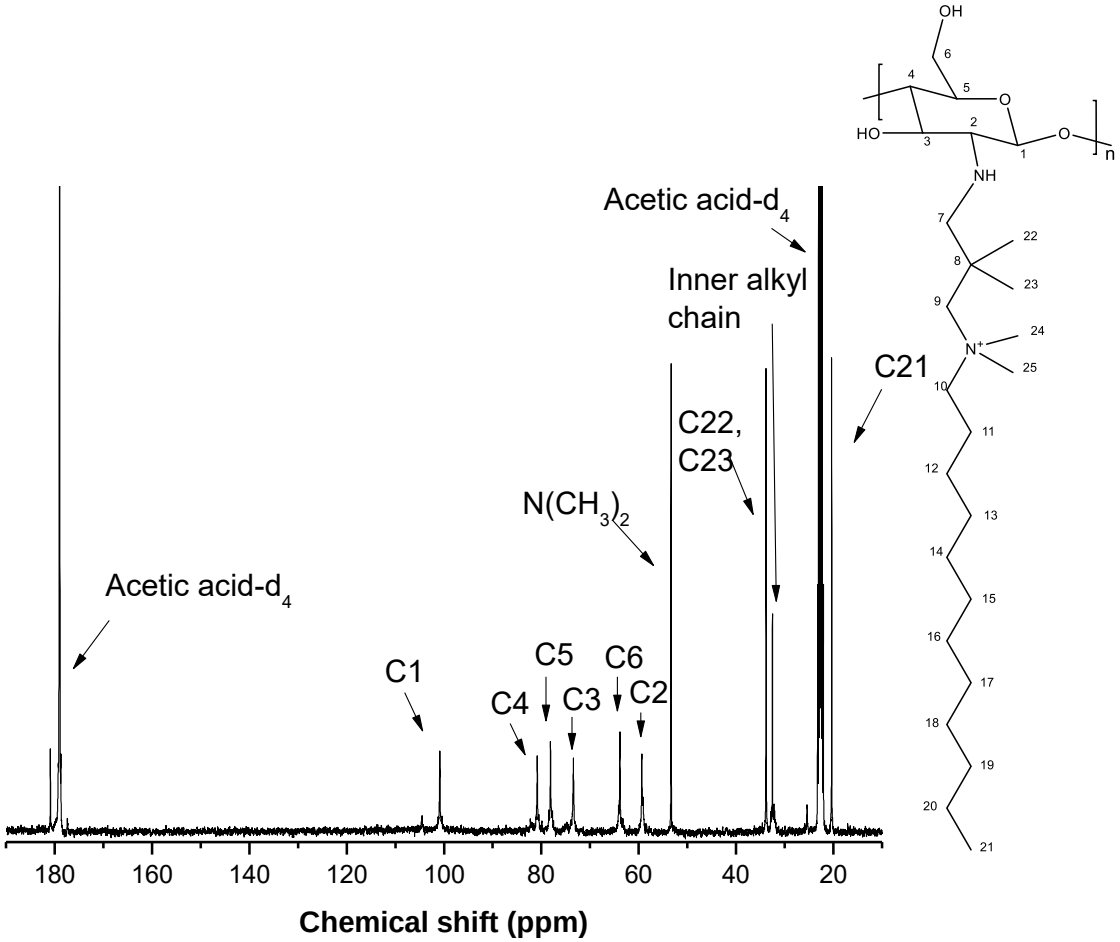

Figure 4.3.2-4: ^{13}C NMR spectrum of qC12 dissolved in D_2O/acetic acid-d_4 (70:30, v/v) at 60°C.

4.3.3 N,O-carboxymethyl chitosan (N,O-CMC)

The functionalisation of chitosan to *N,O*-CMC was investigated using both ^{1}H NMR and ^{13}C NMR. The ^{1}H NMR spectrum of this functionalised chitosan is shown in Figure 4.3.3-1. The peaks at 4.7 and 4.6 ppm can be assigned to the protons of C7 and C9, respectively. These peaks indicate the successful functionalisation to *N,O*-CMC[8]. The presence of the protons at

4.7 ppm confirms *O*-carboxymethylation, while *N*-carboxymethylation is confirmed by the peak at 4.6 ppm. Therefore, the ^{1}H NMR spectrum confirms that *N,O*-carboxymethylation occurred. The presence of peaks H1 to H6 represents the chitosan backbone, as illustrated in Figure 4.3.1-1.

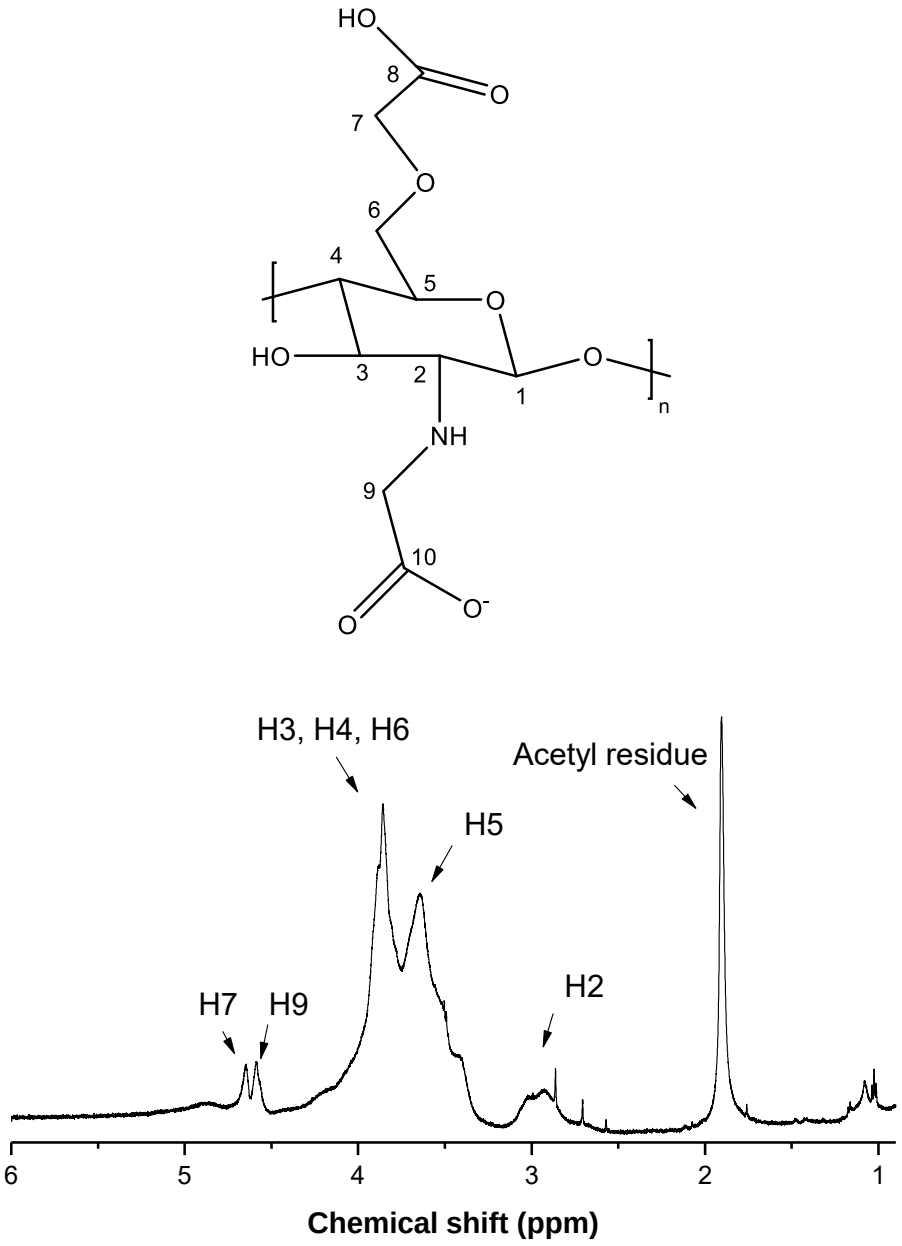

Figure 4.3.3-1: ^{1}H NMR spectrum of *N,O*-carboxymethyl chitosan dissolved in D_2O.

The ^{13}C NMR spectrum of *N,O*-CMC, shown in Figure 4.3.3-2, was obtained to confirm the ATR-FTIR and ^{1}H NMR results. The chemical shifts at 179.9 and 178.5 ppm can be assigned to C10 and C8, respectively. These peaks are associated with the carbonyl carbons of carboxymethyl groups and indicate successful synthesis of *N,O*-CMC[7,11,12]. The peaks assigned to C1 to C6 belong to the unmodified chitosan structure, as discussed in Chapter 4.3.1. The

peak at 56.6 ppm can be assigned to C7, which was identified as the methylene carbon of the carboxymethyl group indicated in Figure 4.3.3-2.

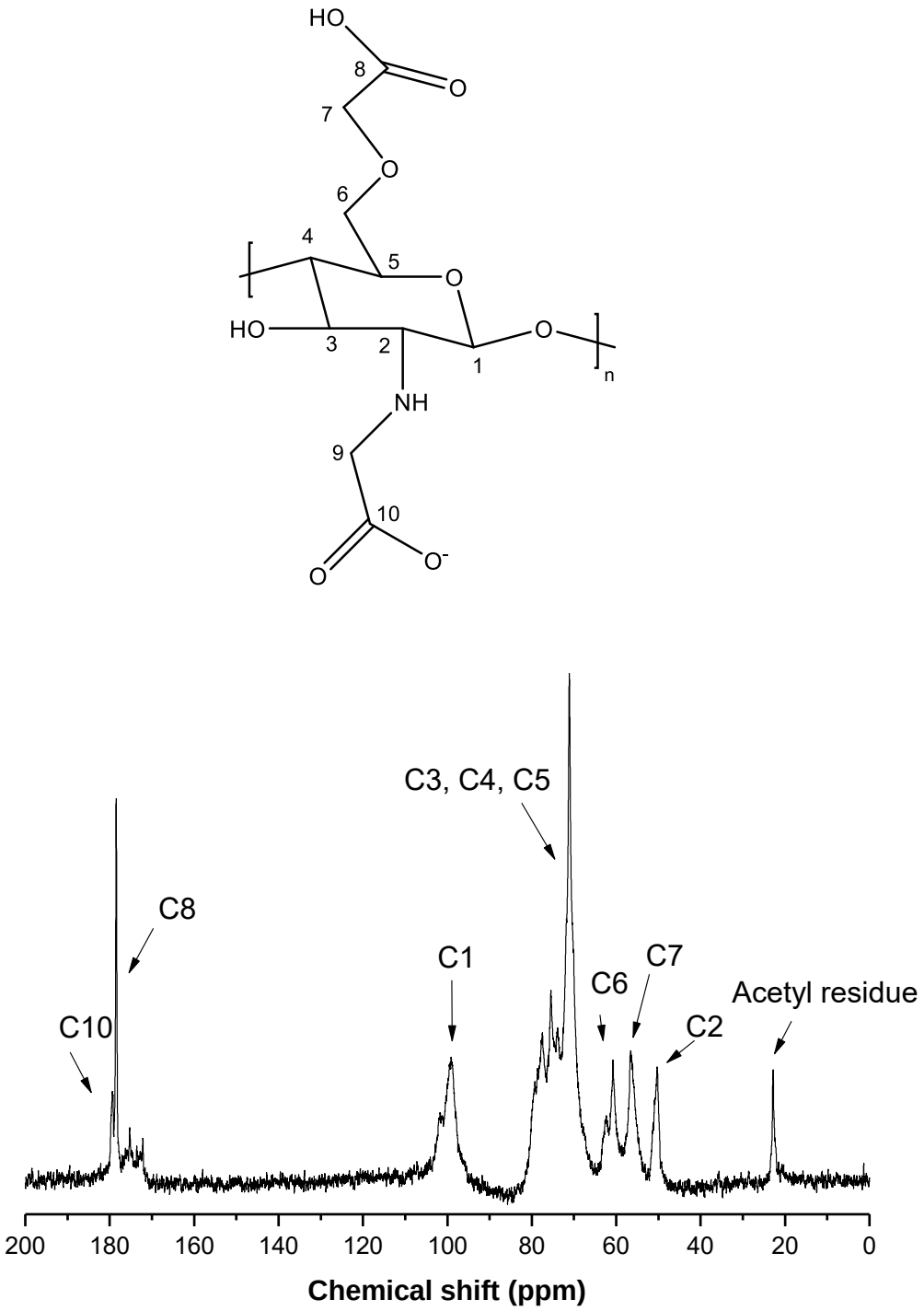

Figure 4.3.3-2: ^{13}C NMR spectrum of *N,O*-carboxymethyl chitosan in dissolved in D_2O.

4.4 Thermogravimetric analysis (TGA)

4.4.1 Unmodified chitosan nanoparticles

The thermal degradation data of unmodified chitosan and CNP is presented in Figure 4.4.1-1. This thermogram shows that the peak degradation temperature of the unmodified chitosan was 303°C, while CNP had a peak degradation temperature of 245°C. The weight loss at temperatures below 100°C was attributed to evaporation of the moisture content and resulted in a weight loss of 20.70% for unmodified chitosan and 15.47% for CNP[2,13,14]. The residue weight for unmodified chitosan was 8.17% and 32.51% for CNP. The peak degradation temperature of CNP was lower than that of unmodified chitosan but the increased residue weight of CNP indicated improved thermal stability after crosslinking. This can be attributed by the presence of inorganic phosphorous in the crosslinking material[15].

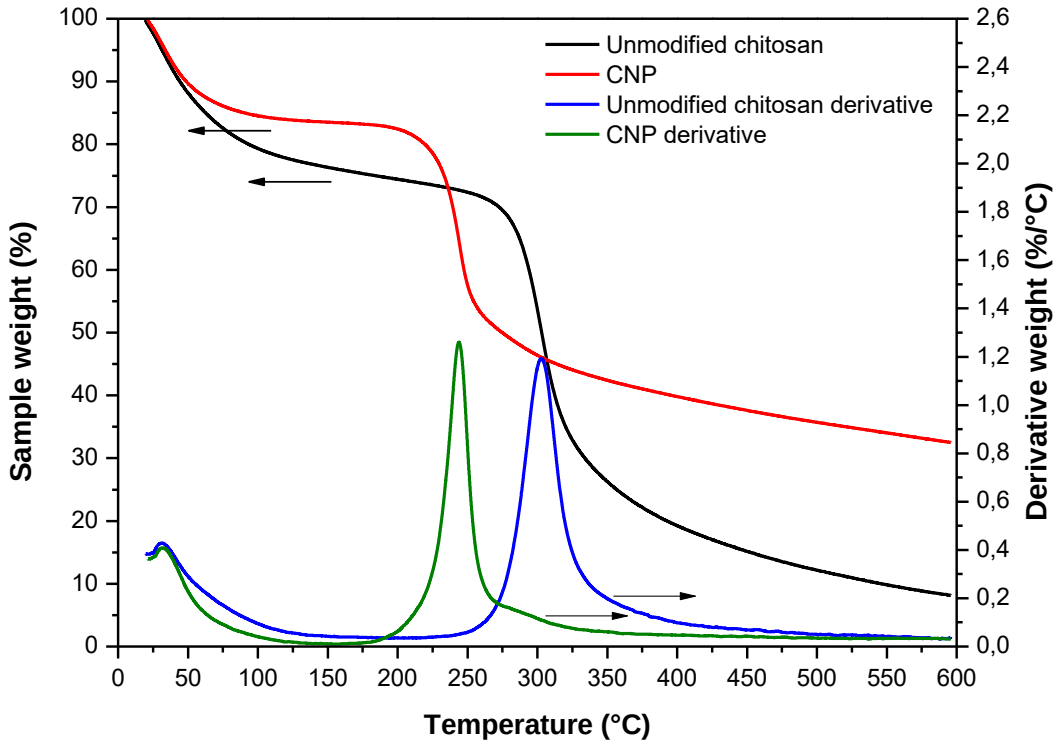

Figure 4.4.1-1: Thermal response data of unmodified chitosan and its produced nanoparticles.

4.4.2 Quaternary chitosan (qC12) nanoparticles

Figure 4.4.2-1 shows the thermal degradation of the functionalised quaternary chitosan derivative and the produced nanoparticles thereof. The quaternary chitosan experienced a primary degradation phase at 233°C while the nanoparticles underwent primary degradation at 244°C. The weight loss below 100°C was 16.51% for qC12 and 13.71% for qC12np. The residue weight after analysis was 27.66% and 42.11% for qC12 and qC12np, respectively. This indicates that the crosslinking of the quaternary chitosan with TPP increased the thermal

stability of the chitosan derivative. The main degradation temperature of qC12 was lower than that of unmodified chitosan. This decrease in thermal stability could be caused by the addition of bulky substituents on the chitosan amino groups and the decrease in interpolymer interactions[16].

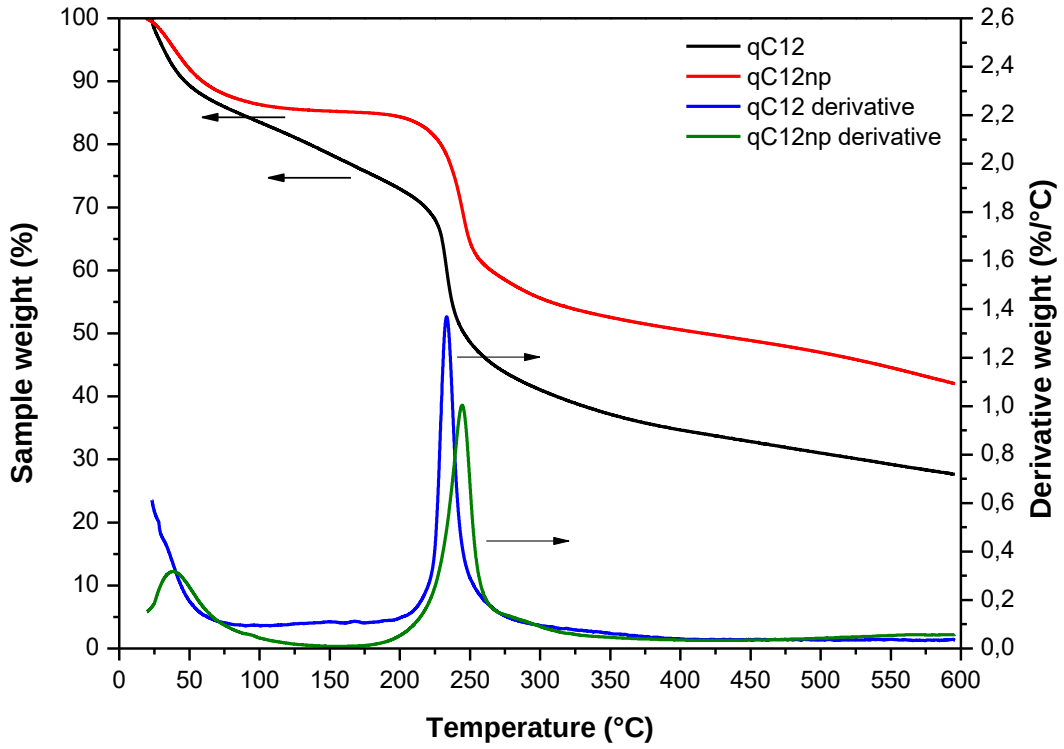

Figure 4.4.2-1: Thermal response data of quaternary chitosan and its produced nanoparticles.

4.4.3 N,O-carboxymethyl chitosan (N,O-CMC) particles

Figure 4.4.3-1 shows the thermal degradation data of the hydrophilic chitosan derivative, *N,O*-carboxymethyl chitosan, and its produced nanoparticles. The main degradation temperatures, of *N,O*-CMC and *N,O*-CMCnp, were measured at 279 and 263°C, respectively. The thermal degradation of the nanoparticles occurred over a wider temperature range, relative to *N,O*-CMC. The weight loss below 100°C, which was attributed to moisture loss, was 13.72% and 13.35% for *N,O*-CMC and *N,O*-CMCnp, respectively. The residue weight after analysis at 600°C was 32.70% for *N,O*-CMC and 27.45% for *N,O*-CMCnp. The results indicate that functionalisation of chitosan and crosslinking with TPP causes changes in the thermal stability of the final materials[2,15,16].

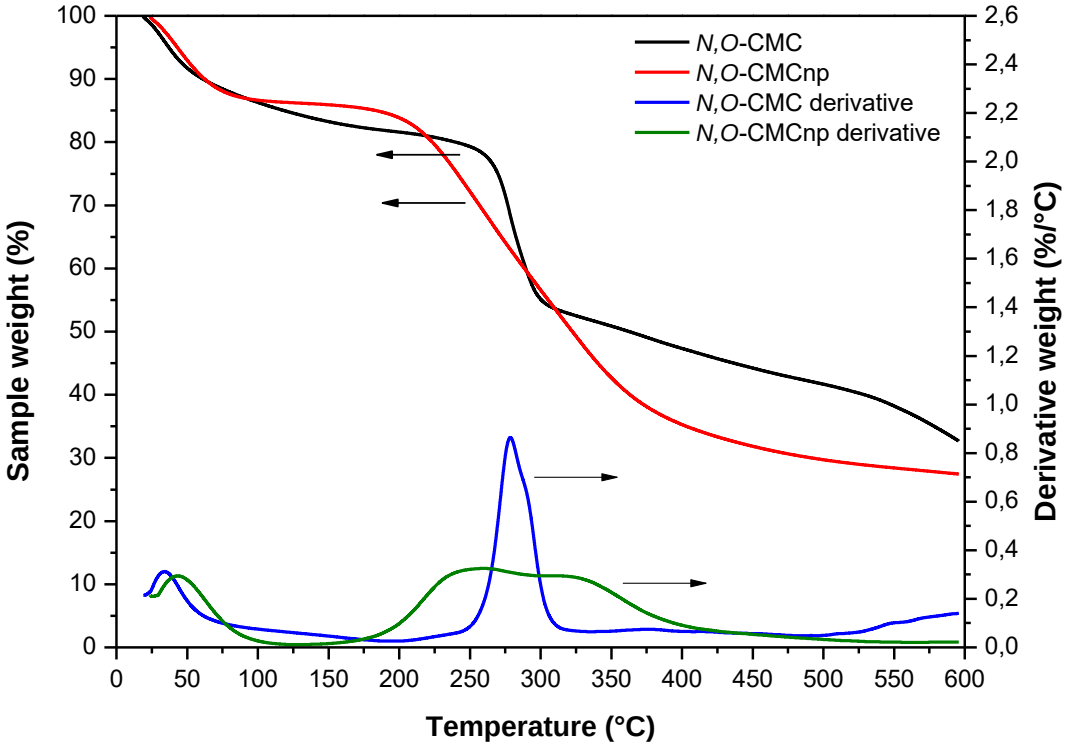

Figure 4.4.3-1: Thermal response data of *N,O*-carboxymethyl chitosan and its produced nanoparticles.

4.5 Scanning electron microscopy (SEM) analysis

The successful production of nanoparticles was confirmed by way of SEM analysis. Three variations of nanoparticles were successfully produced by using unmodified chitosan, quaternary chitosan and N,O-carboxymethyl chitosan. The nanoparticle dimensions are summarised in Table 4.5-1 and Figure 4.5-1. The differences in particle sizes could be attributed to the variations in polymer to TPP weight ratios. The weight ratios were based on the total weight of the unmodified and functionalised chitosan derivatives, instead of only considering the polymer weight of the original chitosan backbone. Therefore, the number of crosslinking sites varied between the unmodified and the functionalised chitosan. The individual nanoparticle size distributions are discussed in more detail below.

Table 4.5-1: Tabulated average nanoparticle diameters of the produced nanoparticles

	Count	Average (nm)	Standard deviation (nm)
Unmodified chitosan (CNP)	200	86	58
qC12np	200	44	8
***N,O*-CMCnp**	200	126	44

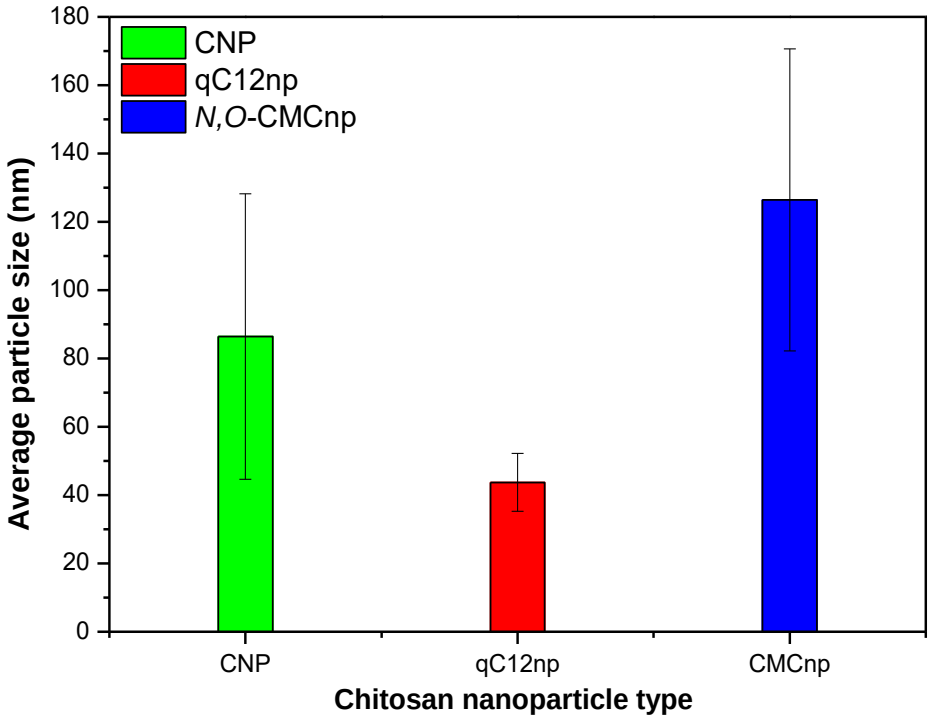

Figure 4.5-1: Average nanoparticle diameters (nm) of the produced nanoparticles.

4.5.1 Unmodified chitosan nanoparticles

The nanoparticle size distribution in Figure 4.5.1-1 shows that the majority of the counted nanoparticles were in the diameter size range of 45-95 nm. This was confirmed by the calculated average value of 86 ± 58 nm.

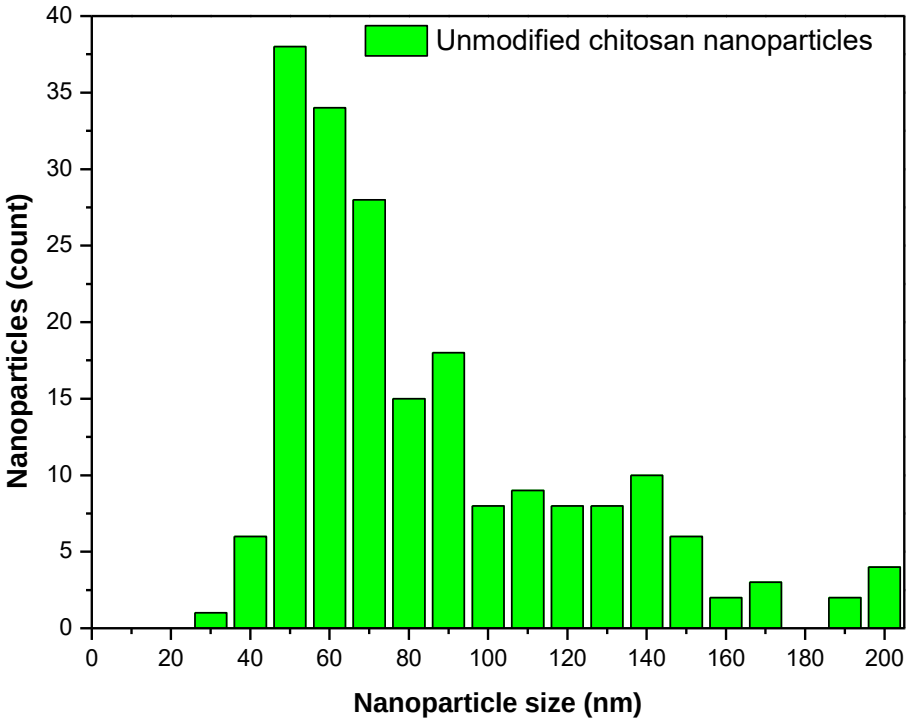

Figure 4.5.1-1: Particle size distribution of unmodified chitosan:TPP nanoparticles (2:1 w/w).

The SEM image in Figure 4.5.1-2 illustrates the size distribution of the produced CNPs.

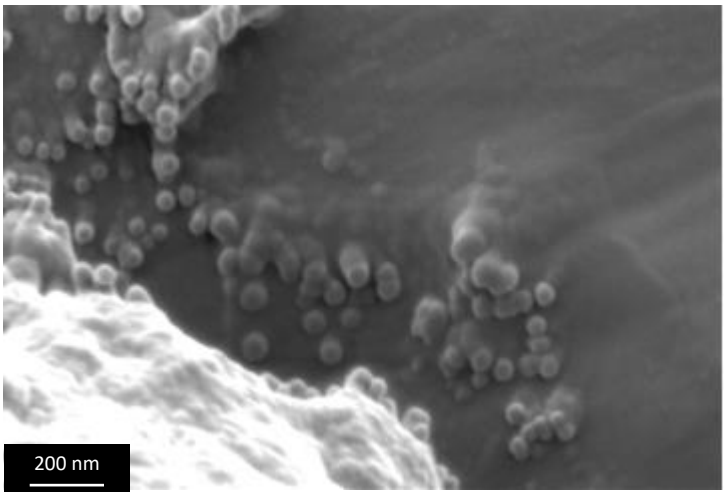

Figure 4.5.1-2: SEM image of unmodified chitosan:TPP nanoparticles (2:1 w/w).

4.5.2 Quaternary chitosan (qC12) nanoparticles

Figure 4.5.2-1 indicates that more than 70% of the produced nanoparticles have a diameter in the 35-55 nm range. This confirms the calculated average diameter of 44 ± 8 nm.

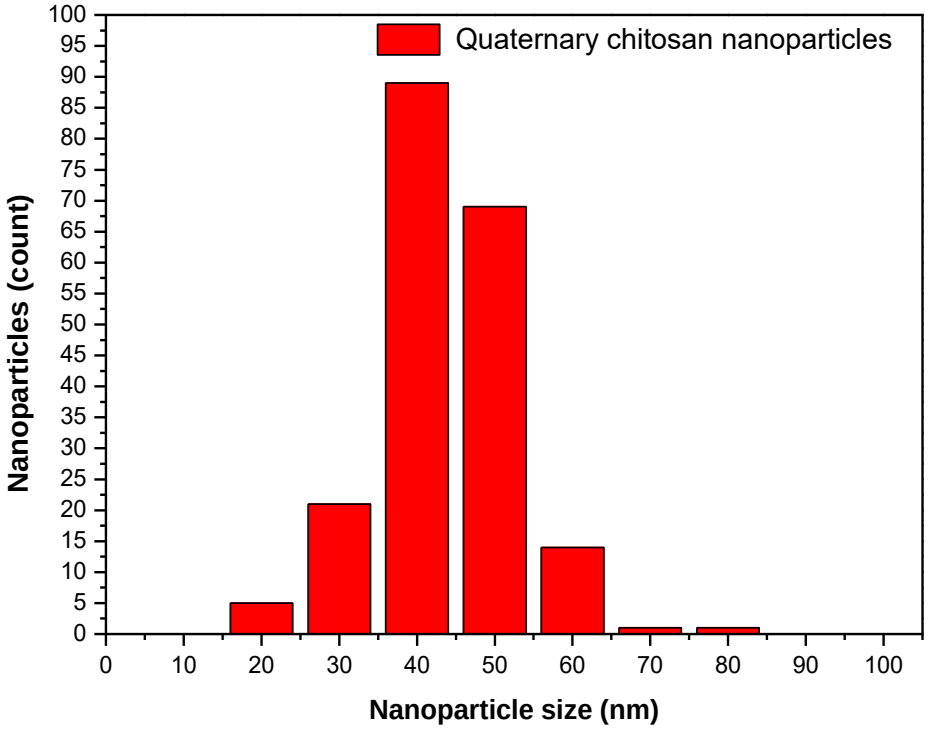

Figure 4.5.2-1: Particle size distribution of qC12:TPP nanoparticles (2:1 w/w).

The uniform size distribution is illustrated in Figure 4.5.2-2. The average particle size was 42 nm smaller compared to the unmodified chitosan nanoparticles. The size reduction of qC12np, relative to CNP, might have been due to the addition of a hydrophobic substituent onto the amino group of chitosan which could have disturbed some of the intermolecular hydrogen bonding of the polymer[17].

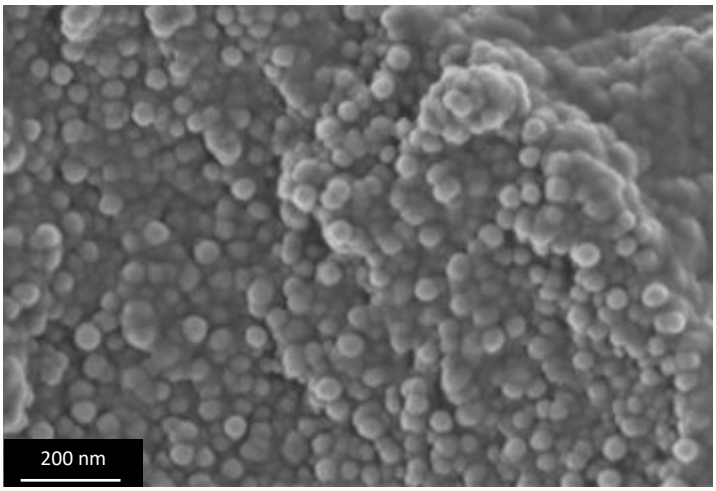

Figure 4.5.2-2: SEM image of qC12:TPP nanoparticles (2:1 w/w).

4.5.3 N,O-carboxymethyl chitosan (N,O-CMC) nanoparticles

Figure 4.5.3-1 shows that the *N,O*-CMC nanoparticles were produced in a wide range of sizes. There was no dominant size range and the average was calculated to be 126 ± 44 nm.

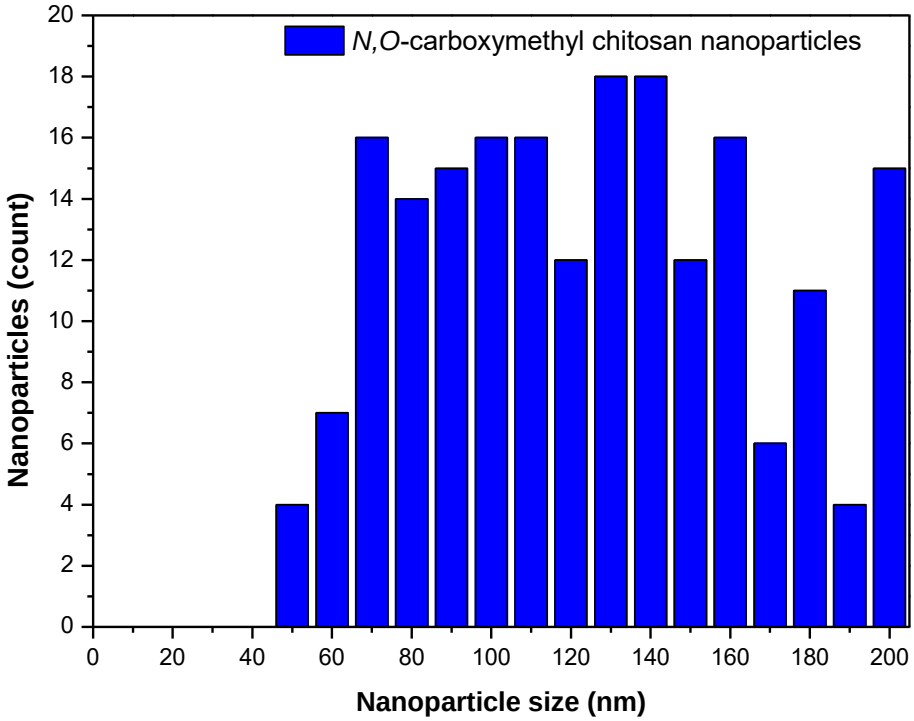

Figure 4.5.3-1: Particle size distribution of *N,O*-CMC:TPP nanoparticles (5:1 w/w).

Figure 4.5.3-2 confirms the lack of uniform particle sizes. The *N,O*-CMC functionalisation and nanoparticle production was performed using previously established methods[18–20]. Based on these methods, acetic acid was not needed to protonate the *N,O*-CMC to crosslink with TPP. When the nanoparticle production was initially attempted, without using an acetic acid solution, there was no crosslinking taking place. Upon addition of acetic acid to the *N,O*-CMC:TPP solution, crosslinking instantly occurred. Therefore, a critical acetic acid concentration had to be determined experimentally to promote crosslinking[21].

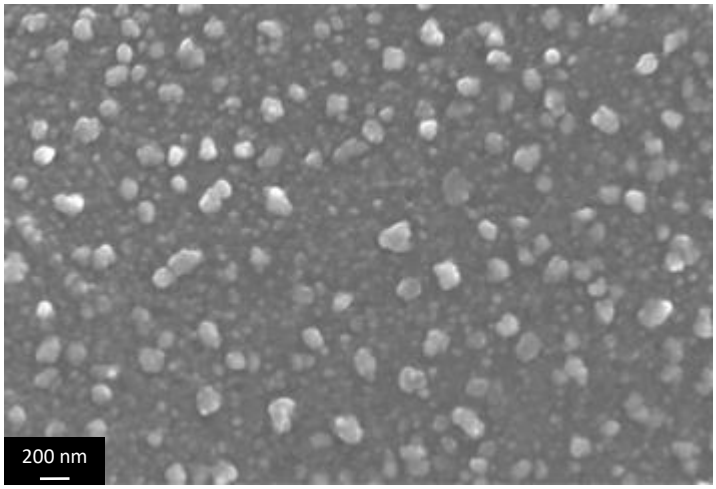

Figure 4.5.3-2: SEM image of *N,O*-CMC:TPP nanoparticles (5:1 w/w).

Exceeding the critical acetic acid concentration led to the *N,O*-CMC precipitating out of solution. As a result, the final nanoparticle diameter was significantly influenced by the acetic acid concentration and was responsible for the lack of a monodispersed particle size. Table 4.5.3-1 illustrates the acetic acid solution concentrations which were tested to protonate *N,O*-CMC before crosslinking with TPP.

Table 4.5.3-1: Acetic acid solution concentrations for the protonation of *N,O*-CMC

Acetic acid solution concentration (w/v)	**Nanoparticle production**
0.35%	Insufficient crosslinking
0.50%	Insufficient crosslinking
0.75%	Crosslinking
0.90%	Precipitation

4.6 Fluorescence spectroscopy

Fluorescence spectroscopy was performed on fluorescein 5(6)-isothiocyanate (FITC) to confirm its excitation and emission characteristics. Figure 4.6-1 shows that FITC has an excitation maximum at 491 nm and an emission peak at 520 nm[22].

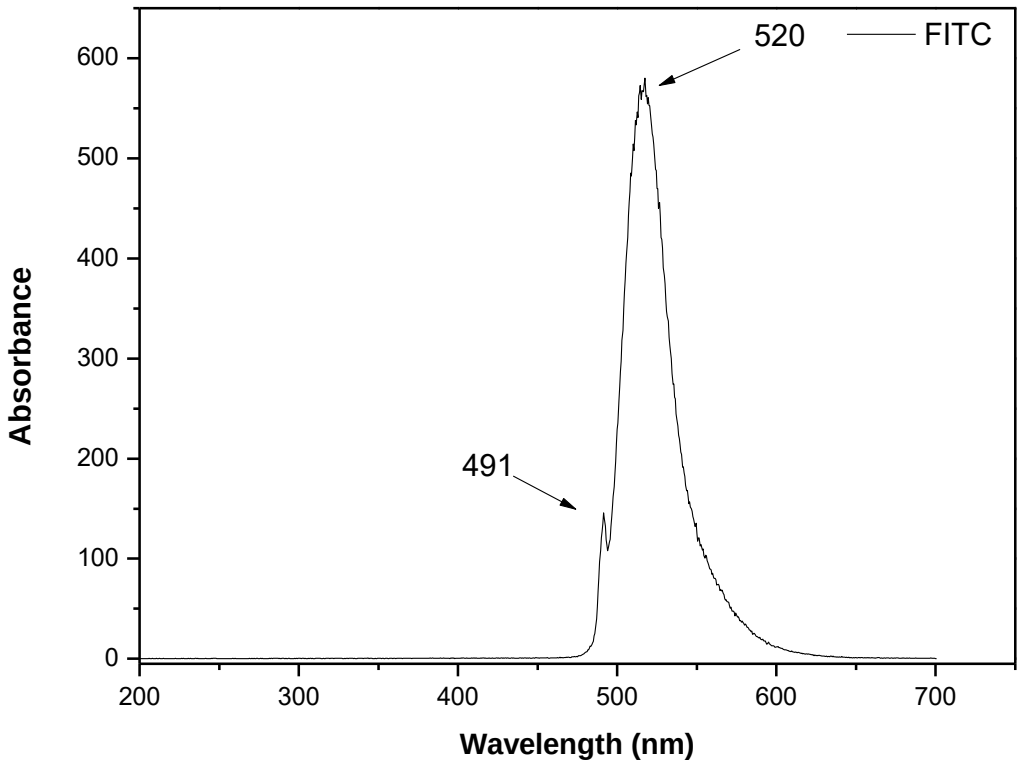

Figure 4.6-1: Fluorescence spectrum of FITC in distilled water.

The FITC dye was attached to all three types of produced chitosan nanoparticles, as discussed in Chapter 3. The FITC labelled nanoparticles were subjected to fluorescence spectroscopy to confirm successful attachment of FITC to the nanoparticles and the results are shown in Table 4.6-1.

Table 4.6-1: Fluorescence spectroscopy results of FITC labelled nanoparticles

Sample	Excitation (nm)	Emission (nm)
FITC/CNP	491	531
FITC/qC12np	491	529
FITC/*N,O*-CMCnp	491	513

4.7 Conclusions

The results obtained from FTIR and NMR showed successful functionalisation of the unmodified chitosan to both its hydrophobic and hydrophilic derivatives. Furthermore, SEM analysis illustrated the successful production of nanoparticles from chitosan and its derivatives.

The particle size of the *N,O*-CMCnp was the largest of the three different types of nanoparticles. SEM analysis showed a variation in particle sizes and this was attributed to the production method used and the chemical structures of the chitosan derivatives. The particle size was partly dependent on the amount of acetic acid used to protonate the chitosan backbone and on the method used to separate the nanoparticles from solution after crosslinking. The separation of the hydrophilic *N,O*-CMCnp from water (through centrifugation) proved to be challenging. This was attributed to strong hydrogen bonding between water and the hydrophilic nanoparticles. As a result, the separated nanoparticles were of a larger size range while some of the smaller particles could not be removed from solution.

The produced nanoparticles were successfully fluorescently labelled so that they could be detected within polymer matrices. The distribution of the nanoparticles in different matrices was investigated further in subsequent chapters.

4.8 References

1. Xu, Y. & Du, Y. Effect of molecular structure of chitosan on protein deli v ery properties of chitosan nanoparticles. *Int. J. Pharm.* **250**, 215–226 (2003).

2. Thandapani, G., Supriya Prasad, P., Sudha, P. N. & Sukumaran, A. Size optimization and in vitro biocompatibility studies of chitosan nanoparticles. *Int. J. Biol. Macromol.* **104**, 1794–1806 (2017).

3. Smit, M. Polymer-coated magnetic nanoparticles and modified polymer nanofibers for the efficient capture of Mycobacterium tuberculosis (Mtb) (MSc). (Stellenbosch University, 2018).

4. Guo, Z., Liu, H., Chen, X., Ji, X. & Li, P. Hydroxyl radicals scavenging activity of N-substituted chitosan and quaternized chitosan. *Bioorganic Med. Chem. Lett.* **16**, 6348–6350 (2006).

5. Guo, Z., Xing, R., Liu, S., Zhong, Z., Ji, X., Wang, L. & Li, P. Antifungal properties of Schiff bases of chitosan, N-substituted chitosan and quaternized chitosan. *Carbohydr. Res.* **342**, 1329–1332 (2007).

6. Robert M. Silverstein, Francis X. Webster, D. J. K. *Spectrometric identification of organic*

compounds. *Journal of Molecular Structure* (2005).

7. Lin, C. C. & Lin, C. W. Preparation of N,O-carboxymethyl chitosan nanoparticles as an insulin carrier. *Drug Deliv.* **16**, 458–464 (2009).

8. Chen, S. C., Wu, Y. C., Mi, F. L., Lin, Y. H., Yu, L. C. & Sung, H. W. A novel pH-sensitive hydrogel composed of N,O-carboxymethyl chitosan and alginate cross-linked by genipin for protein drug delivery. *J. Control. Release* **96**, 285–300 (2004).

9. Anitha, A., Divya Rani, V. V., Krishna, R., Sreeja, V., Selvamurugan, N., Nair, S. V., Tamura, H. & Jayakumar, R. Synthesis, characterization, cytotoxicity and antibacterial studies of chitosan, O-carboxymethyl and N,O-carboxymethyl chitosan nanoparticles. *Carbohydr. Polym.* **78**, 672–677 (2009).

10. Abdel-Rahman, R. M., Hrdina, R., Abdel-Mohsen, A. M., Fouda, M. M. G., Soliman, A. Y., Mohamed, F. K., Mohsin, K. & Pinto, T. D. Chitin and chitosan from Brazilian Atlantic Coast: Isolation, characterization and antibacterial activity. *Int. J. Biol. Macromol.* **80**, 107–120 (2015).

11. Matsuhiro, B., Presle, L. C., Saenz, C. & Urzua, C. C. Structural determination and chemical modifications of the polysaccharide from seeds of Prosopis chilensis Mol. (Stuntz). *J. Chil. Chem. Soc.* **51**, 809–813 (2006).

12. Mourya, V. K., Inamdar, N. N. & Tiwari, A. Carboxymethyl chitosan and its applications. *Adv. Mater. Lett.* **1**, 11–33 (2010).

13. Zakaria, Z., Izzah, Z., Jawaid, M. & Hassan, A. Effect of degree of deacetylation of chitosan on thermal stability and compatibility of chitosan-polyamide blend. *BioResources* **7**, 5568–5580 (2012).

14. Kaya, M., Cakmak, Y. S., Baran, T., Asan-Ozusaglam, M., Mentes, A. & Tozak, K. O. New chitin, chitosan, and O-carboxymethyl chitosan sources from resting eggs of Daphnia longispina (Crustacea); with physicochemical characterization, and antimicrobial and antioxidant activities. *Biotechnol. Bioprocess Eng.* **19**, 58–69 (2014).

15. Ali, S. W., Rajendran, S. & Joshi, M. Synthesis and characterization of chitosan and silver loaded chitosan nanoparticles for bioactive polyester. *Carbohydr. Polym.* **83**, 438–446 (2011).

16. Bakshi, P. S., Selvakumar, D., Kadirvelu, K. & Kumar, N. S. Comparative study on antimicrobial activity and biocompatibility of N-selective chitosan derivatives. *React. Funct. Polym.* **124**, 149–155 (2018).

17. Jothimani, B., Sureshkumar, S. & Venkatachalapathy, B. Hydrophobic structural

modification of chitosan and its impact on nanoparticle synthesis – A physicochemical study. *Carbohydr. Polym.* **173**, 714–720 (2017).

18. Hayes, E. R. N,O-Carboxymethyl chitosan and preparative method thereof. (1986).

19. Kusuma, H. S., Al-sa'bani, A. F. & Darmokoesoemo, H. N,O-Carboxymethyl Chitosan: An Innovation in New Natural Preservative from Shrimp Shell Waste with a Nutritional Value and Health Orientation. *Procedia Food Sci.* **3**, 35–51 (2015).

20. Anitha, A., Maya, S., Deepa, N., Chennazhi, K. P., Nair, S. V. & Jayakumar, R. Curcumin-Loaded N,O-Carboxymethyl Chitosan Nanoparticles for Cancer Drug Delivery. *J. Biomater. Sci. Polym. Ed.* **23**, 1381–1400 (2012).

21. Fan, W., Yan, W., Xu, Z. & Ni, H. Formation mechanism of monodisperse, low molecular weight chitosan nanoparticles by ionic gelation technique. *Colloids Surfaces B Biointerfaces* **90**, 21–27 (2012).

22. Le Grange, M. The use of fluorescence to probe the morphology changes in complex polymers (MSc). (University Stellenbosch, 2015).

CHAPTER 5

RESULTS AND DISCUSSION – NANOCOMPOSITE FILMS

5.1 Introduction

In this chapter three kinds of chitosan nanoparticles were added to poly(vinyl alcohol-co-ethylene) (EVOH) and low-density polyethylene (LDPE) matrices to create nanocomposite films. These nanoparticles were unmodified chitosan nanoparticles (CNP), *N,O*-carboxymethyl chitosan nanoparticles (*N,O*-CMCnp) and quaternary ammonium chitosan nanoparticles (qC12np) at varying loadings. The EVOH matrices were denoted as EVOH27, EVOH38 and EVOH44, where the values of 27, 38 and 44 correspond to the ethylene content (mole %) in the EVOH copolymers.

The nanoparticle distribution within a specific matrix was investigated by scanning electron microscopy – energy dispersive X-ray spectrometer (SEM-EDS), ultraviolet-visible spectroscopy (UV/Vis) and confocal fluorescence microscopy (CFM). Thermal and physical film properties were analysed by differential scanning calorimetry (DSC), tensile testing, static contact angle (SCA) measurements and water uptake studies. Antimicrobial studies were also performed to determine whether the addition of the three kinds of nanoparticles provided the nanocomposite films with antimicrobial properties.

5.2 Scanning electron microscopy (SEM)

The SEM image, Figure 5.2-1, confirms the presence of CNP on the surface of the melt-pressed films. An EDS detector was used to obtain an elemental map of the nanocomposite film in order to gain a better insight of the nanoparticle distribution throughout the polymer films.

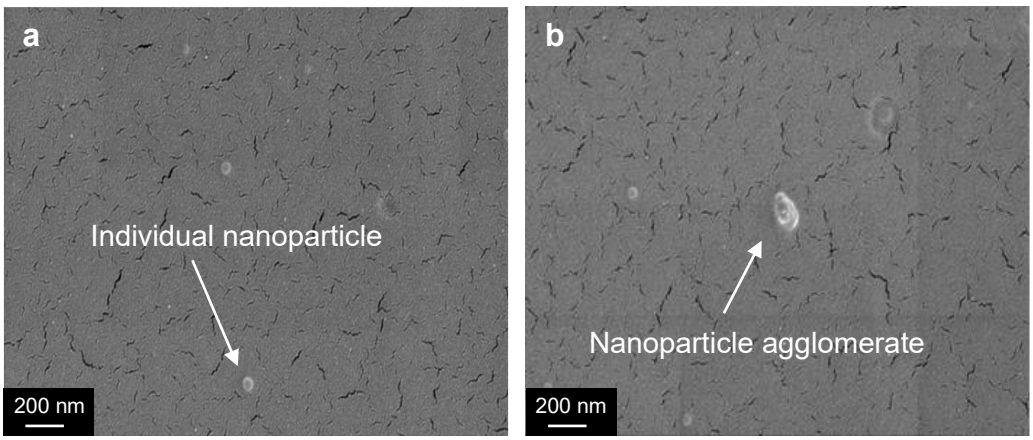

Figure 5.2-1: SEM images of the film surface of EVOH44 containing CNP (5 wt%). Individual nanoparticles (a) can be seen, along with (b) agglomerates.

Figure 5.2-2 shows SEM-EDS images of CNPs. The elemental analysis identified phosphorous, which was present in the TPP crosslinking agent, and nitrogen from the amine functionality of chitosan. These two elements were the only distinguishing factors between the elemental compositions of the nanoparticle fillers and the EVOH matrices. Identification of these elements in the nanocomposite materials would have provided an image of the nanoparticle distribution in the matrices, but unfortunately this analysis was unsuccessful.

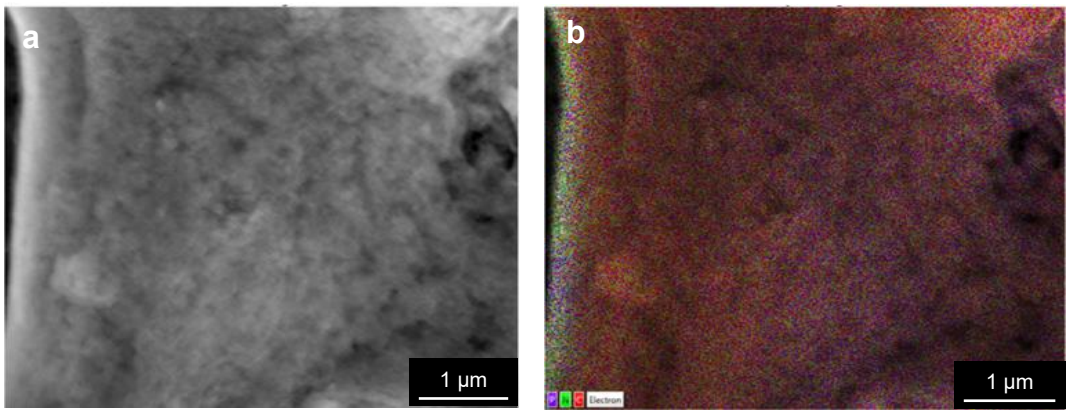

Figure 5.2-2: Electron image of (a) CNP alongside (b) an elemental map of the same sample.

The same sample shown in Figure 5.2-1 was subjected to SEM-EDS and the results are shown in Figure 5.2-3. Neither phosphorous nor nitrogen was detected in the nanocomposite film sample. This was attributed to non-optimal equipment settings. A stronger electron beam would have improved the sensitivity of the detector but the polymer matrix was destroyed at electron beam intensities above 5 kV. As a result, SEM-EDS could not provide additional data regarding the nanoparticle distribution throughout the nanocomposite films. Therefore, alternative analyses were discussed below.

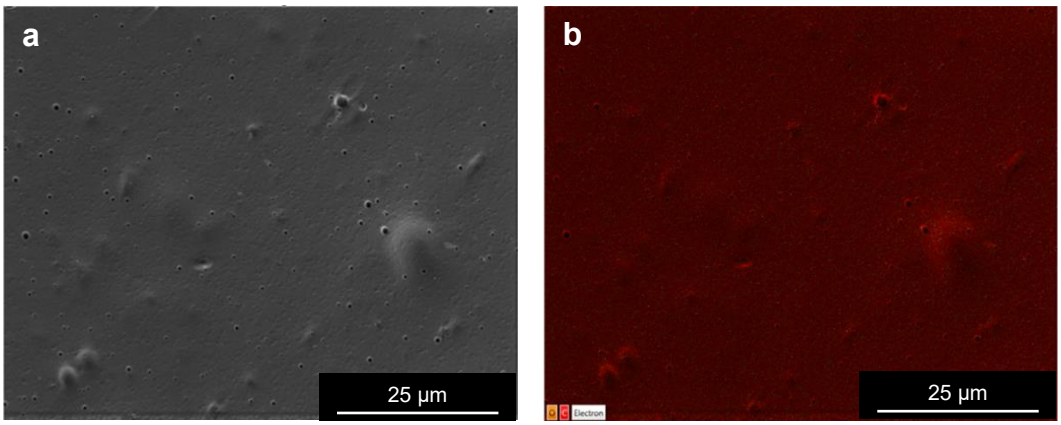

Figure 5.2-3: Electron image of (a) EVOH44 with 5 wt% filler content alongside (b) an elemental map of the same sample.

5.3 UV/Vis spectroscopy

The transparency of the nanocomposite films was compared in a lightbox. Samples were analysed under CIE Standard Illuminant D65 conditions[1]. The results are shown in Figure 5.3-1 and reveal a slight discoloration at filler content above 3 wt%. Instead of subjecting all nanocomposite films to visual inspection the nanocomposite films were analysed using UV/Vis to see whether a correlation could be seen between filler content and transparency.

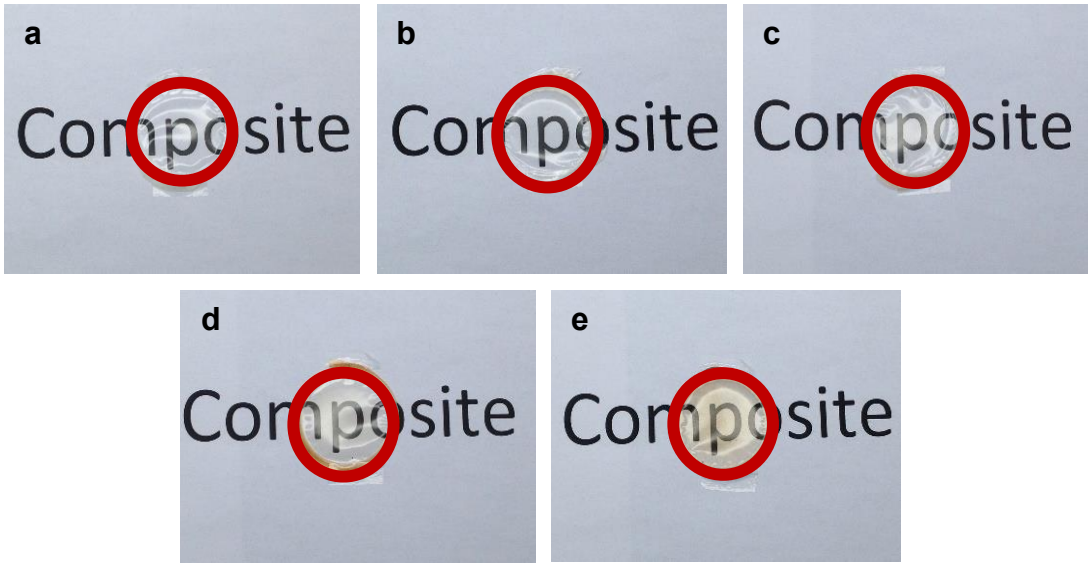

Figure 5.3-1: Transparency of EVOH27 nanocomposite films with (a) 0 wt%, (b) 1 wt%, (c) 3 wt%, (d) 5 wt% and (e) 8 wt% of CNP.

The films shown in Figure 5.3-1 were analysed using UV/Vis and the results are shown in Figure 5.3-2. The UV/Vis results confirmed that the film transparency decreased with an increase in filler content. This trend was visible, irrespective of the nanoparticle variant. Similar analyses were performed on the EVOH38, EVOH44 and LDPE matrices and can be seen in Figure A-1, Figure A-2 and Figure A-3 in Appendix A.

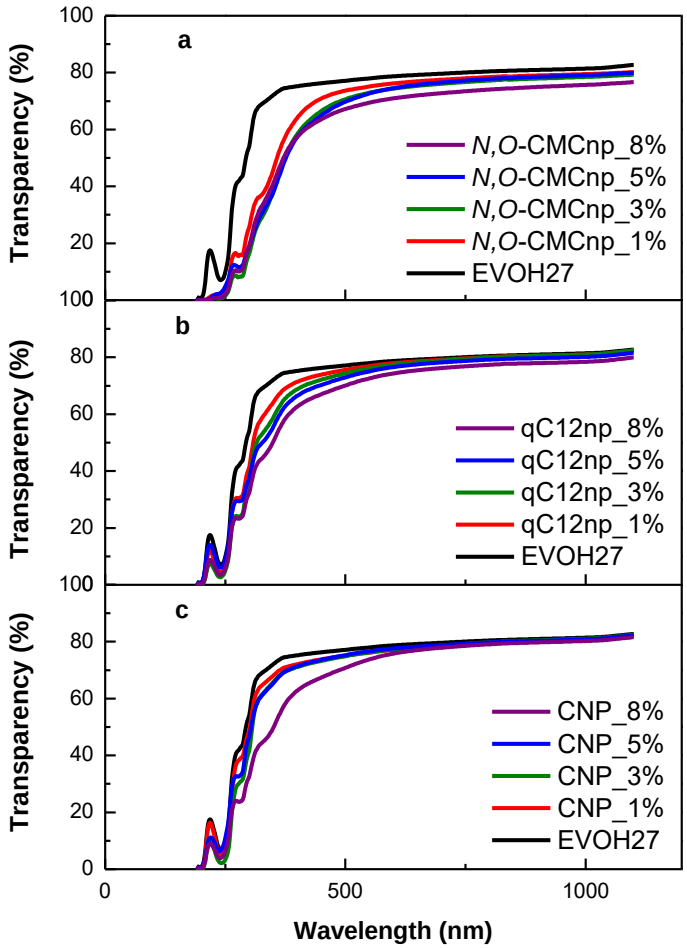

Figure 5.3-2: UV/Vis results of nanocomposite films using EVOH27 as matrix and (a) *N,O*-CMCnp, (b) qC12np and (c) CNP as nanofiller.

5.4 Confocal fluorescence microscopy (CFM)

In order to further investigate the nanofiller distribution, the produced nanoparticles were fluorescently labelled with FITC and subjected to confocal microscopy, as discussed in Chapter 3.3.7.

A CNP/FITC solution was prepared and submitted for CFM to illustrate the successful fluorescent labelling of the nanoparticles. Figure 5.4-1 (a) shows the resuspended CNP/FITC, using a TPMT filter. Figure 5.4-1 (b) shows the fluorescent signal of the labelled nanoparticles after excitation at 488 nm and Figure 5.4-1 (c) is an overlay of (a) and (b) to show that only the nanoparticles showed fluorescence.

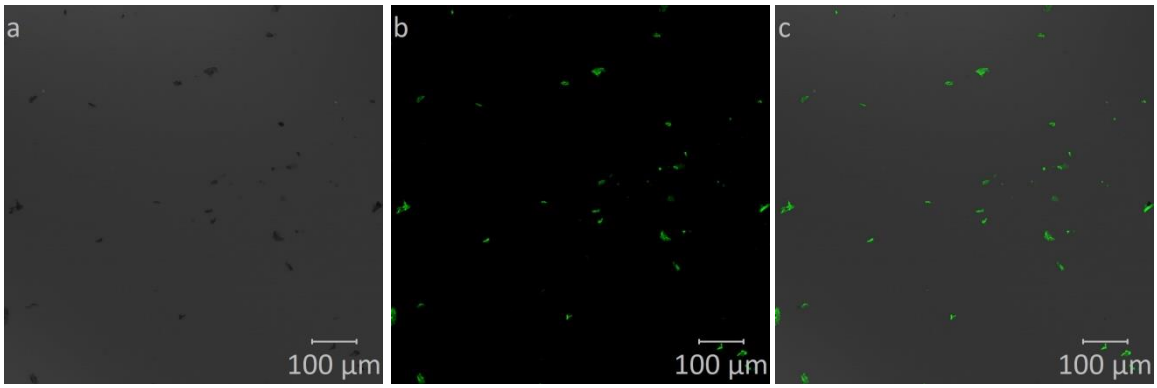

Figure 5.4-1: CFM image of resuspended CNP/FITC in water (a) using the TPMT filter, (b) at 488 nm excitation and (c) an overlay image.

The EVOH44 nanocomposite films, containing CNP, were analysed initially to determine the effect of filler content on its distribution throughout the matrix. Figure 5.4-2 shows the CNP distribution at (a) 1 wt%, (b) 3 wt%, (c) 5 wt% and (d) 8 wt% in EVOH44. According to the CFM images the CNP nanofillers were distributed evenly throughout the matrix, but some agglomeration of the nanoparticles could also be seen. The influence of different matrices and nanoparticle derivatives were investigated below by only considering 3 wt% filler content.

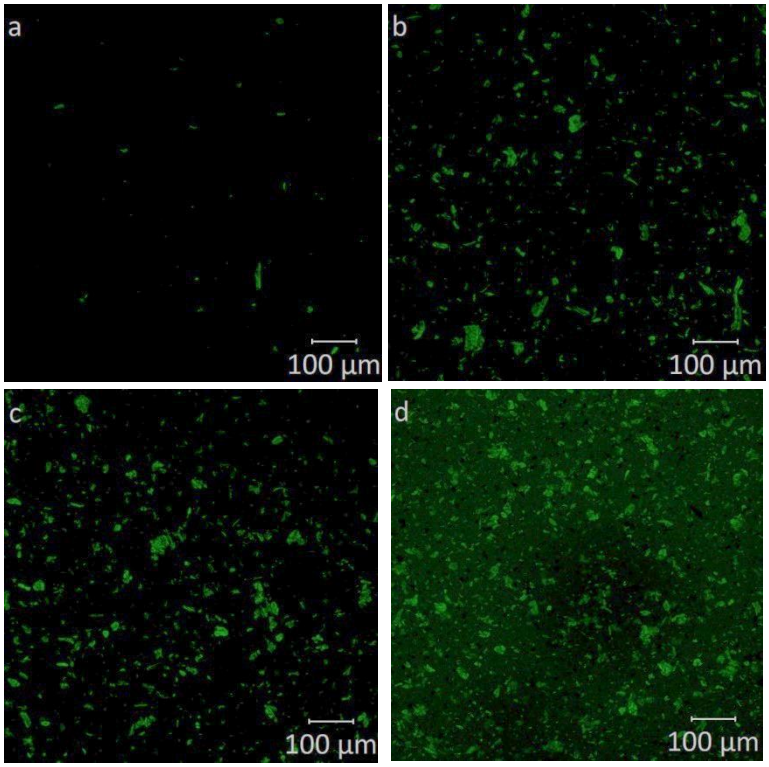

Figure 5.4-2: CFM images of EVOH44 nanocomposite films with CNP content of (a) 1 wt%, (b) 3 wt%, (c) 5 wt% and (d) 8 wt%.

Table 5.4-1 summarises the CFM analysis for the nanocomposite films. The distribution of the nanoparticles, within a specific matrix, seemed unaffected by the type of nanoparticles. During this investigation the type of matrix had a more significant impact.

Table 5.4-1: Summary of CFM results for nanocomposite films with 3 wt% loadings

	***N,O*-CMCnp**	**CNP**	**qC12np**
EVOH27	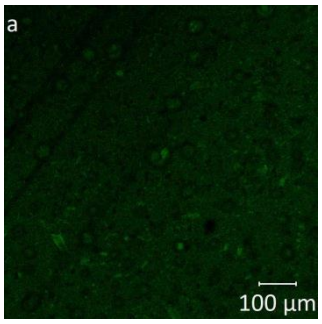	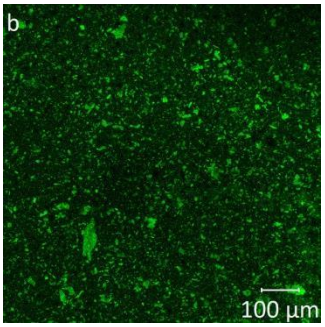	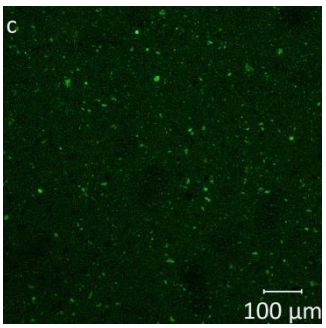
EVOH38	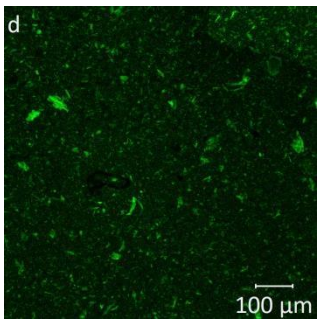	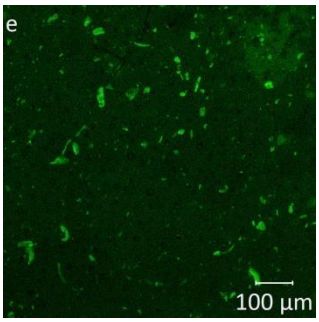	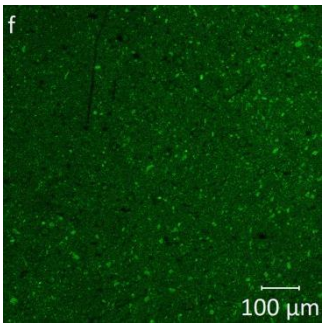
EVOH44	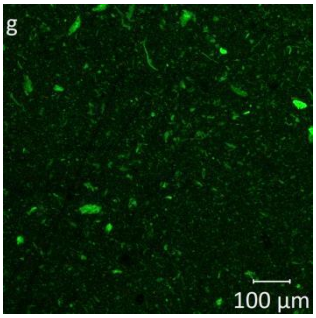	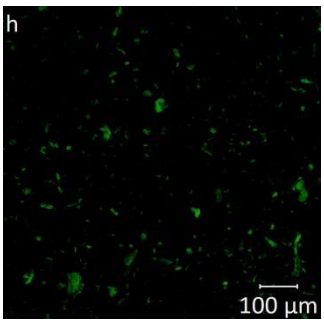	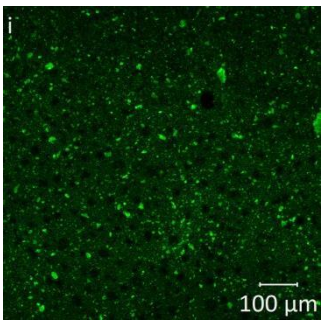
LDPE	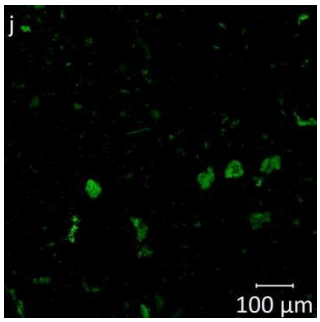	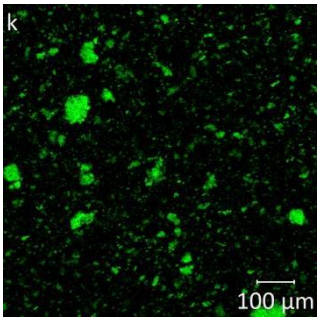	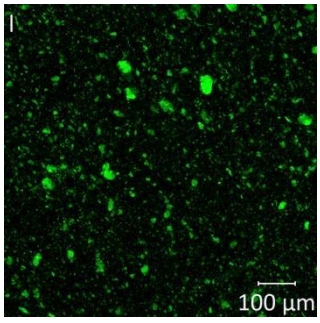

The nanoparticle distributions, throughout the depth of the nanocomposite films, were analysed by z-stack analysis. Figure 5.4-3 shows the z-stack results for the EVOH38_3%_CNP nanocomposite film. The image shows that the nanoparticles were detected throughout the depth of the film sample and were not only limited to the sample surface. This confirmed that the added nanoparticles were partially imbedded within the polymer matrices and the nanofillers may therefore potentially have an insignificant effect on the surface modification of the nanocomposite materials.

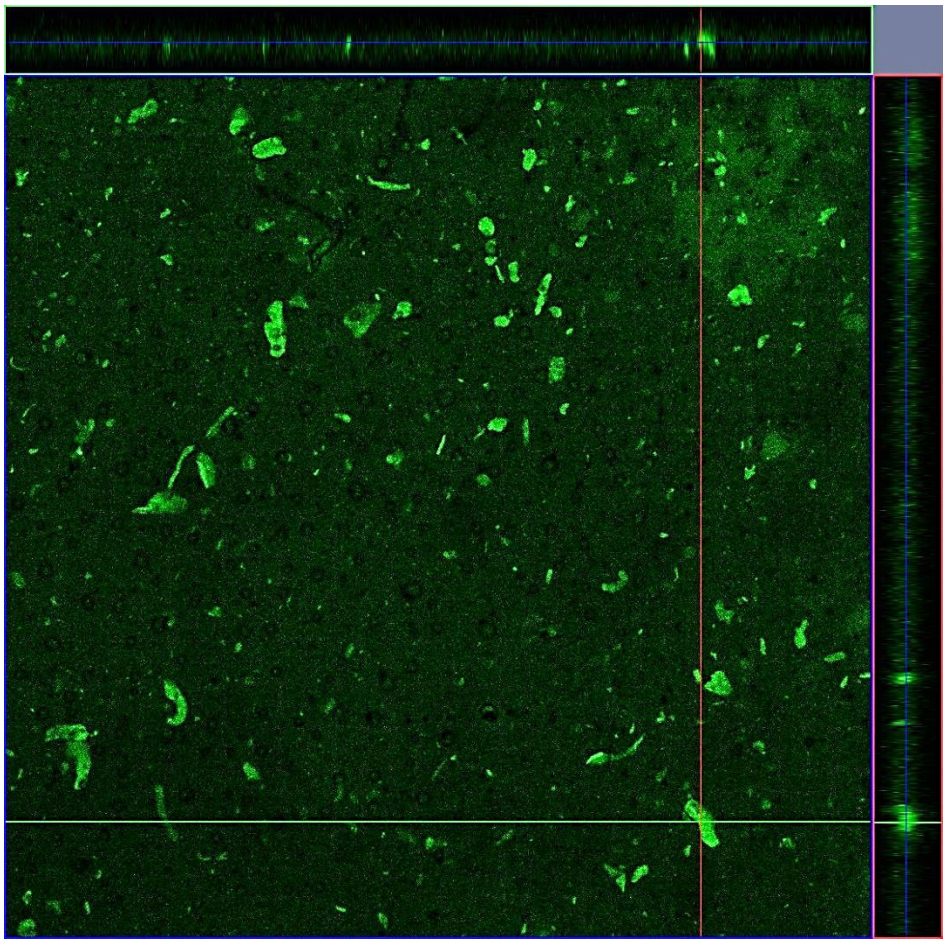

Figure 5.4-3: Z-stack analysis of the EVOH38_3%_CNP nanocomposite film showing the distribution of CNP throughout the depth of the sample.

The nanocomposite films, using EVOH27 and EVOH38 as matrices, showed a homogenous distribution of the nanoparticles. Some of the nanoparticles did, however, still agglomerate. The EVOH44 and LDPE matrices showed significantly more nanoparticle agglomeration and this can be attributed to a lack of interaction between the fillers and matrices. The hydroxyl functionalities of the EVOH matrices therefore have a significant influence on the homogenous distribution of these nanofillers within the produced nanocomposites. The LDPE matrix, which

has no hydroxyl functionalities, revealed the most agglomeration, irrespective of type nanoparticle type.

5.5 Differential scanning calorimetry (DSC) analysis

The results for the DSC analyses of the LDPE nanocomposite films are shown in Figure 5.5-1. No significant change can be noted for the melting or crystallisation temperatures of the nanocomposite materials, irrespectively of the type of nanoparticle and filler content. The enthalpy of melting and crystallisation was also investigated and are shown in Table 5.5-1.

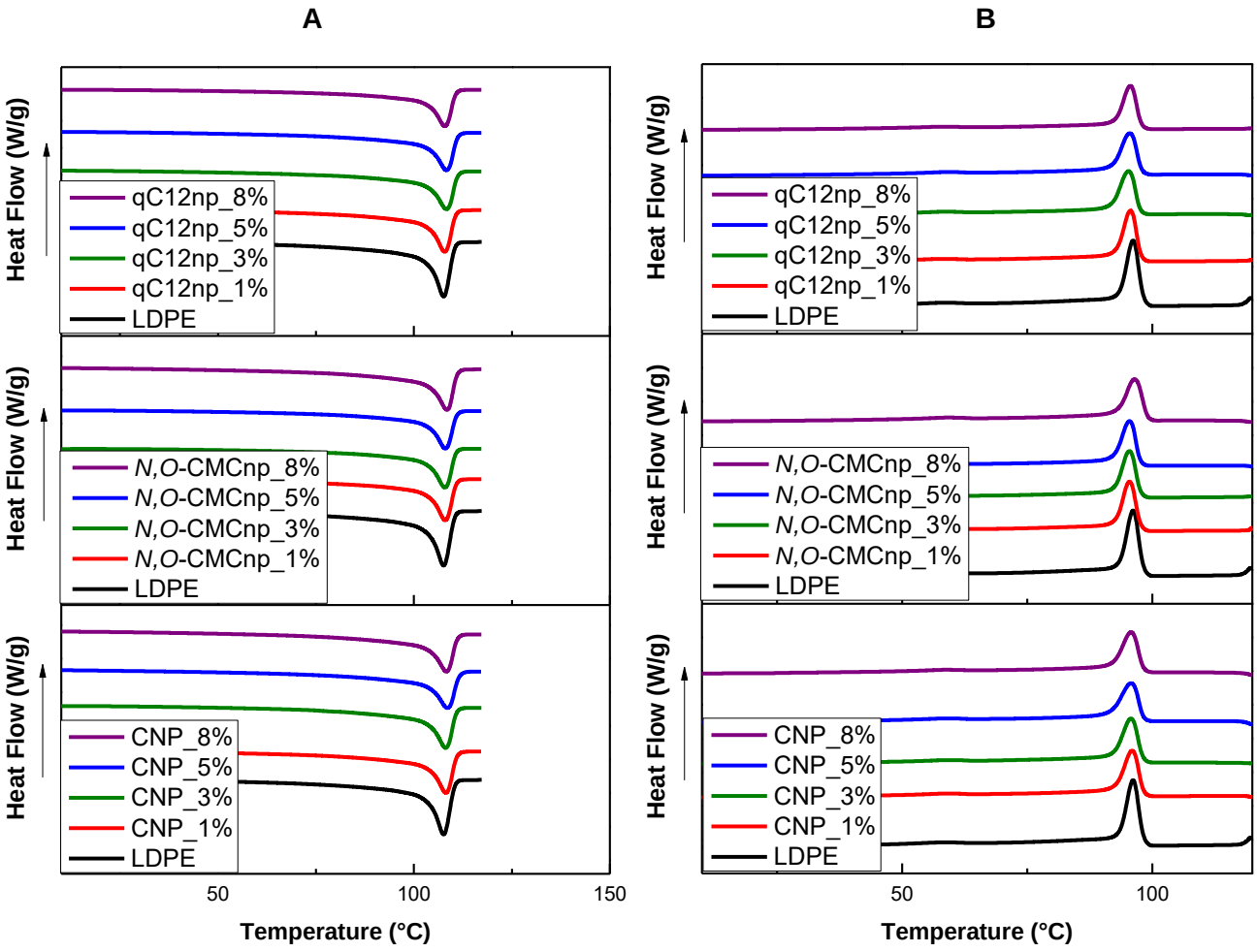

Figure 5.5-1: DSC curves of LDPE nanocomposite films during (A) the second heating cycle and (B) cooling cycle.

The results in Table 5.5-1 confirm the small variations in melting and crystallisation temperatures. The enthalpy of melting and crystallisation also decreased with an increase in filler content. The most significant decrease in enthalpy values were noticed after the addition of 1 wt% nanofiller. This can be attributed to the nanoparticles inhibiting the close packing of

polyethylene chains and chitosan acting as a non-crystalline component in the composite[2,3]. This could explain the decrease in measured enthalpy values while the melting and crystallisation temperatures remain unchanged[4–6]. Therefore, it was shown that the addition of a small amount of nanofiller (1wt%) could influence the thermal properties of nanocomposite materials.

Table 5.5-1: Summary of the DSC results for LDPE nanocomposite films during the second heating cycle and the cooling event

	Melting			Crystallisation	
Sample	**T_m (°C)**	**H_m (J/g)**		**T_c (°C)**	**H_c (J/g)**
LDPE	107.6	127.0		96.2	127.1
LDPE_1%_CNP	108.2	109.0		96.0	103.1
LDPE_3%_CNP	108.1	101.0		95.8	104.9
LDPE_5%_CNP	108.5	104.0		95.8	100.8
LDPE_8%_CNP	108.3	96.0		95.8	100.7
LDPE_1%_*N,O*-CMCnp	108.0	102.0		95.4	100.4
LDPE_3%_ *N,O*-CMCnp	108.0	97.0		95.4	96.6
LDPE_5%_ *N,O*-CMCnp	108.0	95.0		95.5	96.1
LDPE_8%_ *N,O*-CMCnp	108.0	107.0		96.5	106.3
LDPE_1%_qC12np	108.0	104.0		95.7	102.7
LDPE_3%_qC12np	108.0	102.0		95.3	98.3
LDPE_5%_qC12np	108.0	100.0		95.5	96.0
LDPE_8%_qC12np	108.0	92		95.6	90.6

Similar analysis was performed on the EVOH27, EVOH38 and EVOH44 nanocomposite films. The results for EVOH44 nanocomposites are shown in Figure 5.5-2 and Table 5.5-2. The tabulated results for EVOH27 and EVOH38 nanocomposite films are shown in Table A-1 and Table A-2 in Appendix A.

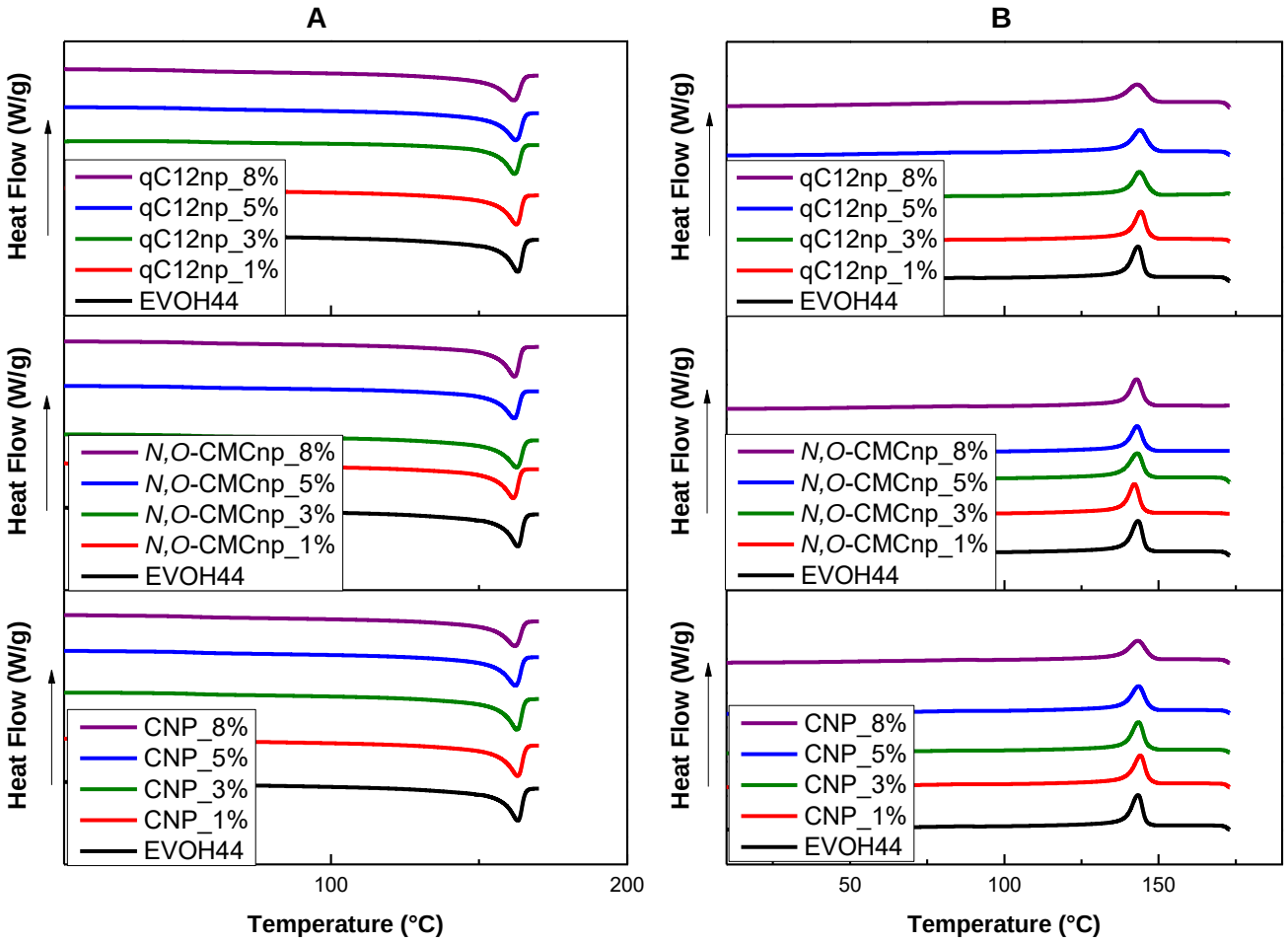

Figure 5.5-2: DSC curves of EVOH44 nanocomposite films during (A) the second heating cycle and (B) cooling cycle.

The melting and crystallisation temperatures of the EVOH44 nanocomposite films also appeared unaffected by the addition of the nanoparticles[7]. As in the case of the LDPE nanocomposites the melting enthalpy values of the EVOH44 nanocomposites were lower than that of the neat matrix and there was a clear decrease in these values as the CNP content increased. This decrease with increase in nanofiller content could not be seen as clearly in the case of the *N,*O-CMCnp and qC12np EVOH44 nanocomposites. The crystallisation enthalpy also decreased with the addition of nanofillers. An increase in CNP content caused a decrease in crystallisation enthalpy but this trend was not noted for the other two types of nanoparticles, although the crystallisation enthalpy values remained lower than that of the neat matrix. The absence of the expected trend could be due to nanoparticle agglomeration at nanofiller content above 3 wt%.

Table 5.5-2: DSC data for EVOH44 nanocomposite films during the second heating cycle and the cooling event.

	Melting			Crystallisation	
Sample	**T_m (°C)**	**H_m (J/g)**		**T_c (°C)**	**H_c (J/g)**
EVOH44	163.0	65.5		143.3	63.3
EVOH44_1%_CNP	163.0	64.6		144.1	63.7
EVOH44_3%_CNP	162.8	62.0		143.4	62.0
EVOH44_5%_CNP	162.2	61.4		143.4	61.7
EVOH44_8%_CNP	162.1	56.4		143.3	55.4
EVOH44_1%_*N,O*-CMCnp	161.6	59.0		142.2	61.1
EVOH44_3%_*N,O*-CMCnp	162.7	61.7		143.0	60.2
EVOH44_5%_*N,O*-CMCnp	161.8	56.4		143.0	57.6
EVOH44_8%_*N,O*-CMCnp	162.0	58.4		142.8	60.1
EVOH44_1%_qC12np	162.6	60.3		144.2	61.5
EVOH44_3%_qC12np	162.0	58.4		143.8	57.3
EVOH44_5%_qC12np	162.4	61.6		144.0	59.6
EVOH44_8%_qC12np	161.7	60.1		143.0	57.0

5.6 Static contact angle (SCA) and water uptake measurements

5.6.1 Static contact angle (SCA) analysis

The nanocomposite films were subjected to static contact angle analyses to investigate the influence of the nanoparticle fillers on the hydrophobicity of the films. The results for the EVOH44 nanocomposite films are reported in Figure 5.6.1-1 . The contact angles increased, relative to the neat EVOH44 matrix, after the addition of 1 wt% CNP and decreased as the CNP content increased to 5 wt%. After increasing the CNP content to 8 wt% the contact angles started to increase once again. The addition of 1 wt% hydrophobic qC12np showed a decrease in contact angles but a steady increase as the qC12np content increased up to 8 wt%. Therefore, the expected increase in contact angles was only noticed at and above 5 wt%. The hydrophilic *N,O*-CMCnp showed the smallest influence on the contact angle values for the nanocomposite films. A nanofiller content of 8 wt% was required to observe an increase in the contact angle values. This was also contrary to what was expected from the hydrophilic nanoparticles.

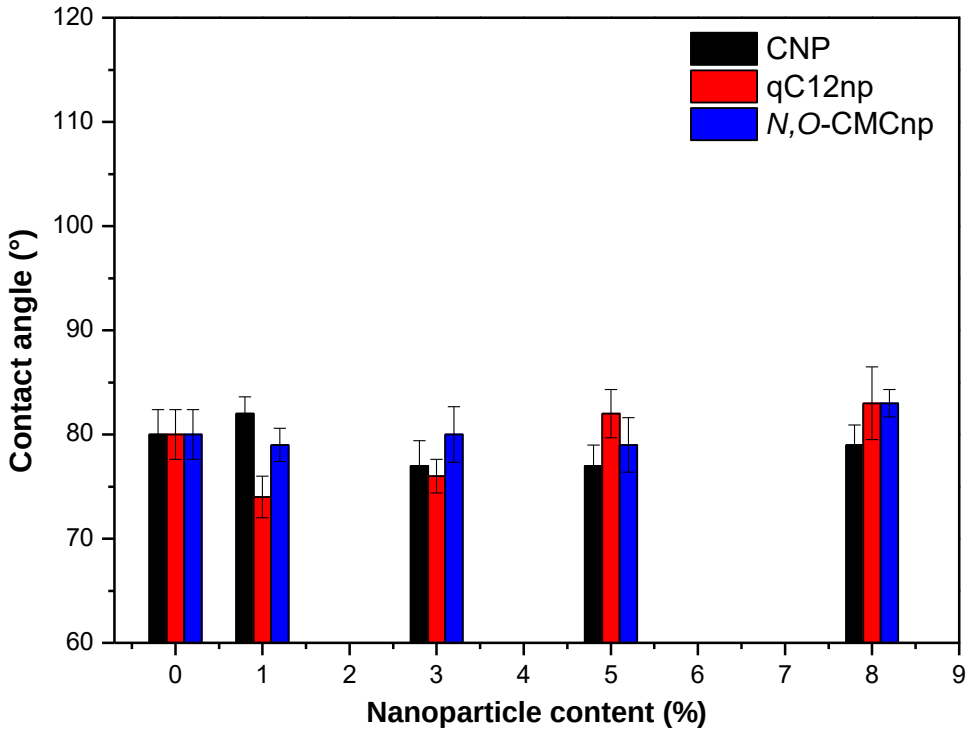

Figure 5.6.1-1: Static contact angle results for EVOH44 nanocomposite films with varying filler content.

The results for the LDPE nanocomposite films are reported in Figure 5.6.1-2. The contact angle values decreased, relative to the neat LDPE matrix, up to a nanofiller content of 5 wt%, irrespective of nanoparticle type. The 8 wt% nanofiller content films showed an overall increase in the contact angle values, relative to the 5 wt% nanofiller films, but the neat LDPE matrix remained to most hydrophobic film. This was attributed to increased nanoparticle agglomeration in the LDPE matrix at filler content of 8 wt%. This absence of the expected effects of the different nanoparticles on the contact angles of the EVOH and LDPE matrices can be due to insufficient amounts of nanoparticles present on the nanocomposite film surfaces to have a significant influence on the surface properties of the films, as shown in Chapter 5.2 and Chapter 5.4.

The decrease in hydrophobicity for the EVOH44 and LDPE composites at low filler loadings might be attributed to the amphiphilic nature of chitosan where the nanoparticles are more hydrophilic than the polymer matrices, irrespective of the chitosan functionalisation[3,6,8]. The noted increase in composite hydrophobicity at 8 wt% filler content might be due to particle agglomeration at the film surfaces which modifies the composite surface roughness.

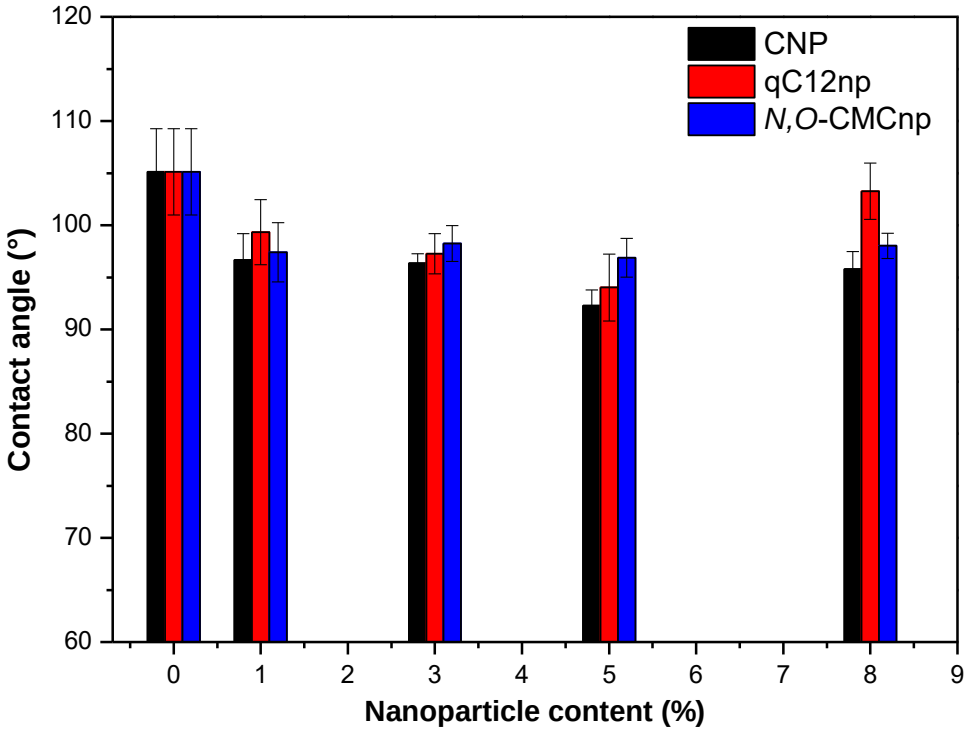

Figure 5.6.1-2: Static contact angle results for LDPE nanocomposite films with varying filler contents.

Contact angle results for the EVOH27 and EVOH38 nanocomposite films are shown in Figure A-4 and Figure A-5 in Appendix A respectively and show a similar lack of expected trends. Water uptake tests were carried out on these nanocomposite film samples for further investigation.

5.6.2 Water uptake

The EVOH44 nanocomposite films, in Figure 5.6.2-1, showed an increase in the rate of water uptake and maximum capacity with the introduction of the various nanoparticles[8]. Result variations between different nanoparticles remained insignificant up to 8 wt% filler content and therefore only the results of the nanocomposites with 8% filler are reported. The neat EVOH44 matrix reached maximum water uptake after 75 minutes while the nanocomposite films continued to absorb water after 2 hours. The hydrophilic *N,O*-CMCnp nanocomposites performed as expected and showed the strongest influence on the water uptake as the maximum capacity and rate of uptake was the most of all the tested samples.

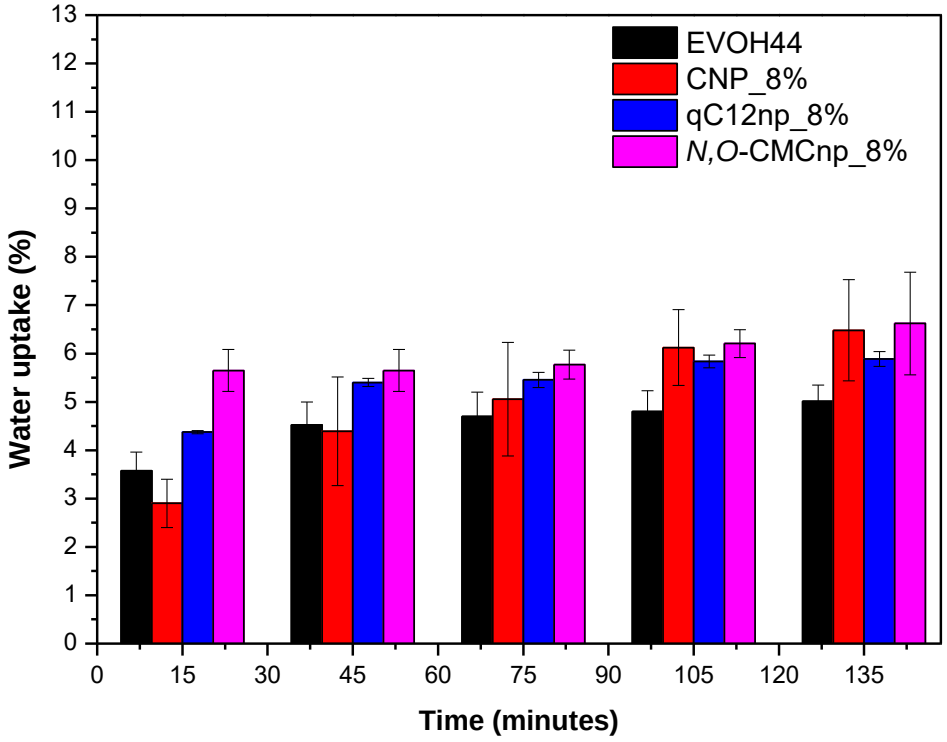

Figure 5.6.2-1: Water uptake results for EVOH44 nanocomposite films with 8 wt% nanoparticle content.

The results of the LDPE nanocomposite films, shown in Figure 5.6.2-2, also showed an increase in water uptake with the addition of any of the different nanoparticles. The results for the EVOH27 and EVOH38 nanocomposites are reported in Figure A-6 and Figure A-7 in Appendix A respectively. Similar experiments were performed for the intermediate filler content films but were omitted. The LDPE nanocomposite film with 8 wt% CNP reached maximum water uptake after 15 minutes. The hydrophilic *N,O*-CMCnp nanocomposite film absorbed the least amount of water out of all the nanocomposites and reached a maximum capacity after 15 minutes. This could be due to a lack of interaction between the filler material and the LDPE matrix which leads to nanoparticle agglomeration. The hydrophobic qC12np nanocomposite film had the slowest rate of water uptake, as was expected, and absorbed a maximum amount of water after 2 hours. The general observed trend, however, showed that an increase in filler content resulted in an increased maximum water uptake, irrespective of matrix or nanoparticle derivative. Therefore, all three different types of nanoparticles seem to promote hydrophilicity of the LDPE and EVOH matrices[3,6,8].

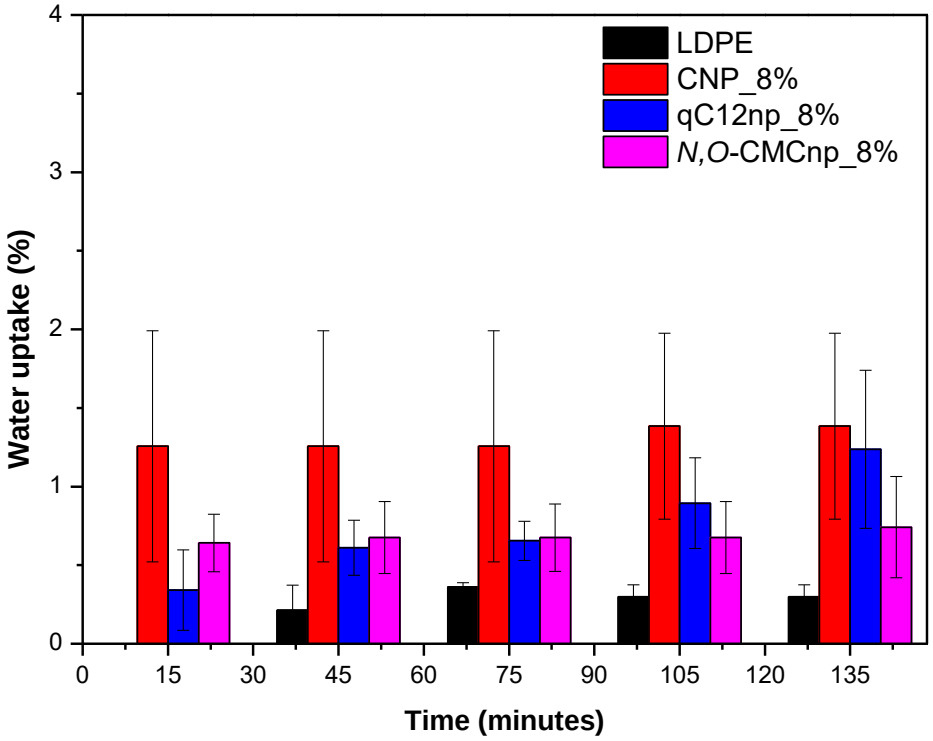

Figure 5.6.2-2: Water uptake results for LDPE nanocomposite films with 8 wt% nanoparticle content.

5.7 Tensile testing

Tensile testing was performed on nanocomposite materials with LDPE and EVOH44 matrices. Table 5.7-1 summarises the tensile test results for the LDPE nanocomposites. Young's modulus increased with increasing nanoparticle content, relative to neat LDPE[2]. The maximum stress remained largely unaffected by the addition of the three types of nanoparticles. A previous study from literature reported that the addition of chitosan (up to 2 wt%) to LDPE matrices led to a decrease in tensile strength[3]. This was attributed to the chitosan disrupting the crystalline structure of the LDPE films and the lack of interaction between the hydrophobic LDPE matrix and the polar sites of the chitosan[9]. Despite this, the observed variations in the tensile strength of the LDPE nanocomposites were not significant. Lastly, the elongation of the nanocomposites decreased significantly as the filler content increased and can be attributed to chitosan acting as a nucleating agent which reduced the elasticity of the nanocomposites[2,3,5].

Table 5.7-1: Tensile testing results for LDPE nanocomposite materials

	Max Load (N)		Elongation (%)		Young's Modulus (MPa)	
Sample	**Mean**	**STDEV**	**Mean**	**STDEV**	**Mean**	**STDEV**
LDPE	22.8	2.1	195.6	78.3	218.9	12.5
LDPE_1%_CNP	23.7	1.1	238.4	96.2	197.6	5.0
LDPE_3%_CNP	22.4	0.6	56.1	13.5	251.9	23.3
LDPE_5%_CNP	22.0	1.0	61.5	18.3	262.1	19.8
LDPE_8%_CNP	21.9	1.0	31.0	12.8	267.7	34.1
LDPE_1%_*N,O*-CMCnp	21.4	0.8	97.1	34.6	195.3	17.1
LDPE_3%_ *N,O*-CMCnp	19.3	2.1	30.2	14.3	203.8	40.1
LDPE_5%_ *N,O*-CMCnp	20.2	1.6	22.8	6.0	221.1	26.1
LDPE_8%_ *N,O*-CMCnp	19.0	3.8	20.2	12.5	225.6	8.8
LDPE_1%_qC12np	21.4	0.6	95.5	48.1	221.3	10.9
LDPE_3%_qC12np	20.9	1.3	54.5	20.9	224.3	30.8
LDPE_5%_qC12np	22.3	0.3	39.0	21.5	267.5	22.9
LDPE_8%_qC12np	21.0	1.6	34.7	21.7	225.6	10.9

Similar analyses were performed on nanocomposites with EVOH44 as a matrix and the results are summarised in Table 5.7-2. The maximum stress decreased with increasing filler content and was attributed to a lack of sufficient interfacial interaction between the EVOH44 matrix and the nanoparticles[9]. The elongation at break showed a similar decrease with increasing filler content, while the Young's modulus remained largely unaffected.

Table 5.7-2: Tensile testing results for EVOH44 nanocomposite materials

	Max Load (N)		Elongation (%)		Young's Modulus (MPa)	
Sample	**Mean**	**STDEV**	**Mean**	**STDEV**	**Mean**	**STDEV**
EVOH44	134.1	18.6	48.7	66.8	2104.1	96.8
EVOH44_1%_CNP	117.5	18.9	6.0	3.9	2050.8	145.1
EVOH44_3%_CNP	134.9	15.3	4.9	1.7	2288.7	165.3
EVOH44_5%_CNP	85.6	27.3	2.1	0.5	2125.9	380.3
EVOH44_8%_CNP	94.9	24.5	2.4	0.7	2126.5	294.7
EVOH44_1%_ *N,O*-CMCnp	65.5	9.8	44.3	27.3	784.9	250.7
EVOH44_3%_ *N,O*-CMCnp	54.2	6.2	35.8	12.1	542.8	92.6
EVOH44_5%_ *N,O*-CMCnp	58.1	4.5	37.3	28.7	652.4	59.1
EVOH44_8%_ *N,O*-CMCnp	58.1	3.4	46.3	17.9	534.4	53.1
EVOH44_1%_qC12np	135.1	10.8	5.0	0.5	2207.4	99.9
EVOH44_3%_qC12np	131.7	20.2	4.6	2.1	2203.7	72.5
EVOH44_5%_qC12np	124.5	28.0	5.0	3.6	2180.5	191.9
EVOH44_8%_qC12np	89.4	16.5	2.0	0.4	2072.2	203.8

5.8 Antimicrobial testing

The antimicrobial activity of chitosan and its derivative depend on the type of bacteria tested[10]. The nanocomposite film samples were exposed to *Staphylococcus aureus* (*S. aureus*) for antimicrobial testing, as described in Chapter 3.3. The sample layout in the petri dishes was discussed in Chapter 3.3.11. The purpose of the antimicrobial testing was to investigate whether a correlation exists between the hydrophobicity of the different types of nanoparticles and the antimicrobial properties of the nanocomposite films[11]. The EVOH44 and LDPE matrices were selected to represent hydrophilic and hydrophobic matrices, respectively.

The nanocomposite films were tested for immediate growth inhibition of *S. aureus* and the results are shown in Figure 5.8-1. The alamarBlue indicator remained blue while making contact with the film surface, which was previously exposed to *S. aureus*, and showed no cell metabolism. The results from Figure 5.8-1 show no dependence towards the nanoparticle content. The blank EVOH44 film (sample in the middle) appeared to show some antimicrobial activity, although no nanoparticles were present in this sample. The samples were incubated to determine whether halo formation occurred and the results are shown in Figure 5.8-2. This confirmed whether any nanoparticles or residual solvent leached out of the films[10,12].

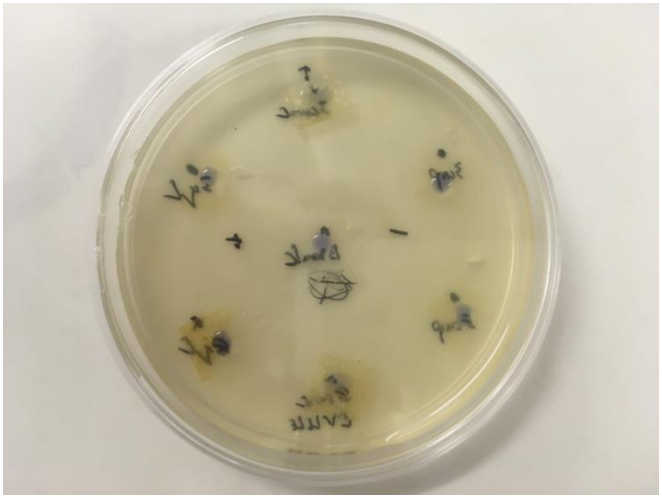

Figure 5.8-1: Antimicrobial results for EVOH44 nanocomposite films exposed to *Staphylococcus aureus* (*S. aureus*) to investigate direct inhibition.

The bacterial staining, shown in Figure 5.8-2, indicated that no halo formation was present around the nanocomposite samples. This meant that the nanoparticle fillers did not create a zone of inhibition. A similar result was observed for the LDPE nanocomposite films and is shown in Figure 5.8-3.

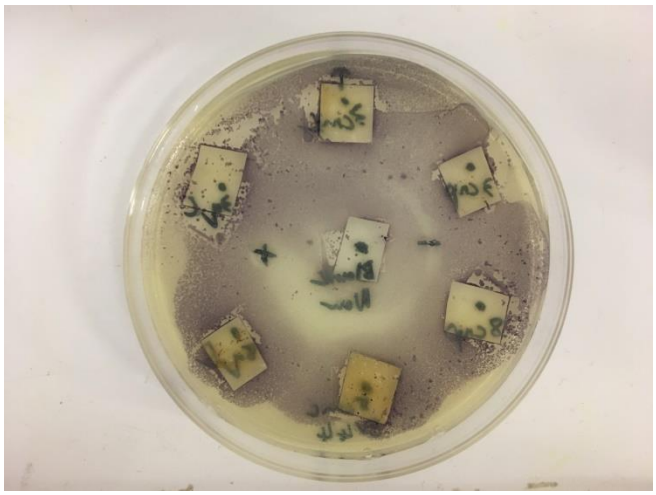

Figure 5.8-2: Antimicrobial results for EVOH44 nanocomposite films exposed to *Staphylococcus aureus* (*S. aureus*) after incubation to investigate halo formation.

According to Figure 5.8-2 and Figure 5.8-3 *S. aureus* did not grow on any of the polymer films and this may be due to the EVOH44 and LDPE matrices being too hydrophobic for *S. aureus* to attach onto the nanocomposite films. This meant that the effect of the filler material could not be determined as the hydrophobicity of the polymer matrices was the dominant factor.

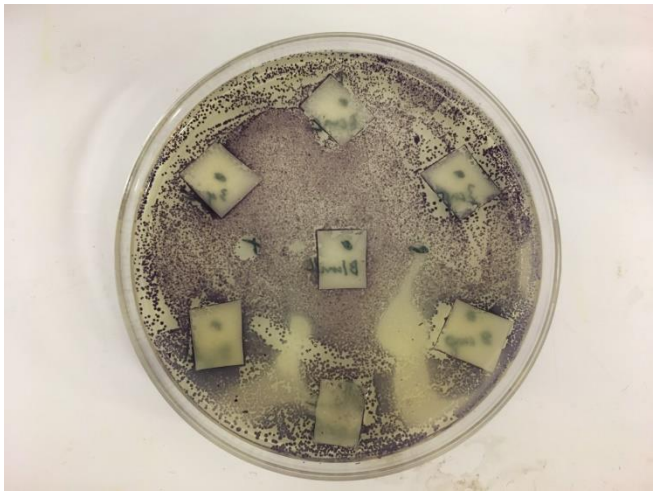

Figure 5.8-3: Antimicrobial results for LDPE nanocomposite films exposed to *Staphylococcus aureus* (*S. aureus*) after incubation to investigate halo formation.

5.9 Conclusions

The CFM analysis successfully showed the distribution of CNP, qC12np and *N,O*-CMCnp in EVOH and LDPE film matrices. The hydrophobicity of the nanocomposite matrices appeared to have had a more significant impact on the nanoparticle distribution, relative to the nanoparticle hydrophobicity. The absence of visible nanoparticles during SEM-EDS indicated that a significant amount of nanoparticles were imbedded within the nanocomposite films. The 3D results of the CFM analysis showed the distribution of nanoparticles throughout the depth of the films. Optical images and UV/Vis was successfully used to show the correlation between nanoparticle content and nanocomposite film transparency. Water uptake studies showed that the addition of all three types of chitosan nanoparticles increased the maximum water uptake of EVOH and LDPE nanocomposite films. The poor correlation of results from the water uptake studies with those from SCA measurements can be attributed to a low concentration of nanoparticles on the nanocomposite film surfaces.

The thermal data from DSC showed that the addition of up to 8 wt% of the three types of chitosan nanoparticles had an insignificant influence on the melting and crystallisation temperatures of the EVOH and LDPE matrices. The addition of 1 wt% nanofiller already caused a decrease in the crystallisation and melting enthalpy of the EVOH and LDPE matrices. The physical properties of the nanocomposite films were evaluated by tensile testing and showed that the LDPE nanocomposites showed a small increase in Young's modulus and a decrease in elongation as the nanoparticle content increased. The EVOH44 nanocomposites showed a decrease in stress and elongation at break, irrespective of the type of nanoparticle filler. The antimicrobial activity of the nanocomposite films proved inconclusive. The lack of growth of *S. aureus* was possibly due to the hydrophobicity of the polymer matrices which hindered the attachment of *S. aureus*. A decision was made that a different physical structure (nanofibres) for the matrices should be used in order to further investigate the effect of the produced nanoparticles on the surface properties of the nanocomposite material. These results are discussed in the following chapter.

5.10 References

1. Van der Westhuizen, B. J. C. Polyester functionalisation for mycobacterial capture (MSc). (University Stellenbosch, 2018).

2. Vasile, C., Darie, R. N., Cheaburu-Yilmaz, C. N., Pricope, G. M., Bračič, M., Pamfil, D., Hitruc, G. E. & Duraccio, D. Low density polyethylene - Chitosan composites. *Compos. Part B Eng.* **55**, 314–323 (2013).

3. Park, S. Il, Marsh, K. S. & Dawson, P. Application of chitosan-incorporated LDPE film to sliced fresh red meats for shelf life extension. *Meat Sci.* **85**, 493–499 (2010).

4. Rogovina, S. Z., Aleksanyan, K. V., Novikov, D. D., Prut, E. V. & Rebrov, A. V. Synthesis and investigation of polyethylene blends with natural polysaccharides and their derivatives. *Polym. Sci. - Ser. A* **51**, 554–562 (2009).

5. Rogovina, S. Z., Alexanyan, C. V. & Prut, E. V. Biodegradable blends based on chitin and chitosan: Production, structure, and properties. *J. Appl. Polym. Sci.* **121**, 1850–1859 (2011).

6. Prasanna, K. & Sailaja, R. R. N. Blends of LDPE/chitosan using epoxy-functionalized LDPE as compatibilizer. *J. Appl. Polym. Sci.* **124**, 3264–3275 (2012).

7. du Toit, M. L. Incorporation of polysaccharide nanowhiskers into a poly (ethylene-co-vinyl alcohol) matrix (MSc). (University Stellenbosch, 2013).

8. Fernandez-Saiz, P., Ocio, M. J. & Lagaron, J. M. Antibacterial chitosan-based blends with ethylene-vinyl alcohol copolymer. *Carbohydr. Polym.* **80**, 874–884 (2010).

9. Tanjung, F. A., Husseinsyah, S., Hussin, K. & Hassan, A. Mechanical and thermal properties of organosolv lignin/sodium dodecyl sulphate binary agent-treated polypropylene/chitosan composites. *Polym. Bull.* **73**, 1427–1445 (2016).

10. Jung, E. J., Youn, D. K., Lee, S. H., No, H. K., Ha, J. G. & Prinyawiwatkul, W. Antibacterial activity of chitosans with different degrees of deacetylation and viscosities. *Int. J. Food Sci. Technol.* **45**, 676–682 (2010).

11. Sahariah, P., Benediktssdóttir, B. E., Hjálmarsdóttir, M. A., Sigurjonsson, O. E., Sørensen, K. K., Thygesen, M. B., Jensen, K. J. & Másson, M. Impact of chain length on antibacterial activity and hemocompatibility of quaternary N-alkyl and N, N-dialkyl chitosan derivatives. *Biomacromolecules* **16**, 1449–1460 (2015).

12. Tan, H., Ma, R., Lin, C., Liu, Z. & Tang, T. Quaternized chitosan as an antimicrobial agent: Antimicrobial activity, mechanism of action and biomedical applications in orthopedics. *Int. J. Mol. Sci.* **14**, 1854–1869 (2013).

CHAPTER 6

RESULTS AND DISCUSSION – ELECTROSPINNING OF EVOH NANOCOMPOSITES

6.1 Introduction

In this chapter three grades of poly(vinyl alcohol-co-ethylene) (EVOH) were individually eletrospun with each of unmodified chitosan nanoparticles (CNP), *N,O*-carboxymethyl chitosan nanoparticles (*N,O*-CMCnp) and quaternary ammonium chitosan nanoparticles (qC12np) at varying loadings. The EVOH matrices were once again denoted as EVOH27, EVOH38 and EVOH44 and the values of 27, 38 and 44 corresponded to the ethylene content (mole %) in the EVOH copolymers.

The influence of the nanoparticles on the electrospinning process and the nanocomposite fibre properties was investigated using scanning electron microscopy – energy dispersive X-ray spectrometer (SEM-EDS), differential scanning calorimetry (DSC), confocal fluorescence microscopy (CFM), water uptake, static contact angle (SCA) and antimicrobial studies.

6.2 Scanning electron microscopy (SEM)

Initial testing was done by electrospinning EVOH27, EVOH38 and EVOH44 polymer solutions in order to find suitable polymer concentrations for the nanocomposite spinning solutions. This was also done in order to find a set of standard conditions for all further electrospinning samples. Figure 6.2-1 shows the electrospun nanofibres for EVOH27 at (a) 15 wt%, (b) 18 wt%, and (c) 20 wt% polymer solutions in dimethyl sulfoxide (DMSO).

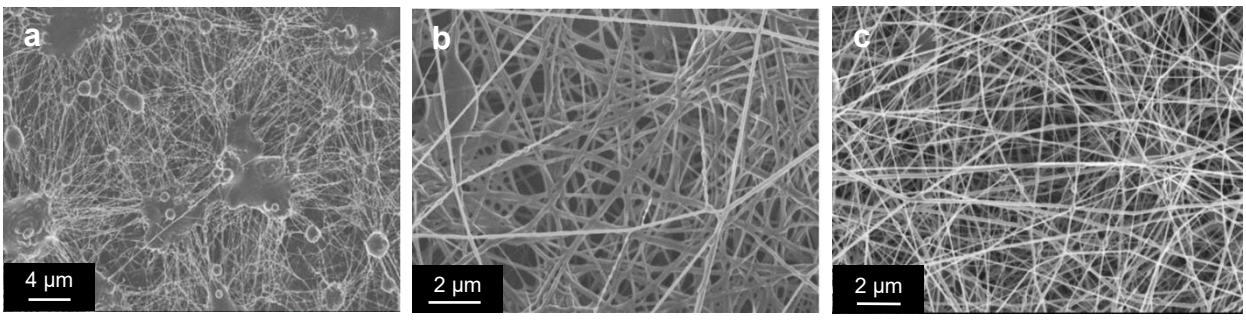

Figure 6.2-1: SEM images of electrospun EVOH27 nanofibres at (a) 15 wt%, (b) 18 wt% and (c) 20 wt% polymer solutions in DMSO.

A similar investigation was performed for the EVOH38 polymer and the SEM results are shown in Figure 6.2-2. EVOH38 could be electrospun at polymer concentrations lower than EVOH27 but this was not investigated further seeing as the aim was to electrospin all samples at similar

conditions. Figure 6.2-2 shows the EVOH38 electrospun nanofibres at (a) 12 wt%, (b) 15 wt%, (c) 18 wt% and (d) 20 wt% polymer solution in DMSO.

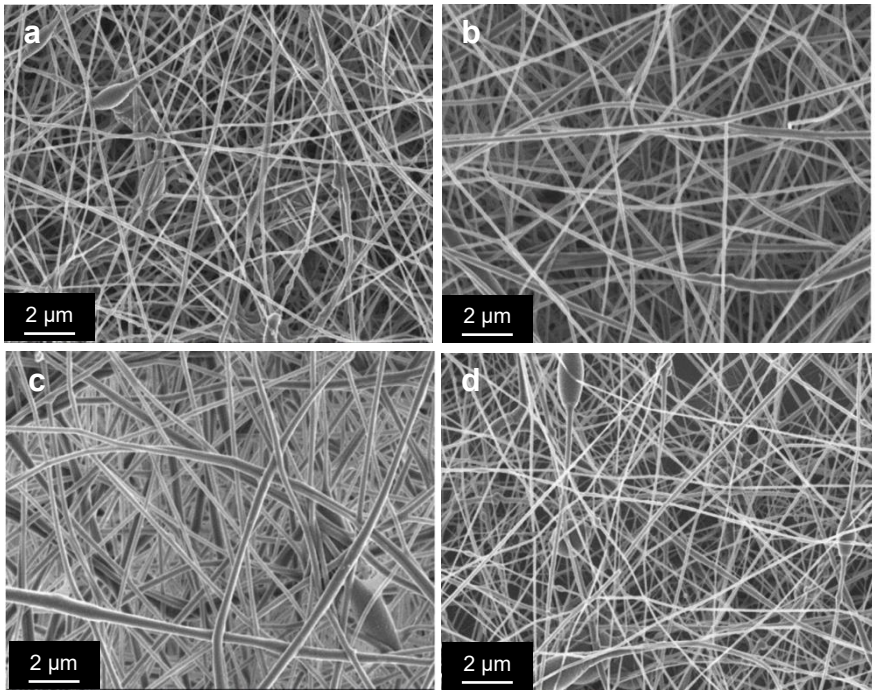

Figure 6.2-2: SEM images of electrospun EVOH38 nanofibres at (a) 12 wt%, (b) 15 wt%, (c) 18 wt% and (d) 20 wt% polymer solutions in DMSO.

The electrospun EVOH44 samples had uniform fibre diameters and confirmed that the EVOH polymers could be electrospun in the polymer concentration range of 15-20 wt% in a DMSO solvent system. The SEM images of EVOH44 nanofibres are shown in Figure 6.2-3. It was also found that an increase in ethylene content in the EVOH polymers improved its electrospinning capabilities, as uniform nanofibres could not be obtained for EVOH27 at 15 wt% polymer concentrations.

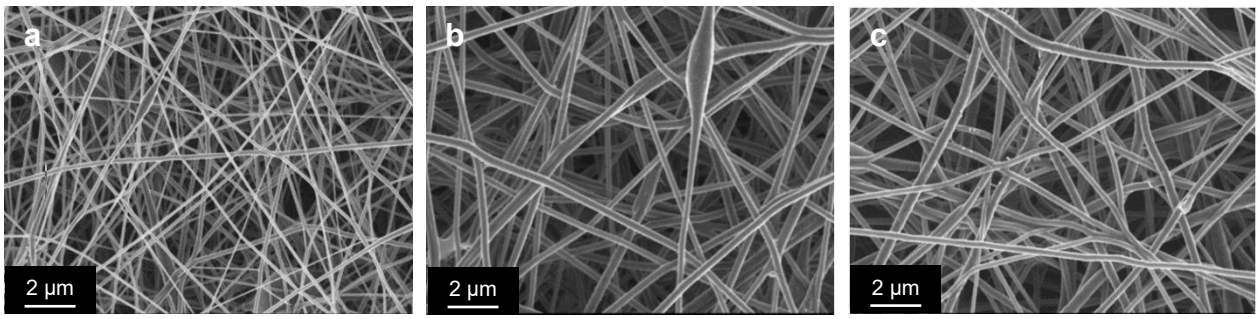

Figure 6.2-3: SEM images of electrospun EVOH44 nanofibres at (a) 15 wt%, (b) 18 wt% and (c) 20 wt% polymer solutions in DMSO.

The fibre diameters of the initial electrospinning investigation are revealed in Figure 6.2-4. The generally observed trend was that the fibre diameter increased with polymer concentration, up to 18 wt%, and with an increase in ethylene comonomer content in the EVOH copolymers[1]. Based on the results of Figure 6.2-4, a 20 wt% polymer solution was selected as an initial starting concentration for the electrospinning of the nanocomposite polymers.

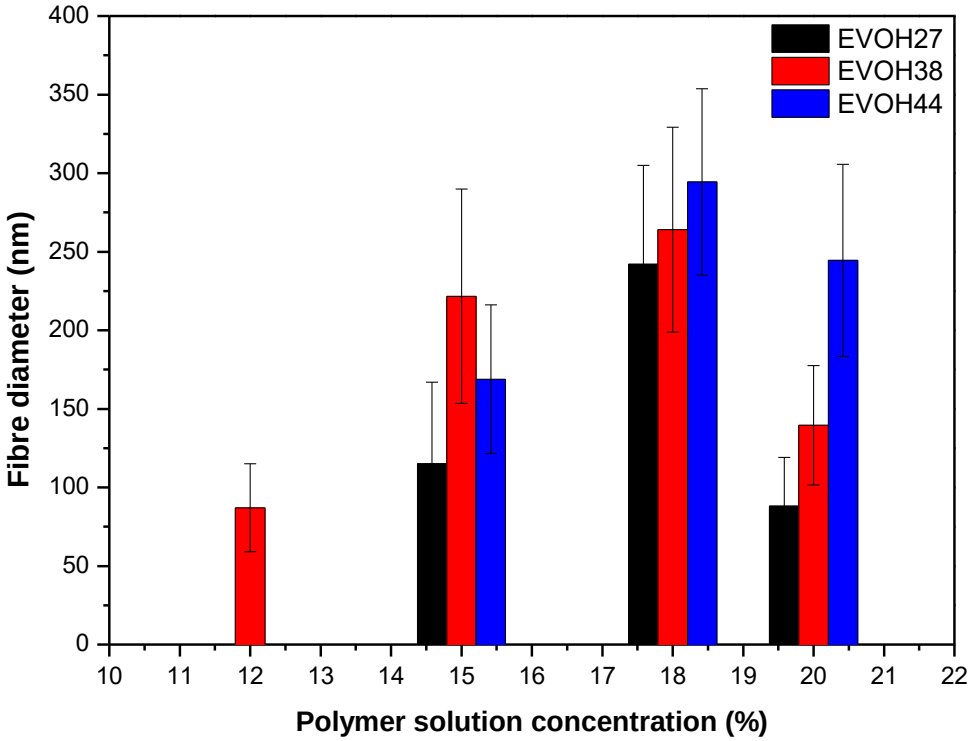

Figure 6.2-4: Fibre diameter of electrospun EVOH27, EVOH38 and EVOH44 polymer solutions.

In order to determine whether the 20 wt% polymer concentrations would work for all the planned samples (listed in Chapter 3) the electrospinning was performed on all three EVOH matrices with a 8 wt% CNP content. During these experiments the EVOH38_8%_CNP and EVOH44_8%_CNP electrospinning solutions tended to cause needle blockage and it was concluded that the addition of the nanoparticle fillers increased the solution viscosity to a point where fibres could not be drawn effectively. Therefore, the EVOH38 and EVOH44 nanocomposite polymers were electrospun at 15 wt%.

Needle blockage did not occur in the case of the EVOH27_8%_CNP electrospinning, but rather fibre fusion upon making contact with the collector plate. This effect is shown in Figure 6.2-5, which was due to the DMSO not being able to evaporate fast enough during the electrospinning process. The fibre formation of EVOH27 at polymer concentrations lower than 20 wt% was already shown to be unsuccessful according to Figure 6.2-1. The polymer concentration could also not be increased to more than 20 wt% as this led to needle blockage for EVOH27.

Therefore, the EVOH27 electrospinning solutions were kept at 20 wt% polymer, even though fibre formation was not obtained for certain nanoparticle loadings.

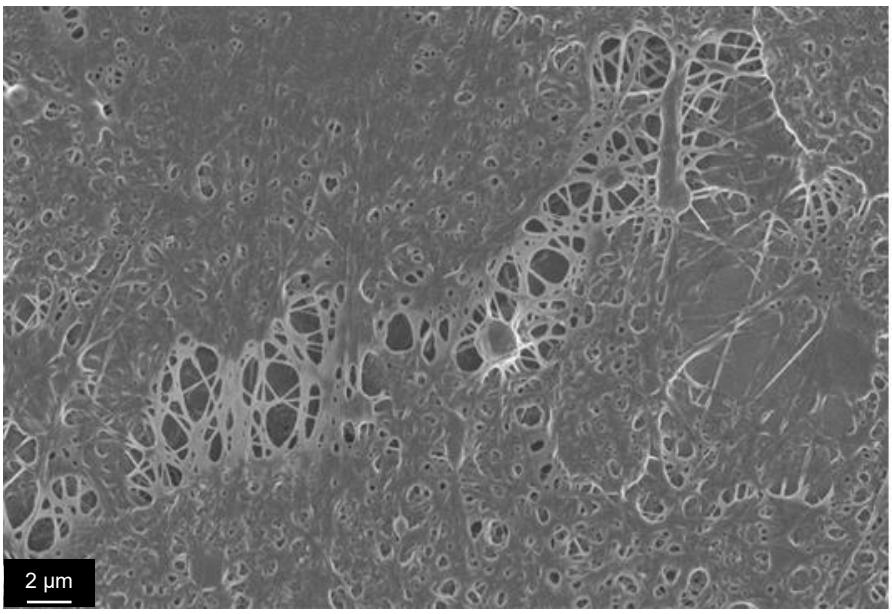

Figure 6.2-5: SEM image of electrospinning attempt of EVOH27_8%_CNP with an electrospinning solution with 20 wt% polymer in DMSO.

The viscosity measurements shown in Table 6.2-1 confirmed the observed electrospinning trends of the SEM analysis. The addition of 8 wt% CNP into EVOH27 reduced the viscosity of the electrospinning solution from 1852 mPa.s to 800 mPa.s and corresponded to the fibre fusion seen in Figure 6.2-1 (a) and Figure 6.2-5. The viscosities of EVOH44 and EVOH44_8%_CNP remained roughly the same and resulted in uniform nanofibres being electrospun for all the nanocomposites using EVOH44 as a matrix.

Table 6.2-1: Viscosity measurements of EVOH27 and EVOH44 electrospinning solutions at 15 wt% polymer in DMSO

	Electrospinning solution at 15 wt%			
	EVOH27	**EVOH27_8%_CNP**	**EVOH44**	**EVOH44_8%_CNP**
Viscosity (mPa.s)	1852	800	1810	2300

The results for the electrospun EVOH27 composites are shown in Table 6.2-2. The successful electrospinning of EVOH27 nanofibres became difficult at 5 and 8 wt% nanoparticle content. This corresponded to the results discussed above.

Table 6.2-2: Fibre diameter analysis of EVOH27 nanocomposites at 20 wt% polymer in DMSO. (Mean diameters calculated from an average of 200 fibres from SEM analysis.)

EVOH27_20%		
	Mean (nm)	**Standard deviation (nm)**
EVOH27_blank_15	115	52
EVOH27_blank_18	242	63
EVOH27_blank_20	88	31
EVOH27_1%	177	50
EVOH27_3%	155	57
EVOH27_5%	--	--
EVOH27_8%	--	--
EVOH27_1%_qC12np	142	35
EVOH27_3%_qC12np	258	79
EVOH27_5%_qC12np	152	56
EVOH27_8%_qC12np	--	--
EVOH27_1%_*N,O*-CMCnp	192	57
EVOH27_3%_*N,O*-CMCnp	171	49
EVOH27_5%_*N,O*-CMCnp	162	35
EVOH27_8%_*N,O*-CMCnp	--	--

The electrospinning results for the EVOH38 and EVOH44 matrices are summarised in Table 6.2-3. The fibre diameters of the EVOH38 nanocomposites showed to be larger than those of the EVOH44 nanocomposites. The measured viscosities for the neat 15 wt% EVOH38 and EVOH44 electrospinning solutions were 2936 mPa.s and 1810 mPa.s, respectively. The variation in fibre diameter can be attributed to the difference in viscosity of the two matrices[1,2]. The general trend from Table 6.2-3 shows that the EVOH38 nanofibre diameters were larger than the EVOH44 nanofibres, irrespective of the nanoparticle type or weight content.

Table 6.2-3: Fibre diameter analysis of EVOH38 and EVOH44 nanocomposites at 15 wt% polymer in DMSO. (Mean diameters calculated from an average of 200 fibres from SEM analysis.)

EVOH38_15%				**EVOH44_15%**		
	Mean (nm)	**Standard deviation (nm)**			**Mean (nm)**	**Standard deviation (nm)**
EVOH38_blank_15	222	68		**EVOH44_blank_15**	169	47
EVOH38_blank_18	264	65		**EVOH44_blank_18**	294	59
EVOH38_blank_20	140	38		**EVOH44_blank_20**	244	61
EVOH38_1%	251	45		**EVOH44_1%**	219	80
EVOH38_3%	231	50		**EVOH44_3%**	213	80
EVOH38_5%	150	36		**EVOH44_5%**	146	58
EVOH38_8%	272	61		**EVOH44_8%**	163	49
EVOH38_1%_qC12np	244	62		**EVOH44_1%_qC12np**	202	72
EVOH38_3%_qC12np	285	69		**EVOH44_3%_qC12np**	193	54
EVOH38_5%_qC12np	264	72		**EVOH44_5%_qC12np**	164	48
EVOH38_8%_qC12np	293	71		**EVOH44_8%_qC12np**	192	68
EVOH38_1%_*N,O*-CMCnp	268	59		**EVOH44_1%_*N,O*-CMCnp**	171	48
EVOH38_3%_*N,O*-CMCnp	234	61		**EVOH44_3%_*N,O*-CMCnp**	181	51
EVOH38_5%_*N,O*-CMCnp	231	57		**EVOH44_5%_*N,O*-CMCnp**	121	32
EVOH38_8%_*N,O*-CMCnp	220	49		**EVOH44_8%_*N,O*-CMCnp**	278	78

Figure 6.2-6 shows a photo of the successfully electrospun EVOH44_5%_CNP nanofibre mat. The nanofibre mats were successfully removed from the collector plate and maintained its physical shape after removal. Further analysis could therefore be performed on these nanofibre composites.

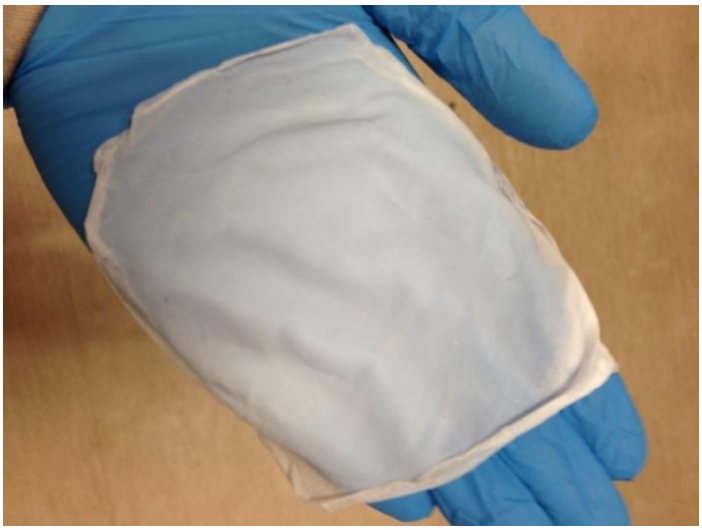

Figure 6.2-6: Electrospun EVOH44_5%_CNP at 15 wt% polymer in DMSO.

The EVOH44_5%_CNP fibre mat, shown in Figure 6.2-6, was submitted for SEM-EDS analysis to investigate the nanoparticle distribution and the result is shown in Figure 6.2-7. None of the characteristic elements, from the nanoparticles, were detected with SEM-EDS. This included nitrogen from the chitosan backbone and phosphorus from the crosslinking agent. These elements were also not detected during the SEM-EDS analysis of the EVOH44_5%_CNP nanocomposite film. The lack of observed characteristic elements was attributed to ineffective experimental conditions. The nitrogen and phosphorus might have been identified at higher electron beam intensities but unfortunately the EVOH matrix would have been destroyed. The nanoparticle distributions were probed further by using CFM and are discussed in later this chapter.

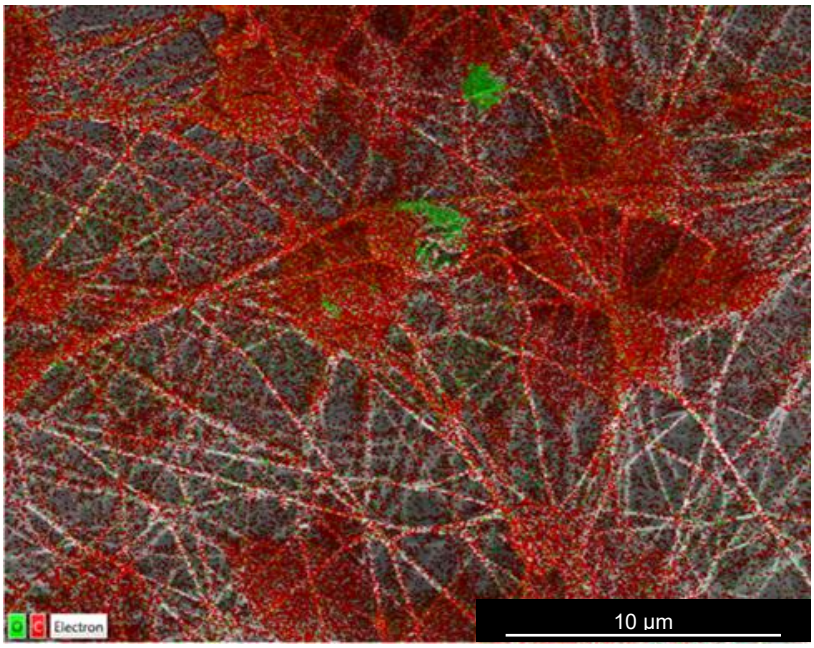

Figure 6.2-7: Elemental map of the electrospun EVOH44_5%_CNP sample.

6.3 Differential scanning calorimetry (DSC) analysis

The DSC analysis results of the EVOH44 electrospun nanocomposites are shown in Figure 6.3-1, with the results for EVOH38 available in Figure A-8 and Table A-3 in Appendix A. The EVOH27 composites were excluded due to their lack of fibre formation, as discussed in Chapter 6.2.

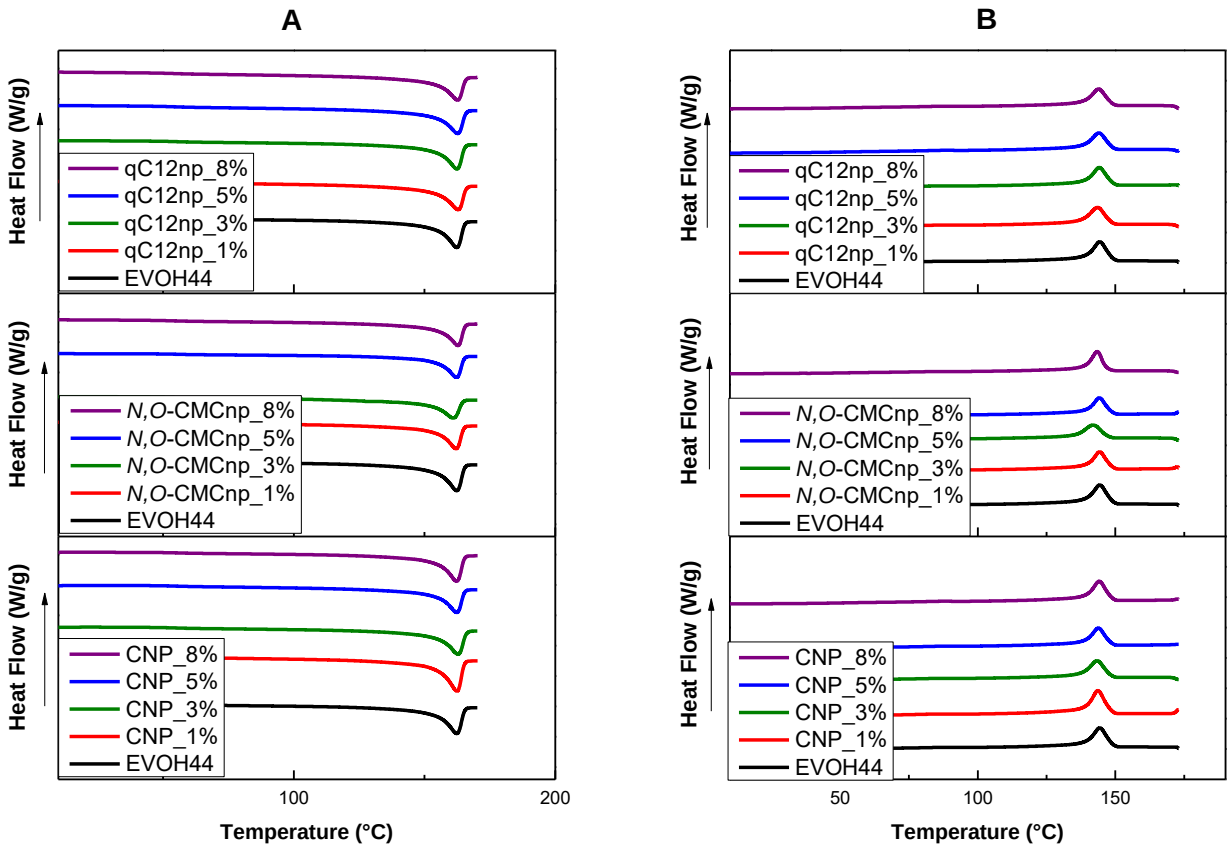

Figure 6.3-1: DSC curves of EVOH44 nanocomposite fibres during (A) the second heating cycle and (B) cooling cycle.

The results from Table 6.3-1 show no clear influence of nanoparticle filler content on the melting and crystallisation temperatures of the electrospun nanocomposites. The melting and crystallisation enthalpy of the neat EVOH44 matrix remained the largest of the tested samples, excluding EVOH44_1%_CNP. The general observed trend showed a decrease in enthalpy values as nanofillers were added to the EVOH44 matrix. These trends were attributed to chitosan acting as a non-crystalline component in the nanocomposite fibres which resulted in the decrease in crystallisation and melting enthalpies and no influence on melting and crystallisation temperatures[3–5]. Similar trends were noticed for the prepared nanocomposite films in Chapter 5.

Table 6.3-1: DSC data for EVOH44 nanocomposite fibres during the second heating cycle and the cooling event

	Melting			Crystallisation	
Sample	**T_m (°C)**	**H_m (J/g)**		**T_c (°C)**	**H_c (J/g)**
EVOH44	162.3	63.3		144.3	62.4
EVOH44_1%_CNP	162.4	71.3		143.7	72.9
EVOH44_3%_CNP	162.8	59.4		143.4	56.1
EVOH44_5%_CNP	162.4	55.8		143.8	53.5
EVOH44_8%_CNP	162.3	61.4		144.1	59.6
EVOH44_1%_*N,O*-CMCnp	162.1	54.1		144.3	52.4
EVOH44_3%_*N,O*-CMCnp	161.0	47.9		141.9	47.3
EVOH44_5%_*N,O*-CMCnp	162.3	50.2		144.2	49.9
EVOH44_8%_*N,O*-CMCnp	162.8	51.6		143.4	52.0
EVOH44_1%_qC12np	162.9	61.4		143.5	58.5
EVOH44_3%_qC12np	162.4	60.0		144.2	58.0
EVOH44_5%_qC12np	162.7	59.4		144.0	56.9
EVOH44_8%_qC12np	162.7	58.5		144.0	55.3

6.4 Confocal fluorescence microscopy (CFM)

Figure 6.4-1 shows the CFM results for the EVOH44_CNP electrospun nanofibres, with CNP content from 1-8 wt%. Figure 6.4-1 (a)-(c) indicate a homogenous CNP distribution, including some agglomerates, as the filler content varied between (a) 1 wt%, (b) 3 wt% and (c) 5 wt%. Figure 6.4-1 (d) shows that EVOH44_8%_CNP produced significant CNP agglomerates in the nanofibre mats. The electrospinning method proved ineffective at distributing nanoparticles homogenously through the EVOH matrices at nanoparticle contents of 8 wt% and higher. Therefore, further CFM analyses considered only nanocomposite fibre mats with 3 wt% nanoparticles.

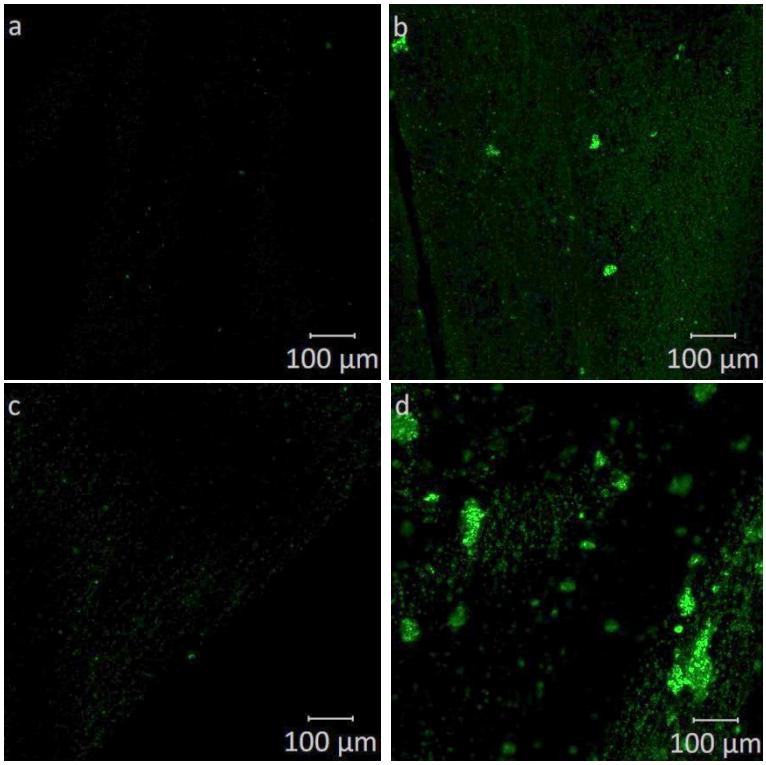

Figure 6.4-1: CFM images of EVOH44 nanocomposite fibres with CNP content of (a) 1 wt%, (b) 3 wt%, (c) 5 wt% and (d) 8 wt%.

The CFM analysis of the EVOH nanocomposite fibres is summarised in Table 6.4-1 and only considered composites with 3 wt% nanoparticle content. The nanoparticle distributions appeared unaffected by the specific type of chitosan nanoparticle, irrespective of the EVOH matrix that was used to create the nanocomposite fibre mats. Furthermore, it appeared as though the nanoparticle agglomerates increased in size as the ethylene mole content increased from 38% to 44% in the EVOH matrices. This trend was not observed for the EVOH27 fibres due to the electrospinning challenges discussed in Chapter 6.2. EVOH27 nanocomposite solutions could not be electrospun at conditions similar to the EVOH38 and EVOH44 fibres. As a result, the nanoparticle distributions of the EVOH27 fibres were not directly comparable to that of the EVOH38 and EVOH44 fibres.

The nanocomposite materials analysed in this study consisted of amphiphilic polymer matrices and filler materials. As a result, the matrix-filler interaction was varied by modifying the hydrophobicity of the chitosan nanoparticles and investigating polymer matrices with increasing hydrophobicity. Based on the CFM results in Table 6.4-1, an optimal matrix-filler configuration was obtained by using EVOH38 as polymer matrix and 3 wt% qC12np as the filler material. Lastly, the results from Table 6.4-1 showed improved nanoparticle distribution by

electrospinning when compared to the nanoparticle distributions of the prepared nanocomposite films in Table 5.4-1 in Chapter 5.

Table 6.4-1: Summary of CFM results for nanocomposite fibres with 3 wt% loadings

	***N,O*-CMCnp**	**CNP**	**qC12np**
EVOH27	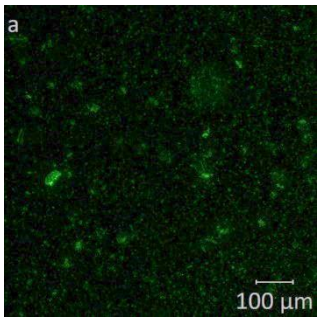	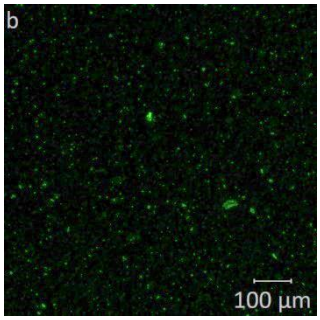	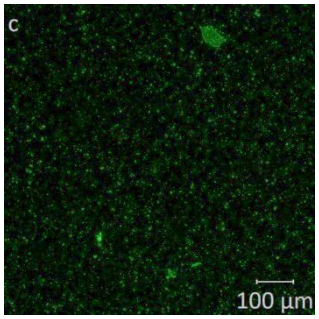
EVOH38	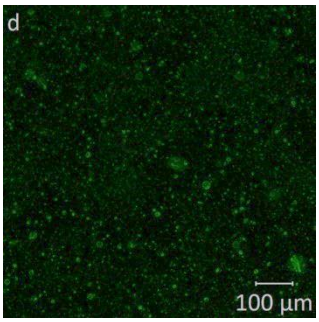	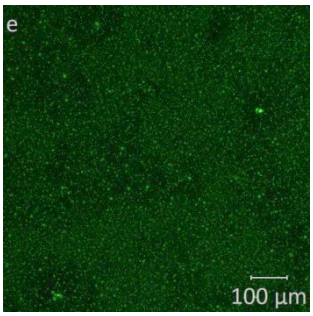	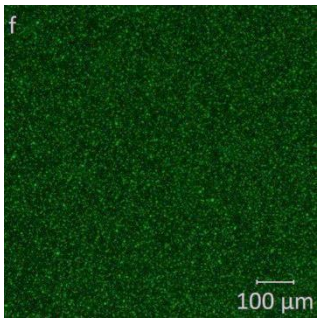
EVOH44	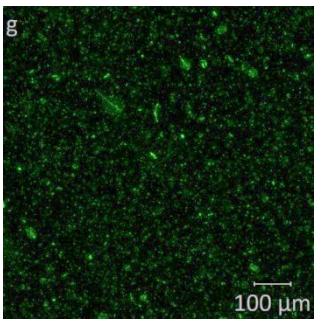	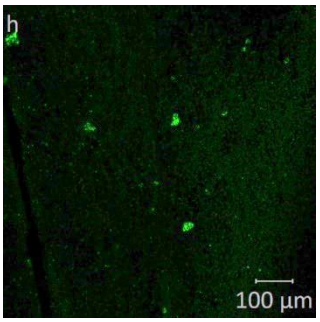	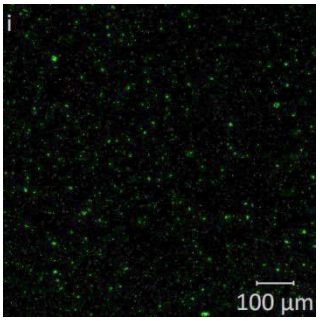

The result from the z-stack analysis, on EVOH38_3%_CNP nanofibres, is shown in Figure 6.4-2. The presence of CNP was not only noticed on the sample surface, but can be seen throughout the depth of the nanofibre mat.

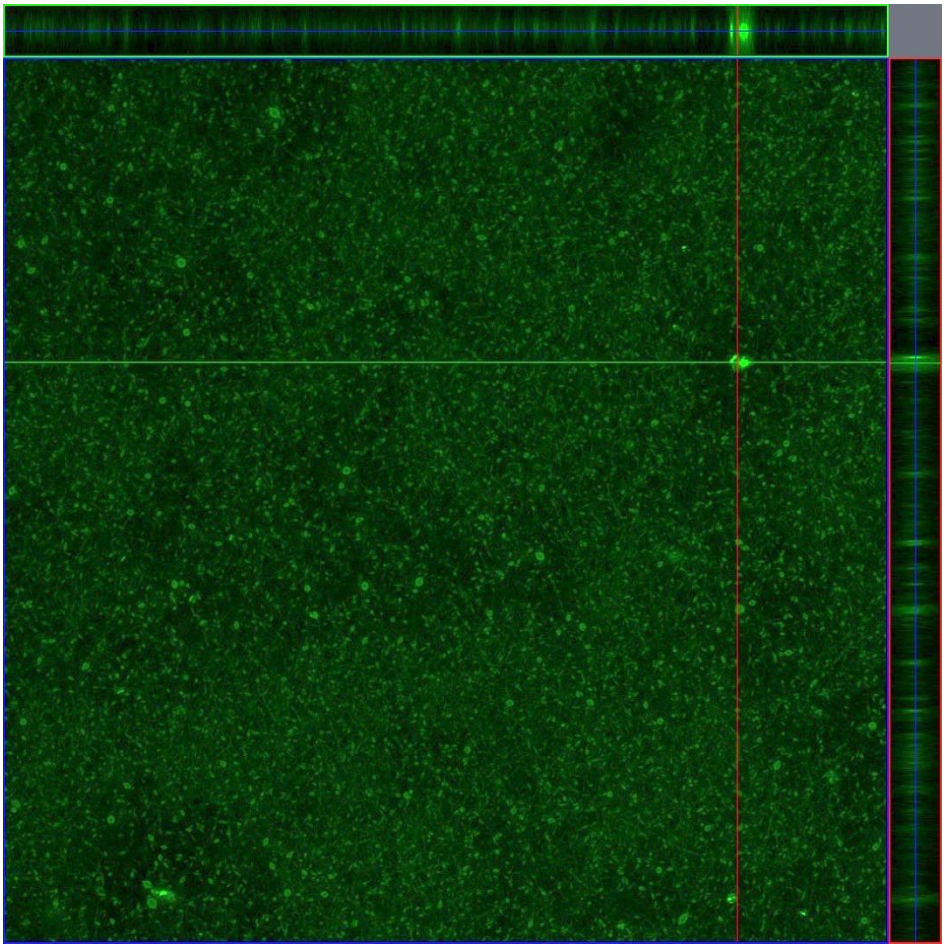

Figure 6.4-2: The z-stack analysis of EVOH38_3%_CNP electrospun nanofibres showing the distribution of CNP throughout the depth of the sample.

6.5 Static contact angle (SCA) and water uptake measurements

6.5.1 Static contact angle (SCA) analysis

The nanocomposite fibres, with EVOH27, EVOH38 and EVOH44 as matrices, were subjected to SCA analysis. No results were obtained for the EVOH27 and EVOH38 matrices as the water droplets were instantly absorbed by the fibre mats. As a result, no clear variations could be observed as the filler content was increased for these two matrices.

The water droplets maintained their shape longer while in contact with the EVOH44 nanocomposite fibres. This is attributed to the increased hydrophobic nature of the EVOH44 matrix, when compared to EVOH27 and EVOH38. Figure 6.5.1-1 shows the SCA results of water making contact with the neat EVOH44 fibre mat.

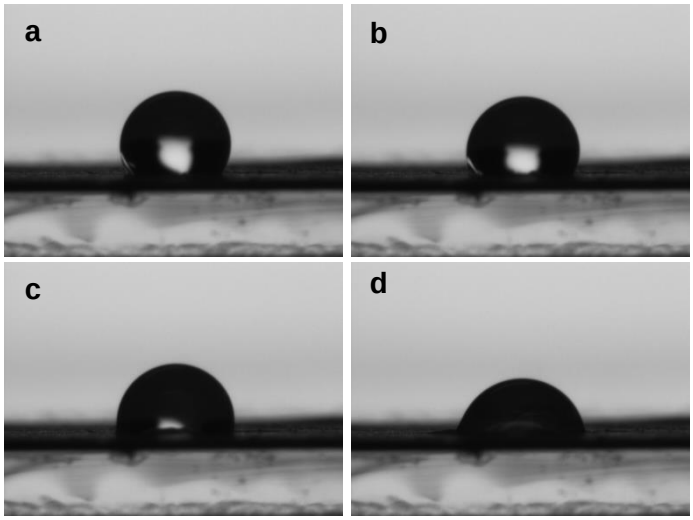

Figure 6.5.1-1: Water droplet making contact with EVOH44_15%_polymer fibre mat for (a) 0 seconds, (b) 6 seconds, (c) 12 seconds, (d) 20 seconds.

Despite the hydrophobic nature of EVOH44, the lower filler loadings had a negligible effect on the contact angle results. Therefore, only the neat EVOH44 fibre mat and the fibre mats with 8 wt% nanoparticle content were analysed. The influence of the nanoparticle content is described by the rate at which the water droplets were absorbed by the fibre mats. This was achieved by measuring the contact angle between the water droplets and the fibre mats over time. The results are shown in Table 6.5.1-1.

Table 6.5.1-1: Water droplet disappearance while in contact with EVOH44 nanocomposite fibre mats

	Rate of disappearance (deg/s)	**Standard deviation (deg/s)**
EVOH44	2.47	0.80
EVOH44_8%_*N,O*-CMCnp	NA	NA
EVOH44_8%_CNP	3.36	0.33
EVOH44_8%_qC12np	1.86	0.28

The EVOH44_8%_CNP fibre mat had a faster rate of disappearance, relative to the neat EVOH44 fibres. This could be due to the nanoparticles having stronger hydrophilic properties than the EVOH44 matrix. The EVOH44_8%_qC12np fibre mat had the slowest rate of disappearance and could be attributed to the addition of the hydrophobic chitosan nanoparticle to the fibre mats. Finally, the EVOH44_8%_*N,O*-CMCnp fibre mat was expected to be the most hydrophilic sample and possess the fastest rate of water absorbance. This was confirmed by the fact that the water droplets were immediately absorbed by the fibre mats. Therefore, no contact angle data could be obtained over a known period of time.

The results shown in Table 6.5.1-1 could also be influenced by fibre diameters. The results of the fibre diameters are shown in Table 6.2-3 but there is no clear correlation between the obtained fibre diameters and the observed rates of water absorption.

6.5.2 Water uptake

Swelling studies of composite fibre mats with nanoparticle contents of 3 wt% and 8 wt% were done, along with neat EVOH38 and EVOH44 fibres. Figure 6.5.2-1 illustrates the swelling behaviour of EVOH38 fibres with 3 wt% nanoparticle content. The neat fibre mat showed the highest water uptake after 24 hours. The water uptake for EVOH38_3%_qC12np remained the lowest during the 24 hours. This trend was investigated further by testing the 8 wt% fibre mats.

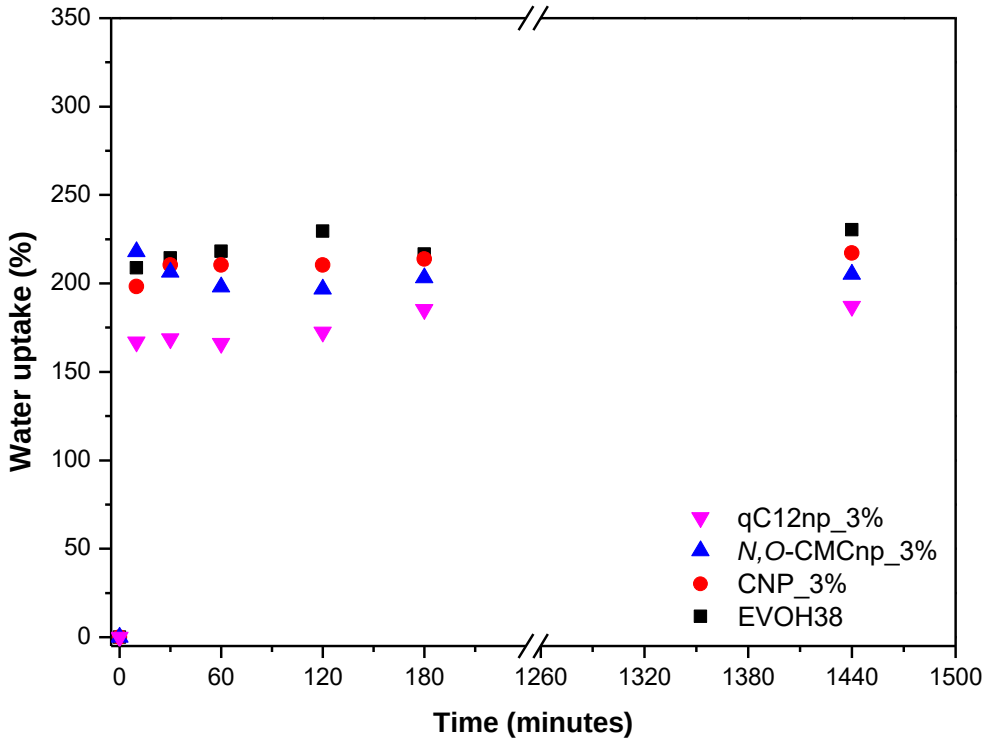

Figure 6.5.2-1: Water uptake of EVOH38 nanocomposite fibre mats with 3 wt% nanoparticle content.

Figure 6.5.2-2 shows the water uptake results for the EVOH38 nanocomposite fibres with 8 wt% nanoparticle content. The hydrophobic chitosan nanocomposite achieved the lowest water uptake, similar to what is shown in Figure 6.5.2-1. Furthermore, the hydrophilic chitosan nanocomposite, EVOH38_8%_*N,O*-CMCnp, achieved the highest water uptake during the 24 hours. The expected influence of the different types of nanoparticles became apparent at filler loadings of 8 wt%. EVOH38 appeared to be a suitable polymer matrix for this study as the water uptake of the EVOH38 nanocomposite fibres was successfully modified with the incorporation of functionalised chitosan nanoparticles.

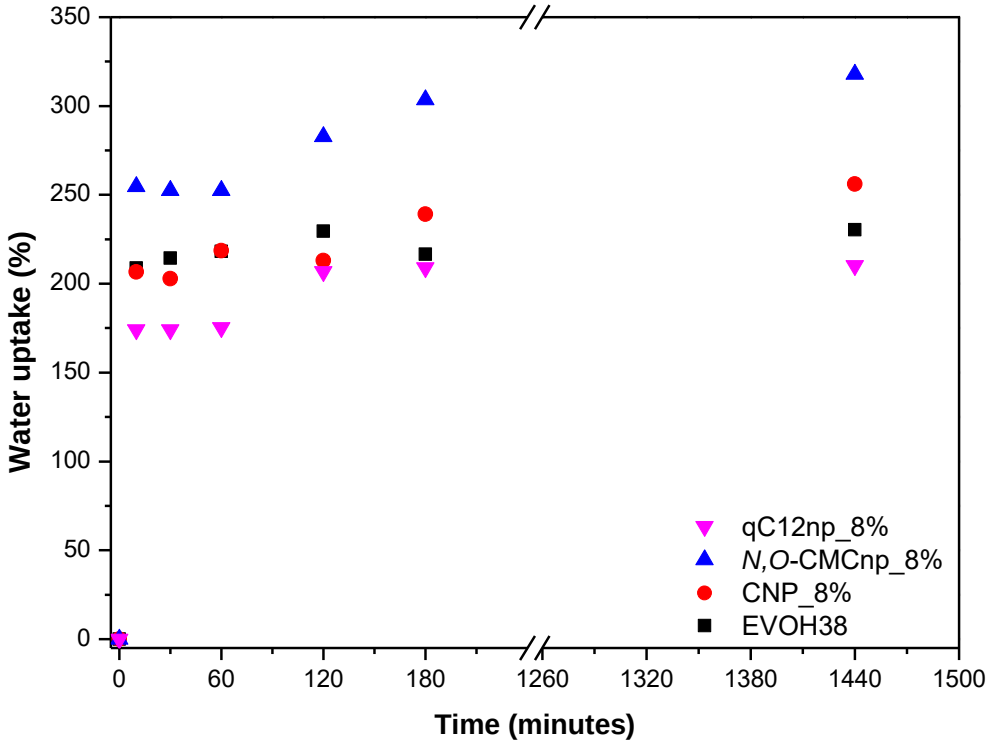

Figure 6.5.2-2: Water uptake of EVOH38 nanocomposite fibre mats with 8 wt% nanoparticle content.

The EVOH44 nanocomposite fibres were subjected to similar water uptake tests. Figure 6.5.2-3 shows that the EVOH44 control fibres achieved the highest water uptake, when compared to 3 wt% filler content sample. This result was also obtained in the case of the EVOH38 matrix. Therefore, the chitosan functionalisation did not appear to show the expected trends at 3 wt% filler content.

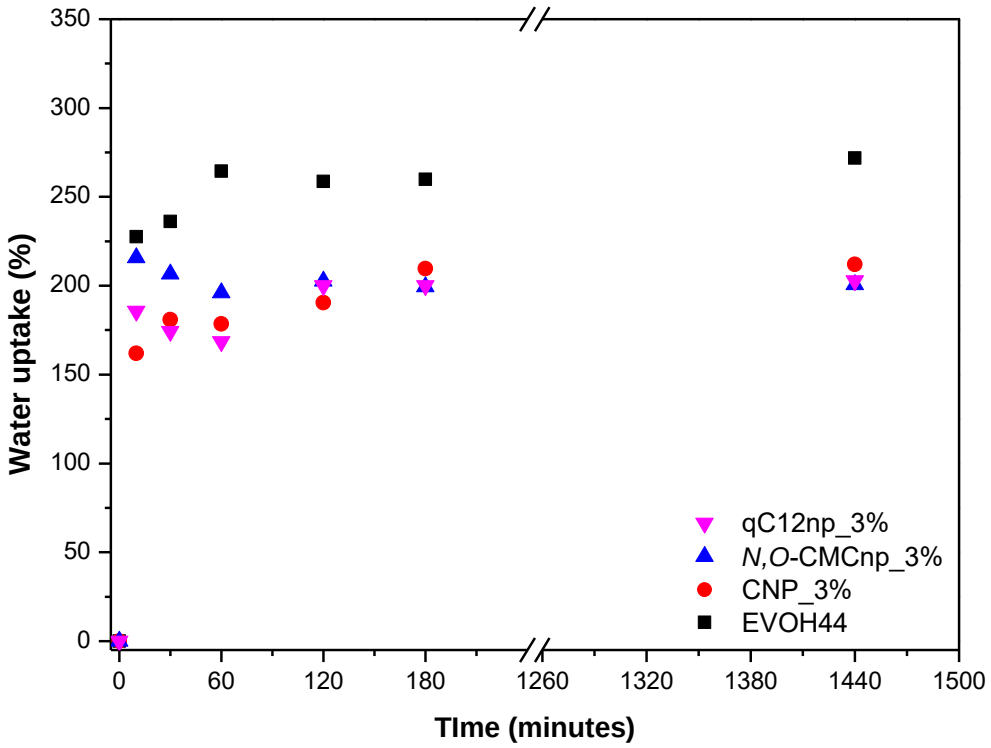

Figure 6.5.2-3: Water uptake of EVOH44 nanocomposite fibre mats with 3 wt% nanoparticle content.

Figure 6.5.2-4 shows the water uptake for EVOH44 nanocomposite fibres with 8 wt% nanoparticles. The EVOH44_8%_qC12np nanocomposite showed a significant decrease in water uptake, compared to the neat EVOH44 and EVOH44_3%_qC12np. The EVOH44_8%_CNP and EVOH44_8%_*N,O*-CMCnp nanocomposite fibres showed increased water uptake, relative to the 3 wt% samples, but not relative to the neat EVOH44 nanofibres. This may possibly be attributed to increased nanoparticle agglomeration throughout the nanofibre mats. Table 6.4-1 indicates that qC12np had the best distribution throughout the EVOH44 matrix. The conclusion was that the ethylene content of the EVOH44 matrix led to the increased agglomeration of the polar CNP and *N,O*-CMCnp, while hydrophobic interactions between the EVOH44 matrix and qC12np improved nanoparticle distributions.

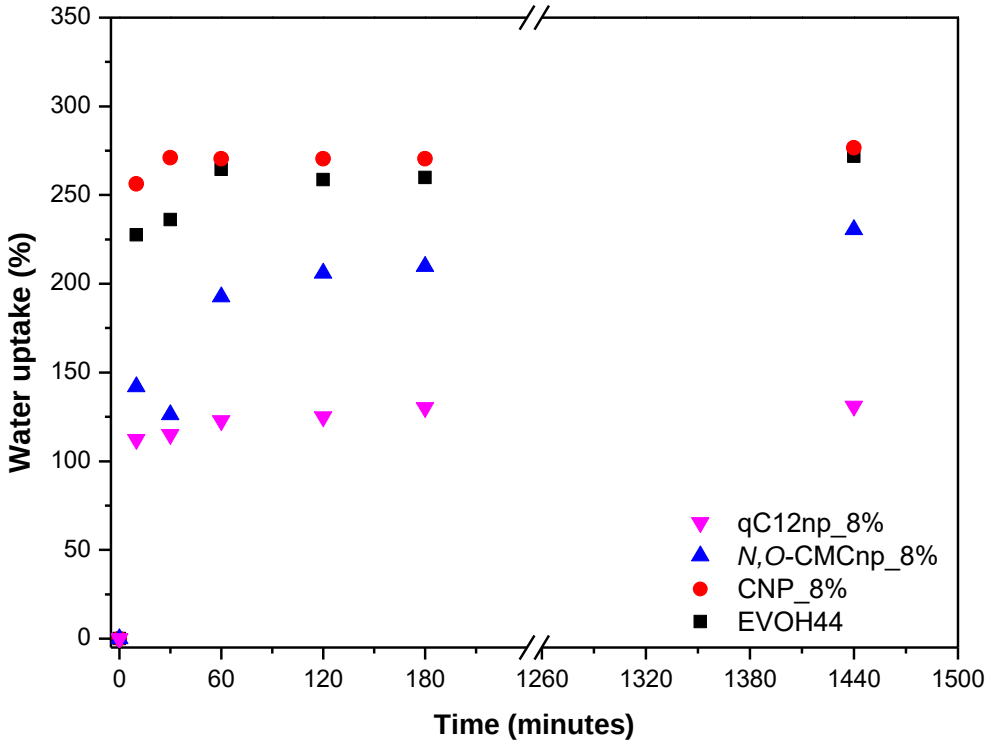

Figure 6.5.2-4: Water uptake of EVOH44 nanocomposite fibre mats with 8 wt% nanoparticle content.

6.6 Antimicrobial testing

The produced nanocomposite fibres were subjected to antimicrobial tests, as discussed in Chapter 3. The sample layout was also discussed in Chapter 3.3.11. The results of the immediate and direct inhibition of *S. aureus* are shown in Figure 6.6-1 and Figure 6.6-2.

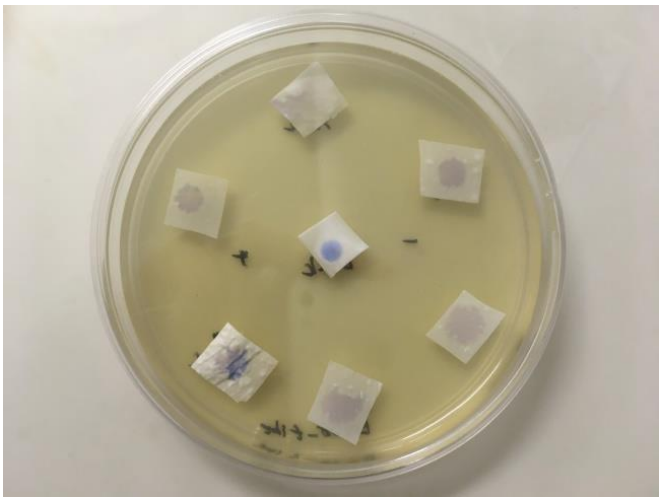

Figure 6.6-1: Antimicrobial results for EVOH38 nanocomposite fibres exposed to *Staphylococcus aureus* (*S. aureus*) to investigate direct inhibition.

According to Figure 6.6-1 the EVOH38 and EVOH38_8%_qC12np samples showed immediate inhibition of *S. aureus*. Figure 6.6-2 also shows immediate inhibition for EVOH44_3%_qC12np. Quaternised chitosan derivatives have previously been reported to provide enhanced antimicrobial activity, relative to unmodified chitosan, but the performance of the control EVOH38 nanofibre did not indicate any clear correlation[6–10]. Therefore, no trend was noticed based on nanoparticle filler type or quantity. The diameters of the eletrospun nanofibres, shown in Table 6.2-3, were considered for their influence on the attachment of *S. aureus* onto the samples. No clear correlation was observed between fibre diameter and direct inhibition. The samples in Figure 6.6-1 and Figure 6.6-2, which display immediate inhibition, appear to show decreased wettability, relative to the other samples. This was confirmed by visual inspection of the absorption of the alamarBlue dye into the nanocomposite fibres. The fibre density of the samples could have possibly had an impact on the attachment of the *S. aureus* during the direct contact phase.

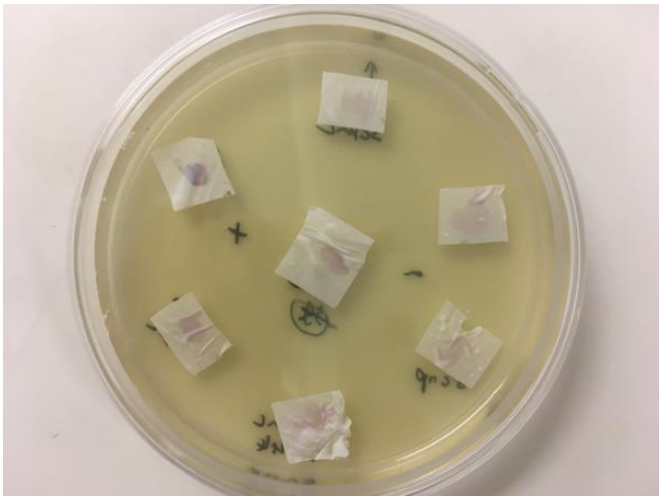

Figure 6.6-2: Antimicrobial results for EVOH44 nanocomposite fibres exposed to *Staphylococcus aureus* (*S. aureus*) to investigate direct inhibition.

The incubation of the samples negated the influence of the fibre densities and provided sufficient time for the *S. aureus* and growth media to distribute throughout the nanocomposite fibres. These results are shown in Figure 6.6-3 and Figure 6.6-4 and were analysed for the formation of zones of inhibition around the nanoparticle loaded samples[11].

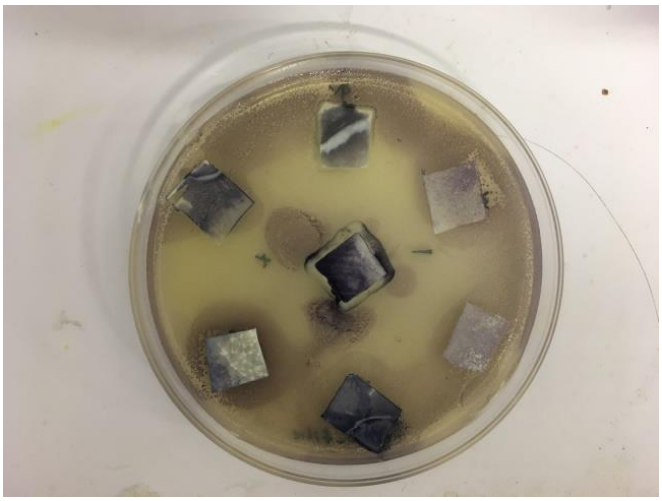

Figure 6.6-3: Antimicrobial results for EVOH38 nanocomposite fibres exposed to *Staphylococcus aureus* (*S. aureus*) after incubation to investigate halo formation.

Despite the initial inhibition, which was noticed earlier, the dye staining process showed no halo formation in both Figure 6.6-3 and Figure 6.6-4. Furthermore, it showed microbial activity within the fibres, even though it was shown in Chapter 6.4 that the nanoparticle fillers were distributed homogenously throughout the nanofibres. The conclusion was that the addition of any of the nanoparticles up to 8 wt% did not influence the antimicrobial properties of the electrospun materials and that there was insufficient interaction between the produced nanoparticles and *S. aureus*.

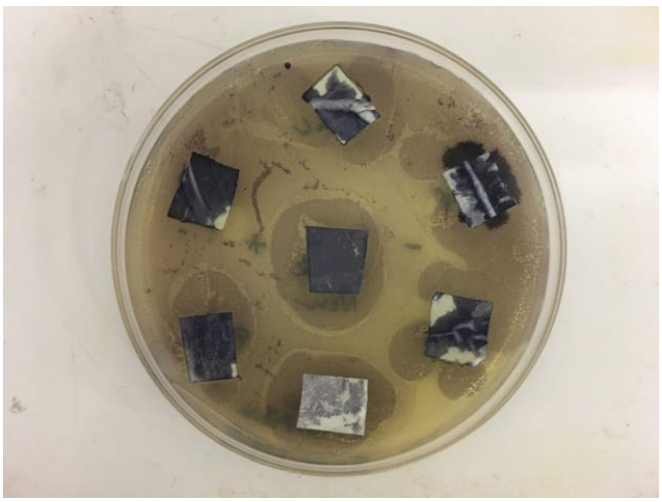

Figure 6.6-4: Antimicrobial results for EVOH44 nanocomposite fibres exposed to *Staphylococcus aureus* (*S. aureus*) after incubation to investigate halo formation.

6.7 Conclusions

The results from SEM analysis showed that an optimal polymer concentration of 15 wt% in the electrospinning solution for EVOH38 and EVOH44 was found, where the majority of desired composites could be electrospun. The EVOH27 proved difficult to electrospin even at 20 wt% polymer. No clear correlation was observed between fibre diameters and nanoparticle loading. It was, however, noted that the fibre diameters of EVOH44 generally appeared to be smaller than those for the EVOH38 nanofibres. This was attributed to the increased ethylene content which aided the fibre drawing process during electrospinning. The nanoparticle distribution within the nanocomposite fibres were investigated by CFM and showed that nanoparticle agglomeration occurred during the electrospinning process at filler content higher than 8 wt%. The EVOH matrices appeared to play a significant role in determining the ease of electrospinning and nanoparticle dispersion. An optimal nanocomposite fibre was identified, in terms of nanoparticle distribution. The use of EVOH38 as electrospinning matrix and qC12np as filler material yielded the best nanoparticle distributions and modification of the nanocomposite fibre properties.

Thermal analysis of the nanocomposite fibres, by DSC, showed no significant changes in the melting and crystallisation temperatures after the addition of the different nanoparticles. The melting and crystallisation enthalpies decreased with the addition of 3 wt% nanofillers and more. Physical and surface properties were evaluated by SCA and water uptake studies. The SCA results for the EVOH44 nanocomposite fibres showed that the wettability increased with the addition of the hydrophilic *N,O*-CMCnp and decreased with the addition of the hydrophobic qC12np. These trends were confirmed by water uptake studies which showed similar trends in the maximum water uptake of the nanocomposite fibres. The antimicrobial studies showed no clear antimicrobial activity of the nanocomposite fibres. A high fibre density prevented *S. aureus* from attaching to the samples but when given sufficient time to absorb into the fibre samples no growth inhibition was noticed. This could have been caused by a lack of contact between the incorporated nanoparticles and *S. aureus*. Changing the physical structure of the EVOH matrices into an electrospun fibre mat therefore did not enhance the antimicrobial properties, despite the enhanced surface area.

6.8 References

1. Du Toit, M. L. Incorporation of polysaccharide nanowhiskers into a poly (ethylene-co-vinyl alcohol) matrix (MSc). (University Stellenbosch, 2013).
2. Keulder, L. The preparation of polyolefin nanofibres by solution electrospinning (PhD). (University Stellenbosch, 2013).
3. Prasanna, K. & Sailaja, R. R. N. Blends of LDPE/chitosan using epoxy-functionalized LDPE as compatibilizer. *J. Appl. Polym. Sci.* **124**, 3264–3275 (2012).
4. Rogovina, S. Z., Aleksanyan, K. V., Novikov, D. D., Prut, E. V. & Rebrov, A. V. Synthesis and investigation of polyethylene blends with natural polysaccharides and their derivatives. *Polym. Sci. - Ser. A* **51**, 554–562 (2009).
5. Rogovina, S. Z., Alexanyan, C. V. & Prut, E. V. Biodegradable blends based on chitin and chitosan: Production, structure, and properties. *J. Appl. Polym. Sci.* **121**, 1850–1859 (2011).
6. Sahariah, P., Benediktssdóttir, B. E., Hjálmarsdóttir, M. A., Sigurjonsson, O. E., Sørensen, K. K., Thygesen, M. B., Jensen, K. J. & Másson, M. Impact of chain length on antibacterial activity and hemocompatibility of quaternary N-alkyl and N, N-dialkyl chitosan derivatives. *Biomacromolecules* **16**, 1449–1460 (2015).
7. Jung, E. J., Youn, D. K., Lee, S. H., No, H. K., Ha, J. G. & Prinyawiwatkul, W. Antibacterial activity of chitosans with different degrees of deacetylation and viscosities. *Int. J. Food Sci. Technol.* **45**, 676–682 (2010).
8. Sahariah, P. & Másson, M. Antimicrobial Chitosan and Chitosan Derivatives: A Review of the Structure-Activity Relationship. *Biomacromolecules* **18**, 3846–3868 (2017).
9. Tan, H., Ma, R., Lin, C., Liu, Z. & Tang, T. Quaternized chitosan as an antimicrobial agent: Antimicrobial activity, mechanism of action and biomedical applications in orthopedics. *Int. J. Mol. Sci.* **14**, 1854–1869 (2013).
10. Guo, Z., Xing, R., Liu, S., Zhong, Z., Ji, X., Wang, L. & Li, P. Antifungal properties of Schiff bases of chitosan, N-substituted chitosan and quaternized chitosan. *Carbohydr. Res.* **342**, 1329–1332 (2007).
11. Kaya, M., Cakmak, Y. S., Baran, T., Asan-Ozusaglam, M., Mentes, A. & Tozak, K. O. New chitin, chitosan, and O-carboxymethyl chitosan sources from resting eggs of Daphnia longispina (Crustacea); with physicochemical characterization, and antimicrobial and antioxidant activities. *Biotechnol. Bioprocess Eng.* **19**, 58–69 (2014).

CHAPTER 7

CONCLUSIONS AND RECOMMENDATIONS

7.1 Conclusions

Hydrophilic *N,O*-CMC and hydrophobic qC12 was successfully synthesised and this was confirmed by NMR and FTIR analysis. Characteristic peaks were observed which indicated that *N*-carboxymethylation and *O*-carboxymethylation were formed during *N,O*-CMC synthesis. Furthermore, the attachment of an alkyl chain was observed in the NMR results of qC12.

The nanoparticle production of all three chitosan variants was considered a success with average nanoparticle diameters ranging between 86-126 nm. The average particle diameters were confirmed by SEM analysis, measuring a minimum of 200 nanoparticles per nanoparticle type.

Nanocomposite films, with EVOH and LDPE matrices, were prepared with up to 8 wt% nanoparticle content. Individual nanoparticles were observed on the film surfaces using SEM. Optical images and UV/Vis showed a decrease in film transparency as the nanoparticle content increased up to 8 wt%. According to CFM the nanoparticle distribution improved as the hydrophobicity of the matrix decreased. This was shown using EVOH matrices with varying ethylene content. No clear correlation could be observed between nanoparticle functionalisation and distribution as the matrix properties appeared to be the dominant factor. The water uptake and SCA measurements showed, in general, that the addition of the three kinds of chitosan nanoparticles into LDPE and EVOH matrices increased wettability, irrespective of nanoparticle functionalisation. Exposure of *S. aureus* to the nanocomposite films showed growth inhibition. The inhibition was attributed to the hydrophobicity of the films which prevented *S. aureus* from attaching to the surfaces. Therefore, the influence of the added nanoparticles could not be observed.

Nanocomposite fibres were successfully electrospun, using three different grades of EVOH with varying ethylene content. It was noted that the electrospinning procedure became ineffective for EVOH27, with an ethylene content of 27 mole %, as the nanoparticle content reached 8 wt%. The nanoparticle presence in the electrospinning solution therefore hindered the fibre drawing process. The SEM results indicated that the fibre diameters decreased with an increase in the ethylene content of the EVOH matrices. The effect of the added nanoparticles on the fibre diameters remained inconclusive. The results from CFM showed that EVOH38 and a 3 wt% nanoparticle loading was the optimal matrix and loading combination respectively for homogenous distribution of the filler material during electrospinning. The SCA measurements of EVOH44 nanocomposite fibres showed that the wettability increased with the addition of the

hydrophilic *N,O*-CMCnp and decreased with the addition of the hydrophobic qC12np. The results could have been influenced by fibre diameters and density but no clear correlation between these properties and wettability was observed. The SCA analysis was supplemented with water uptake experiments and the observed wettability trends were confirmed with the water uptake results. The antimicrobial studies of the nanocomposite fibres showed no inhibition of *S. aureus* and it was concluded that an 8 wt% nanoparticle content was insufficient to provide antimicrobial properties to the nanocomposite materials.

When comparing the results of the nanocomposite films with those of the fibres it was concluded that the nanoparticles were homogenously distributed with the most success in the nanocomposite fibres. Furthermore, it was noted that the water uptake capabilities of the fibres were more dependent on the addition of the various kinds of chitosan nanoparticles, albeit from direct modification of the fibre hydrophobicity or indirectly influencing the fibre diameters during electrospinning. The antimicrobial studies showed that 8 wt% of the added nanoparticles had an insignificant influence on the growth of *S. aureus*. This may be attributed to a lack of contact between *S. aureus* and the produced nanoparticles.

7.2 Recommendations

For future work it would be advantageous to improve the *N,O*-CMC and qC12 functionalisation processes to have more control over the degree of functionalisation. In addition, the crosslinking procedure can be modified in order to obtain nanoparticles of equal size so that particle size can be eliminated as a potential variable.

The influence of the chitosan functionalisation might be more significant in the composite films if the chitosan is applied directly onto the polymer film surfaces. An investigation into film coating methods can potentially lead to promising results.

Electrospinning of EVOH with chitosan nanoparticles above 8 wt% can be investigated. Furthermore, surface modification of EVOH, with chitosan, after electrospinning might prove to have a more significant impact on the fibre properties.

APPENDIX A

SUPPLEMENTARY RESULTS

Nanocomposite Films

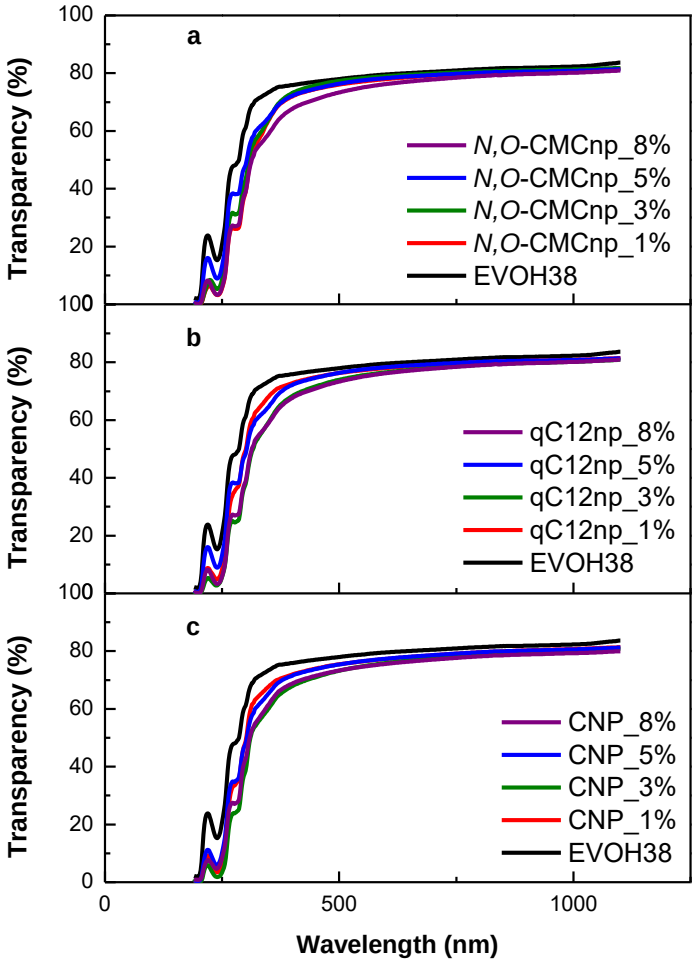

Figure A-1: UV/Vis results of nanocomposite films using EVOH38 as matrix and (a) *N,O*-CMCnp, (b) qC12np and (c) CNP as nanofiller.

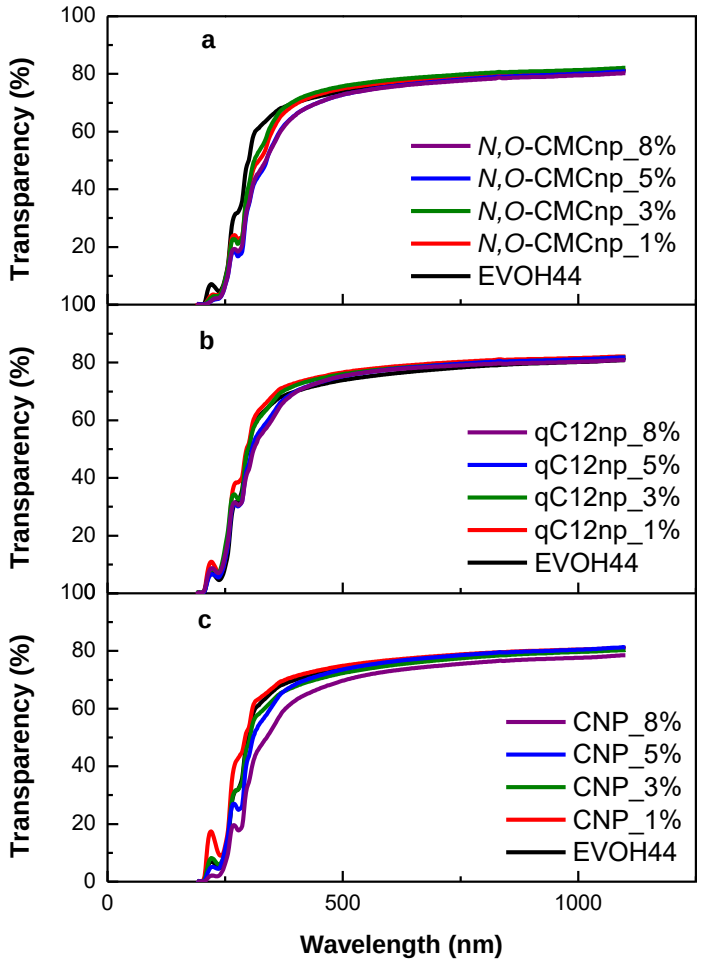

Figure A-2: UV/Vis results of nanocomposite films using EVOH44 as matrix and (a) *N,O*-CMCnp, (b) qC12np and (c) CNP as nanofiller.

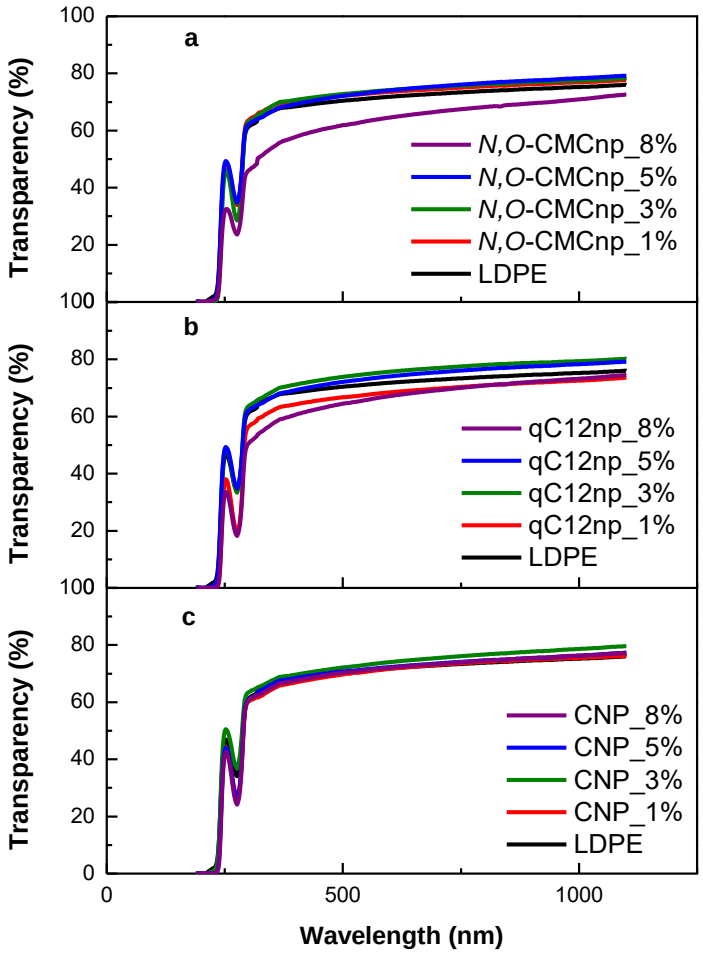

Figure A-3: UV/Vis results of nanocomposite films using LDPE as matrix and (a) *N,O*-CMCnp, (b) qC12np and (c) CNP as nanofiller.

Table A-1: Summary of DSC results for EVOH27 nanocomposite films during the second heating cycle and the cooling event

	Melting			Crystallisation	
Sample	**T_m (°C)**	**H_m (J/g)**		**T_c (°C)**	**H_c (J/g)**
EVOH27	187.8	61.7		166.2	55.6
EVOH27_1%_CNP	187.7	56.2		166.8	50.1
EVOH27_3%_CNP	188.2	61.8		167.3	56.4
EVOH27_5%_CNP	188.2	64.6		166.0	57.8
EVOH27_8%_CNP	186.7	52.7		166.1	50.2
EVOH27_1%_ *N,O*-CMCnp	183.8	62.5		163.0	53.2
EVOH27_3%_ *N,O*-CMCnp	184.8	61.5		164.3	52.4
EVOH27_5%_ *N,O*-CMCnp	187.2	59.8		166.6	52.8
EVOH27_8%_ *N,O*-CMCnp	186.8	62.0		166.5	54.0
EVOH27_1%_qC12np	187.7	67.7		166.4	59.9
EVOH27_3%_qC12np	187.2	68.9		166.0	62.6
EVOH27_5%_qC12np	187.2	75.2		165.8	61.6
EVOH27_8%_qC12np	186.6	60.4		165.3	53.5

Table A-2: Summary of DSC results for EVOH38 nanocomposite films during the second heating cycle and the cooling event

	Melting			Crystallisation	
Sample	**T_m (°C)**	**H_m (J/g)**		**T_c (°C)**	**H_c (J/g)**
EVOH38	176.4	62.6		155.3	58.8
EVOH38_1%_CNP	176.2	65.2		156.6	63.5
EVOH38_3%_CNP	176.3	65.8		156.5	63.5
EVOH38_5%_CNP	176.0	64.4		156.1	63.6
EVOH38_8%_CNP	175.4	62.2		155.2	57.2
EVOH38_1%_ *N,O*-CMCnp	175.5	64.7		155.6	62.0
EVOH38_3%_ *N,O*-CMCnp	175.2	59.1		155.7	57.2
EVOH38_5%_ *N,O*-CMCnp	175.7	62.3		156.5	59.8
EVOH38_8%_ *N,O*-CMCnp	175.1	55.7		155.4	56.0
EVOH38_1%_qC12np	176.4	64.0		155.2	63.1
EVOH38_3%_qC12np	176.2	64.2		155.8	63.2
EVOH38_5%_qC12np	175.9	63.4		156.0	61.6
EVOH38_8%_qC12np	175.5	61.3		155.1	60.0

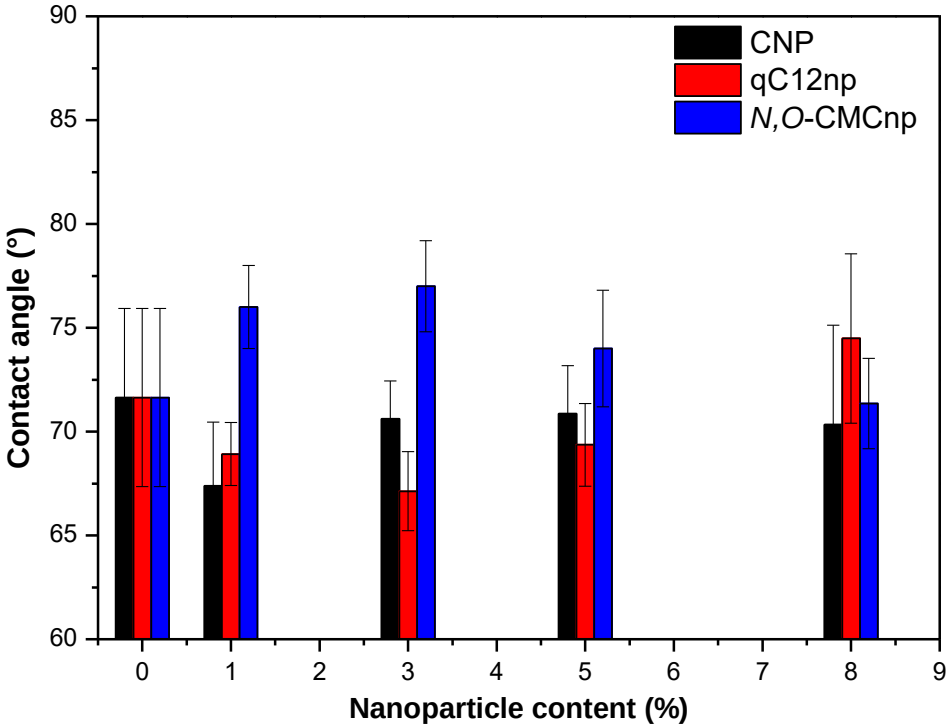

Figure A-4: Static contact angle results for EVOH27 nanocomposite films with varying filler content.

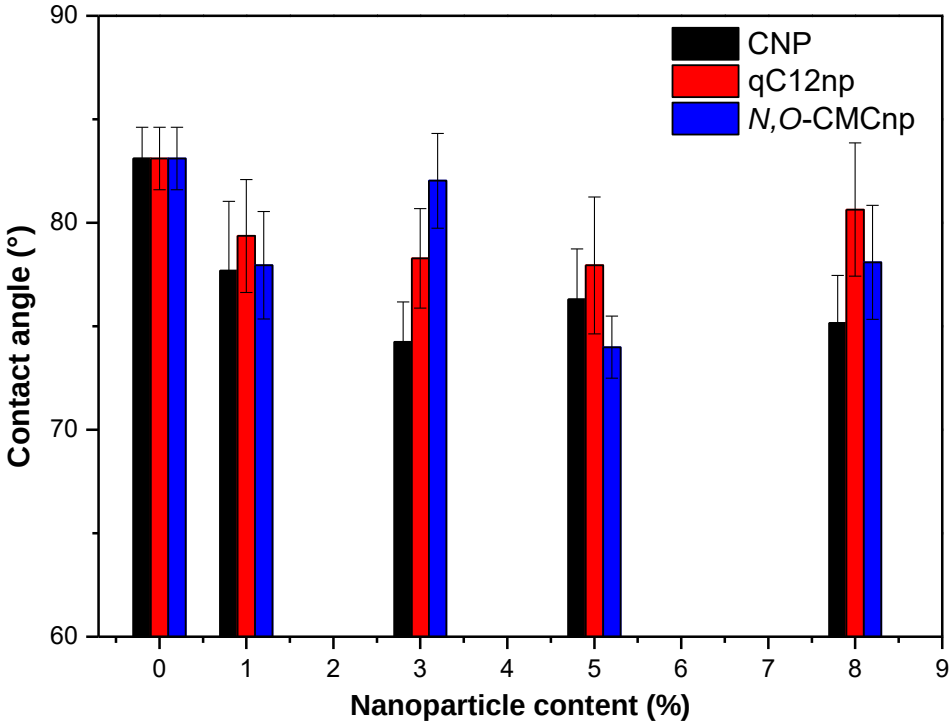

Figure A-5: Static contact angle results for EVOH38 nanocomposite films with varying filler content.

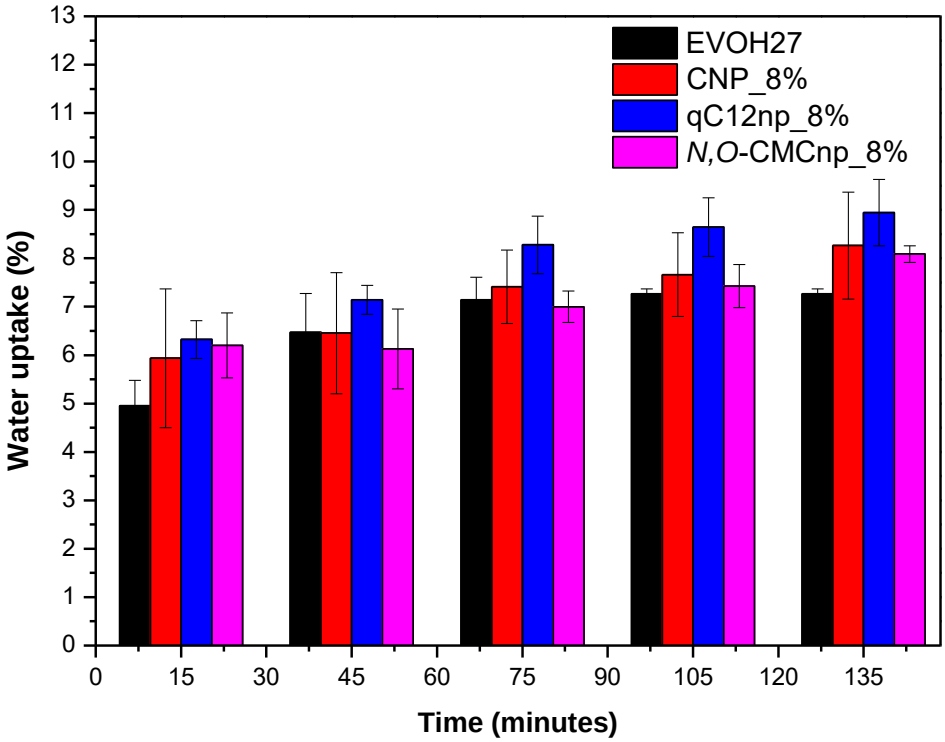

Figure A-6: Water uptake results for EVOH27 nanocomposite films with 8 wt% nanoparticle content.

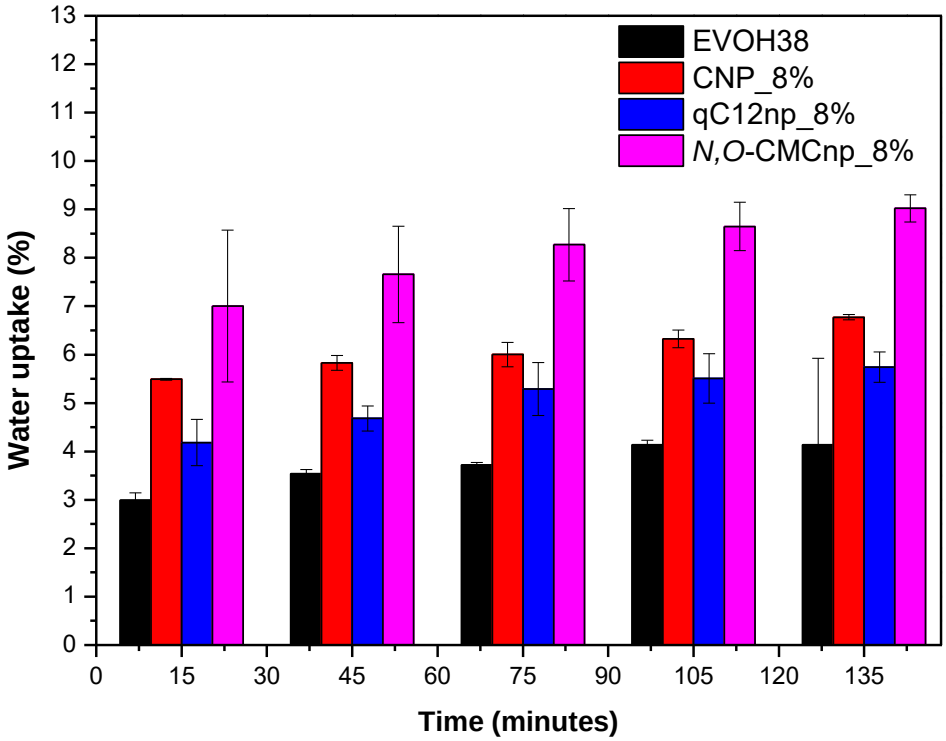

Figure A-7: Water uptake results for EVOH38 nanocomposite films with 8 wt% nanoparticle content.

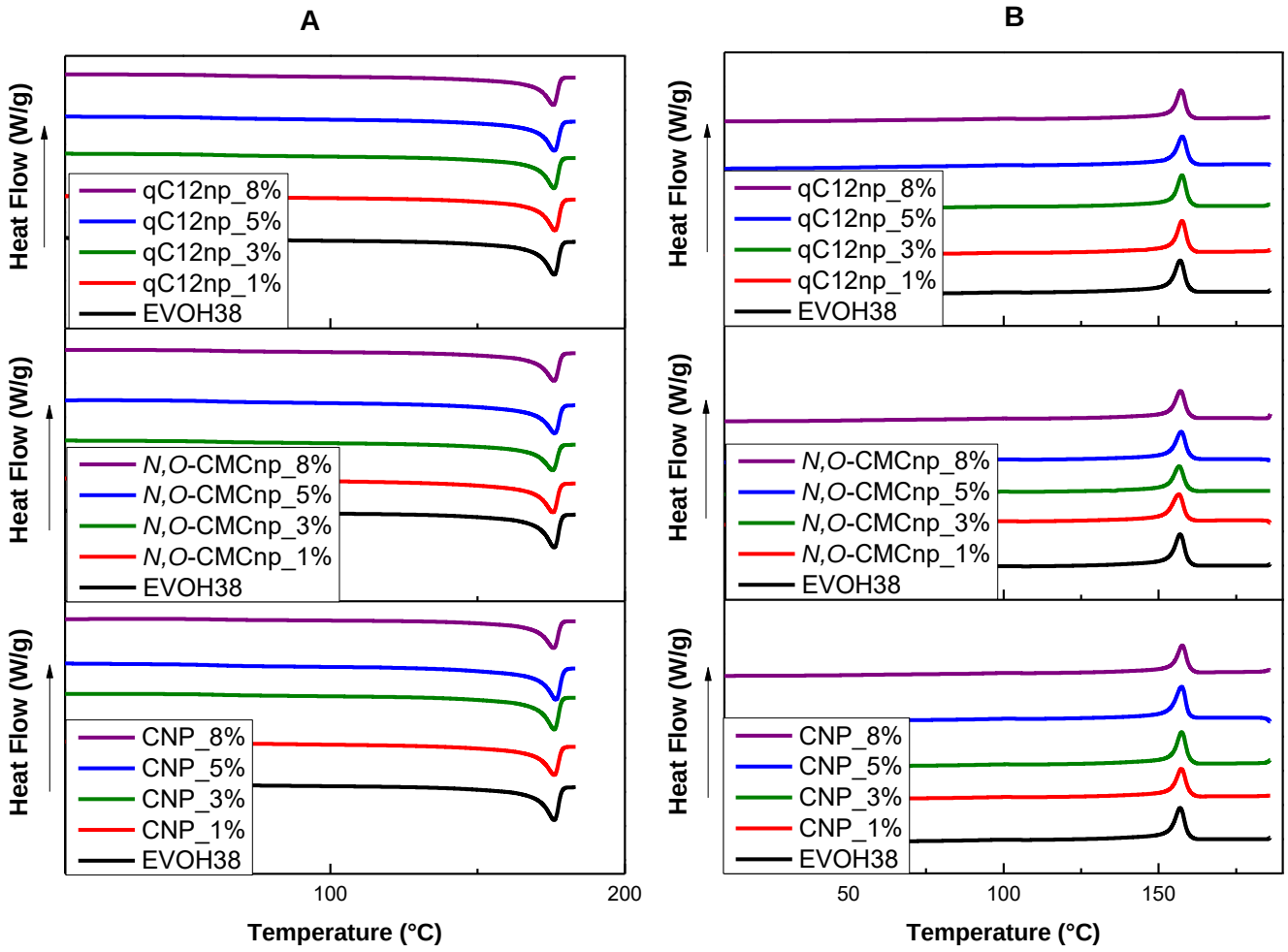

Figure A-8: DSC curves of EVOH38 nanocomposite fibres during (A) the second heating cycle and (B) cooling cycle.

Table A-3: Summary of DSC results for EVOH38 nanocomposite fibres during the second heating cycle and the cooling event

	Melting			Crystallisation	
Sample	**T_m (°C)**	**H_m (J/g)**		**T_c (°C)**	**H_c (J/g)**
EVOH38	176.0	65.2		157.0	64.8
EVOH38_1%_CNP	176.0	57.4		157.3	55.9
EVOH38_3%_CNP	176.0	63.1		157.4	61.6
EVOH38_5%_CNP	176.5	65.9		157.4	62.4
EVOH38_8%_CNP	175.8	54.0		157.6	52.2
EVOH38_1%_*N,O*-CMCnp	175.5	59.9		156.5	57.2
EVOH38_3%_*N,O*-CMCnp	175.5	53.6		156.6	51.0
EVOH38_5%_*N,O*-CMCnp	176.2	59.3		157.3	58.4
EVOH38_8%_*N,O*-CMCnp	175.9	56.6		157.0	56.5
EVOH38_1%_qC12np	176.3	61.7		157.5	59.1
EVOH38_3%_qC12np	175.9	59.0		157.5	59.2
EVOH38_5%_qC12np	176.0	59.0		157.6	56.9
EVOH38_8%_qC12np	175.7	55.5		157.3	52.2